JOURNAL OF PETROLOGY | VOLUME 48 | NUMBER 6 | PAGES 1079–1118 | 2007 | doi:10.1093/petrology/egm011

Entrained Macrocryst Minerals as a Key to the Source Region of Olivine Nephelinites: Humberg, Kaiserstuhl, Germany

ALEXEY ULIANOV[1]*, OTHMAR MÜNTENER[1], PETER ULMER[2] AND THOMAS PETTKE[3]

[1]UNIVERSITY OF LAUSANNE, INSTITUTE OF MINERALOGY AND GEOCHEMISTRY, ANTHROPOLE, CH-1015 LAUSANNE, SWITZERLAND

[2]INSTITUTE OF MINERALOGY AND PETROGRAPHY, ETH ZÜRICH, ETH ZENTRUM, SONNEGGSTRASSE 5, CH-8092 ZÜRICH, SWITZERLAND

[3]INSTITUTE OF GEOLOGICAL SCIENCES, UNIVERSITY OF BERN, BALTZERSTRASSE 1–3, CH-3012 BERN, SWITZERLAND

RECEIVED MAY 18, 2006; ACCEPTED FEBRUARY 27, 2007
ADVANCE ACCESS PUBLICATION APRIL 17, 2007

Olivine nephelinites commonly contain macrocrysts of olivine and clinopyroxene. Some of these macrocrysts might represent fragments of the source region of the host magma transported to the Earth's surface. If this hypothesis is correct these fragments can be used to characterize the composition of the source region and to put constraints on the magma generation process. In this study, we investigate the origin of macrocrysts and mineral aggregates from an olivine nephelinite from the Kaiserstuhl, Germany. We focus on clinopyroxenes (Cpx), which can be divided into three groups. Cpx I is relict Cpx from aggregates with deformed olivine that is depleted in Ca and characterized by strong light rare earth element (LREE) fractionation, low Ti/Eu and negative high field strength element (HFSE) anomalies. Its geochemical signature is consistent with formation by carbonatite metasomatism and with equilibration in the presence of orthopyroxene. Cpx II is Ca-rich Cpx, forming both aggregates with deformed olivine and individual macrocrysts. The LREE, as for Cpx I, are strongly fractionated. Convex REE patterns may be present. The depletion in HFSE is less pronounced. Cpx III is oscillatory zoned Cpx phenocrysts showing enrichment in Ca, convex REE patterns and no HFSE anomalies. The transition in the trace element abundances between the Cpx of the three groups is gradual. However, Cpx I and II did not crystallize from the host magma, as demonstrated by the presence of kink-bands and undulose extinction in the associated olivine and by the composition of alkali aluminosilicate glass inclusions in Cpx II. Based on the Cpx relationships, we interpret the studied suite of macrocrysts and mineral aggregates as a mixture of disintegrated fragments of the source region of the host olivine nephelinite. The process of melt generation was multi-stage. A primary carbonatite melt ascending from deeper levels in the mantle, probably from the dolomite–garnet peridotite stability field, reacted with mantle peridotite along the solidus ledge in the system lherzolite–CO_2 (<20–22 kbar) and started to crystallize carbonate minerals. Because of its low solidus temperature, the resulting carbonate-wehrlite assemblage melted incongruently with the formation of additional clinopyroxene. The carbonatite melt evolved during crystallization of carbonate minerals and concomitant incongruent melting of the carbonate-wehrlite, accompanied by the segregation of incipient alkali aluminosilicate melts. As a consequence of fast reaction rates in the presence of a carbonatite melt, this process probably took place under disequilibrium conditions. Further melting of the assemblage wehrlite + alkali aluminosilicate melt led to the generation of the olivine nephelinite magma. It entrained fragments of the wehrlite and brought them to the surface.

KEY WORDS: *carbonatite; metasomatism; source region; clinopyroxene macrocrysts; wehrlite; olivine nephelinite; Kaiserstuhl*

INTRODUCTION

The understanding of magma generation processes requires characterization of the source region that undergoes partial melting. Constraints on the phase assemblage

*Corresponding author. Telephone: +0041 21 6924452. Fax: +0041 21 6924305. E-mail: Alexey.Ulianov@unil.ch

of the source region, the major and trace element compositions of its mineral and volatile components and conditions of partial melting are actively debated among petrologists. Except for the study of *in situ* examples of partial melting during high-T metamorphism, unravelling the source region characteristics is based on indirect approaches. In the case of alkaline magmatic rocks, a wealth of geochemical and some phase equilibrium constraints can be derived from their major and especially trace element geochemistry and radiogenic isotope compositions (e.g. Greenough, 1988; Wedepohl *et al.*, 1994; Furman, 1995; Späth *et al.*, 2001). Studies of entrained mantle xenoliths have revealed minimum P–T conditions of formation of alkaline mafic and ultramafic magmas (e.g. Boyd, 1973; Henjes-Kunst & Altherr, 1992; Akinin *et al.*, 1997; Lee & Rudnick, 1999; MacKenzie & Canil, 1999; Kopylova & Caro, 2004). Additionally, a number of experimental investigations have been conducted that focused on their high-pressure liquidus phase relations (e.g. Bultitude & Green, 1971; Green, 1973; Brey & Green, 1977; Adam, 1990; Girnis *et al.*, 1995; Ulmer & Sweeney, 2002). Liquidus experiments can provide direct insights into the nature of the phase assemblages in the source regions. However, they commonly assume homogeneity and thermodynamic equilibration of the source region and a given set of P–T conditions, and the fluid composition is determined *a priori*. Although either approach - geochemical, xenolith-based, and experimental - has its strengths and weaknesses, neither allows study of the source region mineral assemblages directly in a natural environment.

Alkaline mafic and ultramafic magmas are generally considered to rise rapidly to the Earth's surface. Their ascent to the surface is often accompanied by the entrainment of significant amounts of disintegrated rocks from the walls of the magma conduit as xenoliths and xenocrysts. Typical magmas that bear such debris are kimberlites, foidites and alkali basalts (for reviews, see Sobolev, 1977; Dawson, 1980; Nixon, 1987; Menzies, 1990; Griffin *et al.*, 1999). At the same time, many kimberlite, foidite and alkali basalt intrusions are almost devoid of xenoliths but contain abundant macrocrysts of olivine (kimberlites) or olivine and clinopyroxene (olivine nephelinites, basanites) showing strong indications of solid-state deformation such as kink-bands, undulose extinction, recrystallization and internal cracks (e.g. Skinner, 1989; Mitchell, 1995). These minerals are neither the products of fragmentation of mantle xenoliths, because of the lack of other minerals typical of common mantle lithologies, nor could they have crystallized from the host magma, because of their deformation features. This raises the question of whether they are entrained directly from the source region of the host magma. If so, they could provide direct constraints on the phase composition, trace element characteristics and, potentially, the P–T conditions of the source region.

This study focuses on a suite of macrocrysts and clinopyroxene–olivine aggregates from a single specimen of olivine nephelinite from the Humberg, Kaiserstuhl (Baden, Germany). The suite is dominated by clinopyroxene and olivine. Deformation features in olivine from the clinopyroxene–olivine aggregates, as well as the chemical composition of silicate melt inclusions in the clinopyroxene, preclude their crystallization from the host magma. Compared with early formed clinopyroxene phenocrysts that display unequivocal relationships with the host magma (oscillatory zoning, euhedral shape, crystal clots), clinopyroxene macrocrysts and most clinopyroxenes intergrown with deformed olivine show clear similarities in major and trace element composition. This study targets this potential source region material. We present and discuss constraints on the genesis of the host olivine nephelinite magma and the history of formation of its source region via the fragments preserved in the rock. Based on this approach, we show that the process of carbonatite metasomatism of mantle peridotite lithologies defined by the solidus reactions in the system lherzolite–CO_2 under uppermost mantle conditions (<20–22 kbar) can yield an appropriate source region for the olivine nephelinite magma, a hypothesis that has previously been suggested by Dunworth & Wilson (1998) to explain the origin of olivine melilitites of the Upper Rhine graben volcanic province.

GEOLOGY

The Kaiserstuhl volcanic complex has a long history of geological investigation (von Dietrich, 1783; see reviews by Wimmenauer, 1957; Keller *et al.*, 1990; Sigmund, 1996). It is situated within the Upper Rhine Graben (Southern Germany, Fig. 1a) and is one of numerous manifestations of Tertiary to Quaternary volcanism within western and central Europe (Wilson & Downes, 1992; Wedepohl *et al.*, 1994). The main phase of volcanic activity in the Kaiserstuhl occurred in Miocene times between 18 and 13 Myr ago (Lippolt *et al.*, 1963; Schleicher & Keller, 1991; Kraml *et al.*, 1995). Major rock types emplaced during this period are olivine nephelinite and basanite (including type-locality limburgite), tephrite and essexite, phonolite, sövite and alvikite carbonatite (Wimmenauer, 1957, 1959, 1962, 1963; Keller, 1984; Keller *et al.*, 1990; see Fig. 1b). Volumetrically insignificant carbonate-rich melilite dike rocks (bergalites) are also present. The olivine nephelinites are regarded as primitive mantle-derived magmas, whereas limburgites are interpreted as their differentiates (Keller, 1978; Keller *et al.*, 1990). Whole-rock Nd and Pb isotopic data indicate disequilibrium between the olivine nephelinites and carbonatites, whereas their Sr isotopic compositions are fairly similar (Schleicher *et al.*, 1990, 1991; Schleicher & Keller, 1991). The bergalites have isotope

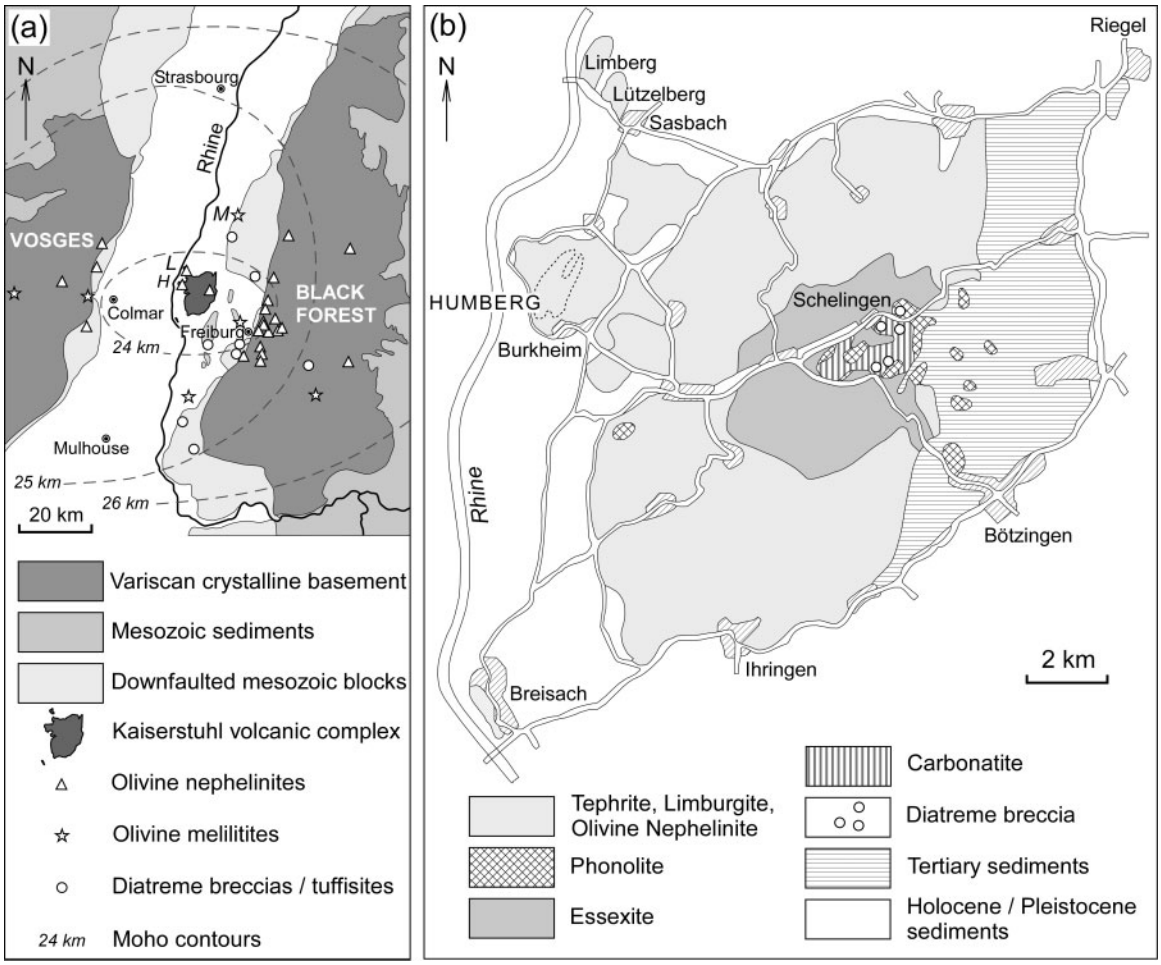

Fig. 1. (a) Geological map of the southern part of the Upper Rhine graben showing the principal geological units and the occurrences of alkaline volcanic rocks (after Keller *et al.*, 2002). L, Lützelberg; H, Humberg; M, Mahlberg. (b) Simplified geological map of the Kaiserstuhl (after Wimmenauer, 1962).

characteristics similar to the carbonatites (Hubberten *et al.*, 1988; Schleicher *et al.*, 1990, 1991).

The olivine nephelinites sometimes contain peridotite xenoliths (Keller *et al.*, 1990, 1997; Sigmund, 1996). Most of these are spinel peridotites; garnet–spinel peridotites are exceptionally rare. Porphyroclastic textures are not observed, although clear indications of strain (undulose extinction, cracked zones and cataclastic zones at the rims of large mineral grains) are common (Sigmund, 1996; Keller *et al.*, 1997). Geothermobarometric estimates indicate temperatures of 950–1100°C (Sigmund, 1996; Keller *et al.*, 1997). The maximum pressure range for spinel-bearing lithologies, calculated based on Cr contents in spinel, does not exceed 22 kbar (Sigmund, 1996; Keller *et al.*, 1997). Garnet-bearing xenoliths yield temperatures of *c.* 1000–1050°C at pressures of 16–24 kbar, depending on the geobarometer used (Sigmund, 1996; Keller *et al.*, 1997). The Al-in-Opx geobarometer of Brey & Köhler (1990) confines this range to *c.* 16–18 kbar, or 53–60 km depth, which probably reflects the limit of garnet stability in mantle peridotites beneath the Kaiserstuhl (Sigmund, 1996; Keller *et al.*, 1997).

The Moho beneath the Kaiserstuhl has been detected by seismic refraction studies at a depth of only *c.* 24 km; there are clear indications of a broad mantle upwarp in the region of the Kaiserstuhl corresponding to the Black Forest–Vosges dome in the surface geology (Edel *et al.*, 1975; Koch, 1993; see Fig. 1a). Gravity modelling (Kahle & Werner, 1980) and electromagnetic deep soundings (Haak *et al.*, 1970; Scheelke, 1974; Winter, 1974) also suggest that a mantle upwarp, centred beneath the Kaiserstuhl, underlies the Upper Rhine Graben (Illies, 1970, 1975). However, available seismic tomography data do not allow assignment of this dome-like structure to an actively upwelling upper mantle diapir and reveal a heterogeneous zone in the depth range of 25–50 km ascribed to partial melts that intruded the mantle lithosphere during the middle and late Miocene and have cooled and solidified since then

(Glahn & Granet, 1992). This zone shows a rather smooth transition to the upper asthenosphere below 50 km (Glahn & Granet, 1992).

This study is based on a single drill-core sample (70 mm × 53 mm) of olivine nephelinite from the locality of Humberg situated in the western part of the Kaiserstuhl complex (Fig. 1b). This locality is known for the presence of essexite rocks and weathered tephrite lavas and tuffs, formerly mined in several quarries, which are now derelict. Olivine nephelinite has not been reported in surface outcrop. However, it crops out c. 4½ km north of the Humberg, in the area of Lützelberg and Limberg, near Sasbach (Fig. 1b). The Lützelberg is the largest and most prominent occurrence of olivine nephelinite rocks in the Kaiserstuhl. It contains abundant spinel peridotite xenoliths (Keller, 1984; Keller *et al.*, 1990). Both the Lützelberg and the Humberg represent paleovolcanic edifices elongated in a NNE–SSW direction, following the orientation of lineaments of the Upper Rhine graben (Fig. 1a and b). The study sample has a fresh and compact appearance. It does not show indications of atmospheric weathering, unlike samples from most local surface outcrops. In terms of chemical composition, it exhibits a remarkable similarity to the Lützelberg olivine nephelinite (Table 1; see Keller *et al.*, 1990). Based on the geological situation (Fig. 1b) and available geochemical data (Table 1), we consider that it may come from the feeder dike system of the Lützelberg olivine nephelinite volcano.

The drill-core sample investigated in this study was taken from the collection of alkaline volcanic rocks initially belonged to Eugen Wegmann and now kept at the University of Neuchâtel, Switzerland. The archiving of specimens in this collection dates to 1961.

Table 1: Major and trace element abundances in the studied olivine nephelinite (H); for comparison, major element abundances in olivine nephelinite from the Lützelberg (L) are also reported

	H	L		H
XRF			*LA-ICPMS (continued)*	
SiO_2	40·41	40·79	Zn	121 (3)
TiO_2	2·62	2·55	Sc	20·7 (0·2)
Al_2O_3	9·55	10·16	V	243 (2)
$Fe_2O_3^*$	11·64	11·67	Rb	26·7 (0·2)
MnO	0·16	0·16	Sr	879 (4)
MgO	15·00	14·50	Y	18·3 (0·2)
CaO	11·36	11·50	Zr	179 (1)
Na_2O	2·24	2·99	Nb	73·5 (0·2)
K_2O	0·64	0·83	Cs	1·26 (0·06)
P_2O_5	0·69	0·77	Ba	679 (3)
LOI	4·29	3·75	La	61·6 (0·1)
H_2O^+	1·36	n.d.	Ce	109 (1)
Total	99·96	99·67	Pr	11·76 (0·04)
Mg-no.	71·9		Nd	46·8 (0·7)
Ni	403		Sm	8·2 (0·3)
Cu	69		Eu	2·62 (0·03)
Zn	96		Gd	6·3 (0·2)
Rb	25		Tb	0·87 (0·02)
Sr	921		Dy	4·3 (0·1)
Ba	609		Ho	0·73 (0·04)
Y	20		Er	1·67 (0·05)
Zr	198		Tm	0·20 (0·01)
Nb	79		Yb	1·18 (0·04)
LA-ICPMS			Lu	0·16 (0·01)
(averages from 4 shots)			Hf	4·2 (0·2)
Li	56·8 (0·9)		Ta	3·78 (0·04)
B	13·0 (0·6)		Pb	5·1 (0·3)
Cr	279 (10)		Th	7·0 (0·1)
Ni	449 (10)		U	2·24 (0·09)
Co	77·3 (0·1)		$(Ce/Yb)_n$	25·7

Element oxides in wt %; trace elements in μg/g. Major element analysis L of the Lützelberg olivine nephelinite is taken from Keller *et al.* (1990). LOI, loss on ignition; n.d., no data. Mg-number = $100 \times Mg/(Mg + Fe^{total})$. Values in parentheses are 1σ standard deviations.
*Total Fe is reported as Fe_2O_3.

ANALYTICAL TECHNIQUES

Major element compositions of minerals were determined by wavelength-dispersive analysis using a four-spectrometer CAMECA SX50 electron microprobe at the Institute of Geological Sciences, University of Bern. The microprobe was operated at 15 kV. Beam currents were 20 nA for most silicate and oxide minerals and 10 nA for carbonate minerals. Compositions of olivine, clinopyroxene and spinel were obtained using spot analyses. For phyllosilicates and carbonate minerals, the electron beam was rastered over an area up to ~10 μm × 15 μm. Major element compositions of quenched carbonatite melt and silicate glass were determined by wavelength-dispersive analysis using the electron microprobe at the University of Bern, and a five-spectrometer JEOL JXA-8200 electron microprobe at the Institute of Mineralogy and Petrography, University of Lausanne. Operating conditions involved a 15 kV accelerating voltage and a 6–10 nA beam current. The beam was rastered over an area 10 μm in diameter. Count times were 10 s for alkalis and silicon and 15–20 s for other elements. Intensity vs time scans performed under these conditions did not reveal any appreciable alkali loss. Data were reduced with the PAP program. Trace element contents of minerals were analysed using a laser ablation inductively coupled plasma mass spectrometry (LA-ICPMS) instrument equipped

with a 193 nm ArF excimer laser (Lambda Physik, Germany) and an ELAN 6100 quadrupole ICPMS system (Perkin Elmer, Canada) at the Institute of Isotope Geochemistry and Mineral Resources, ETH Zürich (see Günther *et al.*, 1997; Heinrich *et al.*, 2003). Operating conditions were similar to those described by Pettke *et al.* (2004). An SRM 610 external standard from NIST was used. Electron microprobe data were used for internal standardization. Whole-rock major element abundances in the host olivine nephelinite were determined using a Philips PW2400 X-ray fluorescence (XRF) spectrometer (Institut de Minéralogie et Pétrographie, University of Fribourg). Trace element abundances were determined on flux-free glass pills using the same LA-ICPMS technique as for minerals. Additionally, some trace elements were analysed by XRF at the University of Fribourg.

BULK CHEMICAL COMPOSITION AND CLASSIFICATION OF THE OLIVINE NEPHELINITE

The sample is classified as an olivine nephelinite because of the frequent presence of olivine macrocrysts, high amount of modal nepheline and lack of modal feldspar, as suggested by the IUGS classification for volcanic rocks (Le Maitre *et al.*, 2002). The bulk-rock major and trace element contents are given in Table 1. In terms of major elements, the rock studied broadly compares with nephelinitic rocks from other localities (Le Bas, 1989, and references therein). Compared with the average olivine (mela)nephelinites of Nockolds (1954) and Le Bas (1987), it is characterized by a somewhat elevated MgO content and a depletion in alkalis, in particular K_2O. The alkali depletion of the studied specimen is also evident when compared with the Lützelberg olivine nephelinite, Kaiserstuhl (Table 1). This is related to the partial replacement of nepheline by analcime in the rock matrix. The elevated MgO content probably reflects the presence of large amounts of olivine macrocrysts. The elevated abundances of incompatible trace elements generally match those for nephelinitic rocks from other occurrences (e.g. Wedepohl *et al.*, 1994; Furman, 1995; Späth *et al.*, 2001). The relatively low Cr content indicates the lack of extensive contamination by xenocrysts derived from depleted mantle lithologies, and the elevated content of Ni reflects the abundance of olivine in the rock.

PETROGRAPHY OF THE OLIVINE NEPHELINITE

The studied rock sample consists of clinopyroxene, olivine and Cr-spinel–Ti-magnetite macrocrysts set in a fine-grained matrix. The matrix is composed of olivine microphenocrysts, clinopyroxene, phlogopite, nepheline, analcime, Ti-magnetite, ilmenite, apatite and calcite. Dominant phases are clinopyroxene, nepheline and analcime. Clinopyroxene forms microphenocrysts (40–50 μm) and microlites (<10–15 μm). The latter are abundant and define the texture of the matrix. Nepheline and analcime occur as interstitial minerals. Nepheline is partly replaced by analcime. Olivine is subordinate and partly or completely replaced by saponite, serpentine and other secondary phyllosilicates. Poikilitic, texturally late phlogopite occurs infrequently. Ti-magnetite and less common ilmenite constitute the major oxide minerals of the matrix and often form intergrowths. Rare segregations and veinlets of calcite are present. Representative microprobe analyses of the matrix minerals are provided in Table 2.

MACROCRYSTS AND MINERAL AGGREGATES

The studied suite of macrocrysts and mineral aggregates is dominated by olivine and clinopyroxene. Cr–Al-spinel and titanomagnetite are minor phases (*c.* 5% of all macrocrysts), with titanomagnetite often forming overgrowths on Cr–Al-spinel. The macrocrysts and aggregates do not exceed 3–4 mm in size (Fig. 2a–f). They account for *c.* 15% of the rock. Individual macrocrysts are more common than aggregates. Core areas of the macrocrysts show distinct chemical compositions, whereas their rims are indistinguishable from matrix microphenocrysts.

Large mantle xenoliths and megacrysts are absent, as well as clinopyroxene macrocrysts compositionally similar to clinopyroxene from common peridotite lithologies. Garnet, orthopyroxene, ilmenite, amphibole and other minerals that can potentially occur as macrocrysts in alkaline mafic and ultramafic magmas have not been found. Green-core clinopyroxene, which often forms macrocrysts in alkaline basalts (e.g. Duda & Schmincke, 1985; Dobosi & Fodor, 1992; Pilet *et al.*, 2002), is similarly absent.

Olivine and spinel

Olivine is abundant among the macrocrysts (Fig. 2a) and is also a major constituent of clinopyroxene–olivine aggregates (Fig. 2b). In both cases, deformed olivine with kink-bands and undulose extinction is common. Large olivine grains (>1 mm) often contain homogeneous cores (Mg-number 90–91·5, 0·08–0·14 wt % CaO). Towards the contact with the host olivine nephelinite, strong chemical zoning is observed. The Mg-numbers and Ni content decrease, whereas the Mn and Ca contents increase (Table 3).

Rare macrocrysts of Cr–Al-spinel–Ti-magnetite consist of anhedral cores of Cr–Al-rich, low-Ti spinel rimmed by a zone of Cr–Al-poor Ti-magnetite (Fig. 2c; Table 4). The cores are usually homogeneous. At the contact

Table 2: Representative electron microprobe analyses of matrix minerals from the studied olivine nephelinite

	Cpx (5 an.)	Ol core	Ol rim	Phl core	Phl intermed.	Phl rim	Ne	Anm	Cc	Ti-Mgt	Ti-Mgt	Ilm
SiO_2	44·59 (0·30)	39·32	38·91	32·15	35·80	37·13	43·19	55·54	0·02	0·03	0·05	0·02
TiO_2	4·05 (0·11)	n.d.	0·05	10·62	11·16	9·46	n.a.	n.a.	n.a.	21·66	14·39	52·79
Al_2O_3	7·98 (0·14)	n.d.	0·02	14·12	12·93	12·63	34·16	23·85	n.a.	1·98	3·23	n.d.
Cr_2O_3	0·17 (0·13)	n.d.	n.d.	0·04	0·08	0·03	n.a.	n.a.	n.a.	0·86	0·95	0·09
Fe_2O_3							0·90	0·42		26·20	38·53	8·55
FeO	6·94 (0·20)	18·84	20·03	11·11	11·45	10·86			0·08	45·23	40·41	27·78
MnO	0·09 (0·02)	0·43	0·45	0·11	0·03	0·12	n.a.	n.a.	0·29	0·81	0·38	1·25
NiO	0·03 (0·02)	0·14	0·13	n.a.	n.a.	n.a.	n.a.	n.a.	n.a.	0·15	0·15	0·04
ZnO	n.a.	n.a.	n.a.	n.a.	n.a.	n.a.	n.a.	n.a.	n.a.	0·03	0·12	n.d.
MgO	12·15 (0·06)	41·85	40·92	12·88	14·41	14·86	0·05	0·08	0·41	3·49	2·30	10·30
CaO	23·38 (0·16)	0·64	0·59	0·03	n.d.	0·13	1·59	0·24	54·43	0·12	0·51	0·03
SrO	n.a.	n.a.	n.a.	n.a.	n.a.	n.a.	n.a.	n.a.	0·33	n.a.	n.a.	n.a.
BaO	n.a.	n.a.	n.a.	8·01	1·66	0·42	n.d.	n.d.	0·07	n.a.	n.a.	n.a.
Na_2O	0·60 (0·04)	0·03	0·03	0·61	0·90	0·76	16·11	12·98	0·03	n.d.	0·04	n.d.
K_2O	0·01 (0·01)	n.d.	0·02	6·23	8·42	9·06	4·60	0·10	n.a.	0·01	n.d.	n.d.
Total	99·99	101·26	101·17	95·91	96·84	95·46	100·60	93·20	55·65	100·58	101·05	100·86
Si	1·680	0·996	0·992	4·995	5·275	5·483	4·111	1·999	0·000	0·001	0·002	0·000
Ti	0·115	0·000	0·001	1·241	1·236	1·050				0·588	0·392	0·924
Al	0·354	0·000	0·001	2·585	2·245	2·198	3·832	1·011		0·084	0·138	0·000
Cr	0·005	0·000	0·000	0·005	0·010	0·004				0·024	0·027	0·002
Fe^{3+}							0·065	0·011		0·712	1·051	0·150
Fe^{2+}	0·219	0·399	0·427	1·444	1·411	1·341			0·001	1·366	1·225	0·541
Mn	0·003	0·009	0·010	0·014	0·004	0·015			0·004	0·025	0·012	0·025
Ni	0·001	0·003	0·003							0·004	0·004	0·001
Zn										0·001	0·003	0·000
Mg	0·682	1·580	1·556	2·983	3·165	3·270	0·007	0·004	0·010	0·188	0·124	0·357
Ca	0·944	0·017	0·016	0·005	0·000	0·020	0·162	0·009	0·980	0·005	0·020	0·001
Sr									0·003			
Ba				0·488	1·583	0·024	0·000	0·000	0·000			
Na	0·044	0·001	0·001	0·184	0·096	0·217	2·973	0·905	0·001	0·000	0·003	0·000
K	0·000	0·000	0·001	1·234	0·258	1·707	0·558	0·005		0·000	0·000	0·000
Sum	4·048	3·005	3·007	15·178	15·282	15·329	11·707	3·945	1·000	3·000	3·000	2·000
O	6	4	4	22	22	22	16	6		4	4	3
Mg-no.	75·7	79·8	78·5	67·4	69·2	70·9				12·1	9·2	39·8

Oxides in wt %; an., analyses; n.d., not detected; n.a., not analysed. For mafic silicates, total Fe is given as FeO. For Ti-magnetite and ilmenite, Fe_2O_3 and FeO were calculated assuming ideal stoichiometry. For nepheline and analcime, total Fe is given as Fe_2O_3. Cpx, clinopyroxene; Ol, olivine; Phl, phlogopite; Ne, nepheline; Anm, analcime; Cc, calcite; Ti-Mgt, Ti-rich magnetite; Ilm, ilmenite. Values in parentheses are 1σ standard deviations. Mg-number $= 100 \times Mg/(Mg + Fe^{2+})$.

between the core and the rim, strong chemical zoning is observed. Microprobe profiles of olivine and spinel are available as an Electronic Appendix at http://www.petrology.oxfordjournals.org (Figs A1 and A2, respectively).

Clinopyroxene

Clinopyroxenes can be divided in three groups. Their main characteristics are summarized in Table 5. Chemical compositions are given in Tables 6–9. Petrographic and major and trace element geochemical data are presented in Figs 2–8. A comprehensive set of petrographic data and electron microprobe profiles is available as an Electronic Appendix at http://www.petrology.oxfordjournals.org (Figs A3–A10, Table A1).

Cpx I is very rare and forms partially resorbed grains in the inner parts of some clinopyroxene–olivine aggregates (Fig. 2b). Such relict grains are almost devoid of inclusions

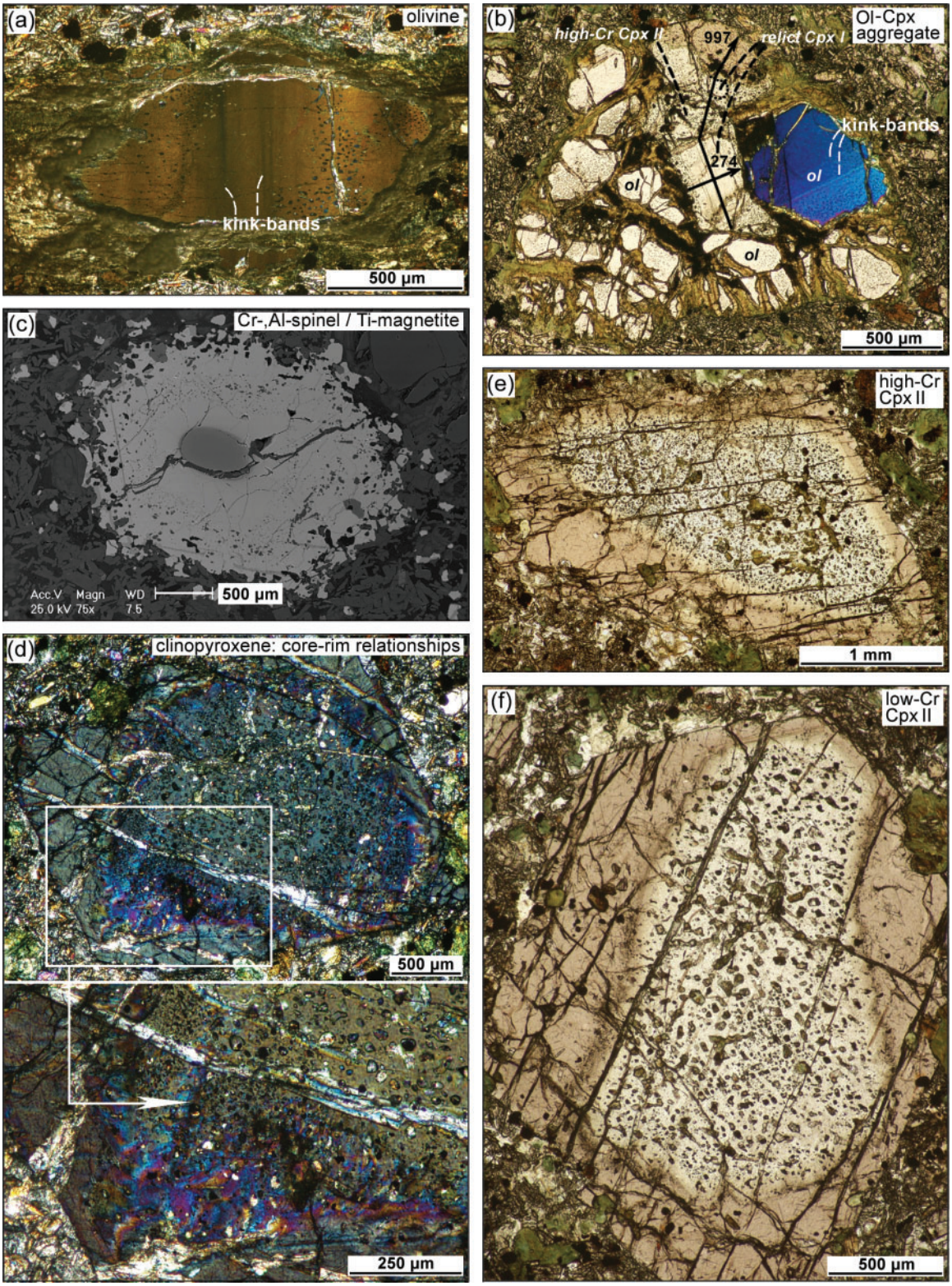

Fig. 2. Photomicrographs and backscattered electron image of macrocrysts and mineral aggregates in the studied olivine nephelinite. (a) Olivine (cross-polarized light). Undulose extinction and kink bands are well developed. (b) Clinopyroxene–olivine aggregate 997/274 (plane-polarized light; one olivine grain from a superimposed complementary photomicrograph in cross-polarized light). The inner part of the aggregate is formed of relict Cpx I that is partly replaced by high-Cr Cpx II containing frequent inclusions. Along the outer rim of the aggregate, Cpx II is mantled by a zone of pale brownish Ti–Al-rich clinopyroxene chemically indistinguishable from the matrix clinopyroxene. Olivine is deformed (kink-bands). Black lines indicate locations of microprobe profiles (see Fig. 5a). (c) Backscattered electron image of a Ti-magnetite macrocryst with a Cr–Al-rich spinel core. (d) High-Cr Cpx II, macrocryst 1426 (cross-polarized light). Clinopyroxene domains with different optical orientations are well developed owing to the angular shape of the core area; their propagation inwards along a crack is visible. (e, f) High-Cr and low-Cr Cpx II, macrocrysts 1610 and 3484, respectively (plane-polarized light). Colourless core areas with abundant inclusions are clearly distinguishable, as well as pale brownish Ti–Al-rich mantles.

of other phases and are characterized by a distinctive chemical composition. Cpx I is magnesian, enriched in Cr and Na, depleted in Ca and strongly depleted in Ti (Tables 5 and 6). It is fairly homogeneous in terms of its major element composition (Fig. 5a). In terms of trace elements, it displays strong light rare earth element (LREE) enrichment and heavy REE (HREE) depletion (Table 7), resulting in an almost 'straight-line' appearance of the REE patterns (Fig. 6a). In the multi-element patterns, pronounced negative anomalies of Nb, Zr, Hf and Ti are present (Fig. 6b).

Cpx II is common and clearly dominates the studied assemblage. It forms macrocrysts and occurs in clinopyroxene–olivine aggregates, partially replacing relict Cpx I when the latter is also present. A typical macrocryst consists of a colorless, anhedral-to-subhedral, resorbed core and a subhedral-to-euhedral pale brownish

Table 3: Representative electron microprobe analyses of olivine macrocrysts and olivine from Cpx–Ol aggregates

	1827-4 macrocryst		1827-1 aggregate		1827-10 aggregate	
	core plateau?*	rim	core plateau	rim	core plateau	rim
SiO_2	41·16	39·14	41·10	38·85	41·22	40·02
TiO_2	n.d.	0·04	n.d.	0·01	n.d.	0·01
Al_2O_3	0·02	0·02	0·01	0·05	0·01	0·03
Cr_2O_3	0·03	0·01	0·04	n.d.	0·05	n.d.
FeO_{total}	9·73	19·63	9·24	18·96	8·67	14·98
MnO	0·14	0·43	0·21	0·47	0·11	0·26
NiO	0·29	0·17	0·42	0·14	0·37	0·3
MgO	50·04	41·57	50·13	41·56	50·80	45·23
CaO	0·09	0·54	0·07	0·50	0·07	0·44
Total	101·50	101·57	101·24	100·53	101·30	101·27
Si	0·994	0·992	0·994	0·992	0·993	0·994
Ti	0·000	0·001	0·000	0·000	0·000	0·000
Al	0·001	0·001	0·000	0·001	0·000	0·001
Cr	0·001	0·000	0·001	0·000	0·001	0·000
Fe^{2+}	0·197	0·416	0·187	0·405	0·175	0·311
Mn	0·003	0·009	0·004	0·010	0·002	0·005
Ni	0·006	0·003	0·008	0·003	0·007	0·006
Mg	1·802	1·571	1·808	1·582	1·825	1·675
Ca	0·002	0·015	0·002	0·014	0·002	0·012
Sum	3·005	3·007	3·005	3·007	3·006	3·005
Mg-no.	90·1	79·1	90·6	79·6	91·3	84·3

Oxides in wt %; n.d., not detected. Total Fe is given as FeO. Mg-number $= 100 \times Mg/(Mg + Fe^{2+})$.
*The corresponding electron microprobe profile does not show a distinct plateau, although the extent of diffusion re-equilibration is probably insignificant.

Table 4: Representative major and trace element analyses of Cr–Al-spinel–Ti-magnetite macrocrysts

	1827-7-1		1827-7-1		1827-7-2	
	core no plateau	rim	core plateau	rim	core plateau	rim
EMPA						
SiO_2	0·04	0·04	0·06	0·30	0·10	0·06
TiO_2	0·66	15·85	0·52	17·86	0·23	15·86
Al_2O_3	19·78	4·48	25·71	4·81	37·10	4·08
Cr_2O_3	39·08	2·71	36·29	4·02	22·43	2·61
Fe_2O_3	9·80	32·97	6·87	27·41	9·26	33·82
FeO	21·91	38·44	19·88	38·64	18·27	38·13
MnO	0·40	0·49	0·34	0·48	0·30	0·40
NiO	0·07	0·22	0·09	0·15	0·11	0·27
ZnO	0·23	0·03	0·23	0·18	0·44	n.d.
MgO	8·69	4·85	10·60	6·16	12·51	5·09
CaO	n.d.	0·02	n.d.	0·04	n.d.	0·10
Na_2O	n.d.	n.d.	n.d.	n.d.	0·04	n.d.
Total	100·65	100·09	100·59	100·04	100·79	100·42
Si	0·001	0·001	0·002	0·011	0·003	0·002
Ti	0·016	0·425	0·012	0·472	0·005	0·424
Al	0·744	0·188	0·931	0·199	1·269	0·171
Cr	0·986	0·076	0·882	0·112	0·515	0·073
Fe^{3+}	0·236	0·884	0·159	0·725	0·202	0·904
Fe^{2+}	0·585	1·145	0·511	1·135	0·443	1·133
Mn	0·011	0·015	0·009	0·014	0·007	0·012
Ni	0·002	0·006	0·002	0·004	0·002	0·008
Zn	0·005	0·001	0·005	0·005	0·009	0·000
Mg	0·414	0·258	0·486	0·322	0·541	0·269
Ca	0·000	0·001	0·000	0·002	0·000	0·004
Na	0·000	0·000	0·000	0·000	0·002	0·000
Sum	3·000	3·000	3·000	3·000	3·000	3·000
Mg-no.	41·4	18·4	48·7	22·1	55·0	19·2
LA-ICPMS						
Li	2·6	n.a.	3·6	17	4·4	n.a.
B	7·7	n.a.	7·4	<2·6	13	n.a.
Sc	0·69	n.a.	0·64	4·6	0·37	n.a.
V	873	n.a.	845	2159	638	n.a.
Co	273	n.a.	288	247	274	n.a.
Ni	648	n.a.	814	1278	1335	n.a.
Y	<0·015	n.a.	0·047	0·063	<0·041	n.a.
Zr	<1·1	n.a.	<0·89	54	<0·80	n.a.
Nb	<0·70	n.a.	<0·83	64	<0·45	n.a.
La	<0·015	n.a.	<0·014	0·095	<0·045	n.a.
Ce	<0·020	n.a.	0·033	0·15	0·092	n.a.
Pr	0·011	n.a.	0·008	0·036	0·024	n.a.
Nd	0·082	n.a.	0·055	0·14	0·12	n.a.

(continued)

Table 4: Continued

	1827-7-1		1827-4		1827-7-2	
	core no plateau	rim	core plateau	rim	core plateau	rim
Sm	<0·075	n.a.	<0·040	<0·11	0·20	n.a.
Eu	0·031	n.a.	0·010	<0·023	<0·055	n.a.
Gd	<0·038	n.a.	0·055	<0·095	<0·16	n.a.
Tb	<0·006	n.a.	0·009	<0·013	<0·029	n.a.
Ho	<0·015	n.a.	<0·013	0·019	<0·014	n.a.
Tm	<0·013	n.a.	0·008	<0·012	<0·022	n.a.
Yb	<0·080	n.a.	<0·042	0·066	<0·12	n.a.
Lu	0·008	n.a.	0·007	<0·013	<0·024	n.a.
Hf	0·045	n.a.	<0·041	1·2	0·094	n.a.
Ta	0·021	n.a.	0·038	5·1	0·022	n.a.
Pb	<0·079	n.a.	0·16	<0·078	0·24	n.a.
Th	<0·007	n.a.	0·006	0·041	<0·022	n.a.
U	<0·007	n.a.	0·011	0·024	0·078	n.a.

Oxides in wt %; trace elements in μg/g; n.d., not detected; n.a., not analysed. Fe_2O_3 and FeO were calculated assuming ideal stoichiometry. Mg-number = $100 \times Mg/(Mg + Fe^{2+})$.

mantle (Fig. 2d–f). No oscillatory zoning in the core area is observed. The mantle can sometimes show oscillatory zoning. In larger macrocrysts, the core area is well developed and optically homogeneous. Closer to the mantle, clinopyroxene forms microscopic domains with different optical orientation, which penetrate the core and define an intermediate zone between the core and the mantle (Fig. 2d). The domain texture tends to spread along cracks and in the corner parts of the core (Fig. 2d), and is therefore unlikely to be a result of direct magmatic crystallization; it appears most consistent with an origin by fast reaction of the clinopyroxene cores with a melt. Small macrocrysts can be entirely overprinted by this process (Fig. 3a and b). Detailed element maps demonstrate that the domain texture is due to the presence of domains characterized by variable chemical compositions (Fig. 3b; for more detail, see Fig. A4 of the Electronic Appendix).

Cpx II from clinopyroxene–olivine aggregates and from the core areas of the macrocrysts are similar. However, the domain texture and outer mantle typical of single Cpx II macrocrysts are not developed in direct contact of Cpx II with olivine, although they are present at its contact with the host olivine nephelinite.

The clinopyroxene cores contain abundant inclusions. Inclusions of fluid, melt and carbonate phases dominate;

Table 5: Systematics of clinopyroxene from the studied olivine nephelinite

Textural setting	Inclusions	Chemical composition*					
		Cr_2O_3	TiO_2	Al_2O_3	CaO	Mg-no.	Zr/Nd
Relict Cpx I							
Aggregates with deformed olivine	no	1·2–1·5	0·1–0·2	3·1–4·0	20·7	91·2–92·2	1·0
High-Cr Cpx II							
Aggregates with deformed olivine, individual macrocrysts	olivine, high-Cr spinel, alkali aluminosilicate glass, calcite, Sr-aragonite, fluid	0·6–1·5	0·1–1·2	2·0–4·3	22·6–23·7	84·7–92·3	1·6–3·2
Low-Cr Cpx II							
Individual macrocrysts	olivine, low-Cr spinel, alkali aluminosilicate glass, calcite Sr-aragonite, apatite, fluid	<0·1	0·9–1·3	3·6–4·5	23·0–23·1	82·5–85·4	2·6–3·8
Cpx III phenocrysts							
Crystal clots and individual crystals with oscillatory zonation	no	<0·6	1·5–1·9	3·1–4·5	22·9–23·8	80·7–87·2	4·2–7·1
Cpx microlites							
Rock matrix	no	0·2	4·1	8·0	23·4	75·7	5·1

*see Tables 2 and 6–9.

Table 6: Representative major element analyses of core areas of clinopyroxene macrocrysts and clinopyroxenes from Cpx–Ol aggregates

	relict Cpx I		high-Cr Cpx II					transitional Cpx		low-Cr Cpx II			
	997/274 (59 an.)	656 (7 an.)	997 (23 an.)	1932 (89 an.)	1610 (18 an.)	1039 (27 an.)	536 (22 an.)	1847 (11 an.)	2308 (90 an.)	3484 (54 an.)	1875 (32 an.)	1774 (15 an.)	1434 (13 an.)
SiO_2	54·12 (0·19)	53·50 (0·11)	54·23 (0·26)	53·23 (0·36)	51·42 (0·53)	50·91 (0·51)	51·66 (0·44)	52·26 (0·18)	52·31 (0·52)	51·13 (0·67)	50·29 (0·27)	49·78 (0·35)	50·40 (0·41)
TiO_2	0·07 (0·01)	0·22 (0·01)	0·10 (0·05)	0·18 (0·03)	0·89 (0·25)	1·15 (0·18)	0·94 (0·13)	0·73 (0·08)	0·64 (0·12)	0·94 (0·09)	0·99 (0·12)	1·40 (0·15)	1·33 (0·22)
Al_2O_3	3·09 (0·07)	3·98 (0·20)	2·03 (0·27)	3·25 (0·45)	3·93 (0·24)	4·33 (0·37)	3·43 (0·45)	3·23 (0·17)	2·86 (0·35)	3·65 (0·29)	3·64 (0·22)	4·37 (0·23)	4·47 (0·31)
Cr_2O_3	1·52 (0·08)	1·17 (0·07)	1·43 (0·19)	1·53 (0·10)	0·69 (0·09)	0·93 (0·14)	0·57 (0·08)	0·21 (0·04)	0·45 (0·07)	0·07 (0·04)	0·06 (0·02)	0·04 (0·02)	0·07 (0·02)
FeO	2·62 (0·09)	3·05 (0·12)	2·60 (0·20)	2·56 (0·13)	4·84 (0·16)	4·32 (0·21)	4·02 (0·19)	4·94 (0·17)	4·21 (0·20)	4·86 (0·23)	5·00 (0·15)	5·43 (0·16)	5·58 (0·18)
MnO	0·08 (0·04)	0·11 (0·03)	0·08 (0·03)	0·09 (0·03)	0·10 (0·03)	0·08 (0·03)	0·08 (0·03)	0·11 (0·02)	0·11 (0·03)	0·12 (0·02)	0·10 (0·02)	0·09 (0·03)	0·10 (0·03)
NiO	0·05 (0·03)	0·04 (0·02)	0·04 (0·03)	n.a.	n.a.	0·03 (0·02)	0·03 (0·02)	n.a.	n.a.	n.a.	n.a.	n.a.	n.a.
MgO	17·54 (0·13)	17·69 (0·22)	16·98 (0·36)	17·18 (0·28)	15·08 (0·16)	15·06 (0·36)	16·22 (0·32)	16·00 (0·20)	15·88 (0·28)	15·87 (0·56)	15·31 (0·16)	14·99 (0·16)	14·77 (0·26)
CaO	20·70 (0·12)	20·71 (0·44)	23·14 (0·32)	22·61 (0·31)	23·71 (0·28)	23·71 (0·25)	22·93 (0·32)	23·01 (0·39)	23·07 (0·70)	22·93 (0·73)	23·52 (0·20)	23·82 (0·21)	23·54 (0·25)
Na_2O	1·11 (0·04)	0·99 (0·09)	0·66 (0·08)	0·61 (0·05)	0·59 (0·10)	0·55 (0·06)	0·51 (0·09)	0·50 (0·06)	0·52 (0·06)	0·56 (0·06)	0·48 (0·04)	0·44 (0·05)	0·47 (0·05)
K_2O	0·01 (0·01)	0·03 (0·03)	0·02 (0·06)	0·02 (0·02)	0·01 (0·01)	0·01 (0·01)	0·01 (0·01)	0·01 (0·01)	0·06 (0·28)	0·01 (0·01)	0·01 (0·01)	0·01 (0·01)	0·02 (0·02)
Total	100·91	101·49	101·31	101·19	101·26	101·08	100·41	100·98	100·13	100·15	99·37	100·37	100·75
Si	1·941	1·911	1·949	1·913	1·875	1·858	1·888	1·903	1·917	1·880	1·870	1·840	1·852
Ti	0·002	0·006	0·003	0·005	0·024	0·032	0·026	0·020	0·018	0·026	0·028	0·039	0·037
Al	0·131	0·168	0·086	0·138	0·169	0·186	0·148	0·139	0·124	0·158	0·160	0·190	0·194
Cr	0·043	0·033	0·041	0·043	0·020	0·027	0·016	0·006	0·013	0·002	0·002	0·001	0·002
Fe^{2+}	0·079	0·091	0·078	0·077	0·148	0·132	0·123	0·150	0·129	0·149	0·156	0·168	0·172
Mn	0·002	0·003	0·002	0·003	0·003	0·002	0·002	0·003	0·003	0·004	0·003	0·003	0·003
Ni	0·001	0·001	0·001			0·001	0·001						
Mg	0·938	0·942	0·910	0·920	0·820	0·819	0·884	0·868	0·868	0·870	0·849	0·826	0·809
Ca	0·795	0·793	0·891	0·871	0·926	0·927	0·898	0·898	0·906	0·903	0·937	0·943	0·927
Na	0·077	0·069	0·046	0·043	0·042	0·039	0·036	0·035	0·037	0·040	0·035	0·032	0·033
K	0·000	0·001	0·001	0·001	0·000	0·000	0·000	0·000	0·003	0·000	0·000	0·000	0·001
Sum	4·009	4·018	4·008	4·013	4·027	4·024	4·022	4·023	4·017	4·034	4·039	4·042	4·030
Mg-no.	92·2	91·2	92·1	92·3	84·7	86·1	87·8	85·3	87·1	85·4	84·5	83·1	82·5

Oxides in wt %; n.a., not analysed; an., analyses; for each grain, averages from several tens of electron microprobe measurements are shown; 1σ standard deviations are given in parentheses. Mg-number $= 100 \times Mg/(Mg + Fe^{2+})$, assuming all Fe as Fe^{2+}.

Table 7: Representative trace element analyses of clinopyroxene macrocrysts and clinopyroxenes from Cpx–Ol aggregates

	cores															
	relict Cpx I		high-Cr Cpx II					trans. Cpx II		low-Cr Cpx II				intermediate zones (Cr peaks) and outer rims in Cpx II			
	997/274	656	997	1932	1610	1039	536	1847	2308	3484	1875	1774	1434	1875 intermed.	1875 rim	1434 intermed.	1434 rim
TiO_2	0·049	0·213	0·124	0·158	0·715	1·099	0·890	0·729	0·608	0·860	0·991	1·299	1·149	1·903	3·840	1·761	3·441
MnO	0·067	0·097	0·060	0·087	0·085	0·082	0·095	0·107	0·089	0·097	0·096	0·093	0·095	0·076	0·075	0·082	0·077
K_2O	0·002	0·008	0·001	0·001	0·002	0·001	0·002	0·002	0·001	0·001	0·001	0·001	0·001	0·001	0·001	0·003	0·001
P_2O_5	0·007	0·021	0·009	0·008	0·009	0·016	0·017	0·012	0·010	0·009	0·016	0·015	0·012	0·016	0·018	0·014	0·015
Li	2·3	3·4	1·7	2·7	1·4	<0·63	<1·6	0·50	1·1	<0·39	<0·36	<0·38	0·35	0·65	2·3	0·64	3·1
B	2·3	<11	5·8	<7·9	3·5	6·0	<8·9	5·5	<3·8	5·7	8·4	2·3	4·5	7·3	7·0	6·8	3·9
Sc	53	48	65	60	47	52	49	50	51	49	49	49	45	100	48	96	38
V	176	191	211	229	316	251	224	266	297	316	298	268	296	186	290	199	286
Cr	7800	7592	9628	9987	4424	5371	4248	1265	2594	429	377	258	416	3758	683	3195	576
Co	19	30	22	22	26	28	35	32	25	28	31	30	30	27	27	28	26
Ni	333	469	339	285	217	303	342	250	199	168	138	169	142	134	158	143	147
Zn	9·2	14	13	11	24	25	22	24	21	21	25	27	28	22	29	25	32
Rb	0·008	<0·16	<0·065	<0·12	0·043	<0·067	<0·22	0·085	<0·028	<0·031	<0·071	<0·036	<0·031	<0·044	<0·032	0·25	<0·025
Sr	141	159	306	62	231	235	116	134	206	142	217	250	280	158	349	159	369
Y	3·6	4·2	4·3	8·2	7·2	13	8·0	7·8	5·7	8·9	9·6	11	11	11	25	10	24
Zr	13	19	16	11	19	57	30	30	14	31	42	57	50	101	293	86	263
Nb	0·84	1·1	0·49	0·3	1·1	1·9	0·47	0·44	0·34	0·30	1·2	2·2	1·7	1·4	6·2	1·2	5·7
Cs	<0·004	<0·053	<0·022	<0·045	<0·008	<0·031	0·04	<0·013	<0·024	<0·008	<0·013	<0·008	<0·015	0·013	<0·014	<0·009	<0·013
Ba	0·23	<0·61	0·57	<0·44	0·72	<0·17	<0·38	0·39	<0·26	<0·12	0·33	0·34	<0·11	0·18	0·38	<0·102	0·17
La	7·6	8·3	8·9	2·1	7·1	13	4·1	5·1	4·5	3·3	9·8	14	13	9·1	31	9·3	29
Ce	13	21	18	5·0	18	30	13	13	12	9·6	22	34	32	26	81	25	77
Pr	1·5	2·6	2·2	0·78	2·5	3·9	2·0	2·0	1·6	1·8	2·6	4·7	4·3	3·8	11	3·5	11

(continued)

Table 7: Continued

	cores																
	relict Cpx I		high-Cr Cpx II					trans. Cpx II		low-Cr Cpx II				intermediate zones (Cr peaks) and outer rims in Cpx II			
	997/274	656	997	1932	1610	1039	536	1847	2308	3484	1875	1774	1434	1875 intermed.	1875 rim	1434 intermed.	1434 rim
Nd	6·6	10	8·6	4·3	12	18	11	10	7·3	8·5	13	21	20	20	56	17	52
Sm	1·3	1·2	1·9	2·0	2·5	3·8	3·4	2·6	2·0	2·4	3·3	4·8	4·4	4·9	12	3·9	12
Eu	0·49	0·45	0·73	0·46	1·0	1·5	0·94	0·93	0·77	0·88	1·2	1·8	1·6	1·5	3·7	1·7	3·6
Gd	1·2	1·7	1·5	1·2	2·3	3·6	1·9	2·3	2·0	2·2	2·9	4·0	4·3	4·4	10	4·3	9·5
Tb	0·18	0·37	0·25	0·24	0·28	0·65	0·31	0·37	0·18	0·45	0·45	0·57	0·59	0·60	1·2	0·52	1·2
Dy	0·79	1·0	1·1	1·9	1·4	3·0	2·1	1·8	1·1	1·8	2·2	2·6	2·5	2·9	6·5	3·1	6·6
Ho	0·17	0·18	0·19	0·28	0·35	0·63	0·34	0·31	0·22	0·37	0·41	0·46	0·42	0·47	1·1	0·31	0·95
Er	0·30	0·55	0·53	0·81	0·75	1·3	0·76	0·91	0·77	0·80	0·83	0·98	1·07	1·0	2·6	0·92	2·1
Tm	0·037	0·12	0·065	0·088	0·079	0·15	0·065	0·12	0·038	0·11	0·062	0·11	0·11	0·12	0·26	0·11	0·22
Yb	0·24	0·37	0·42	n.d.	0·58	0·93	0·68	0·47	0·64	0·69	0·52	0·70	0·73	0·70	1·5	0·87	1·7
Lu	0·039	0·12	<0·039	0·11	0·039	0·084	<0·034	0·048	0·045	0·056	0·10	0·075	0·14	0·062	0·22	0·11	0·24
Hf	0·29	<0·27	0·28	0·42	0·72	1·6	1·5	1·3	0·76	1·5	1·9	1·7	1·9	4·2	8·8	3·7	7·2
Ta	0·11	0·12	0·072	<0·063	0·13	0·36	0·084	0·087	0·064	0·020	0·13	0·36	0·19	0·28	1·4	0·20	1·1
Pb	0·22	<0·49	<0·13	<0·35	<0·10	0·15	<0·37	<0·12	0·27	<0·099	0·15	0·85	<0·072	<0·078	0·085	0·11	0·094
Th	0·37	0·50	0·13	0·19	0·064	0·16	0·082	0·065	<0·016	0·037	0·11	0·22	0·17	0·23	0·54	0·18	0·49
U	0·060	0·14	<0·029	<0·069	<0·01	0·033	<0·035	<0·011	<0·016	<0·010	0·023	0·028	0·013	0·027	0·076	<0·023	0·063
$(Ce/Yb)_n$	15·1	15·3	11·8		8·9	9·0	5·5	7·9	5·1	3·9	11·6	13·4	12·2	10·3	15·1	7·9	12·4
Zr/Nd	2·0	1·9	1·8	2·6	1·6	3·2	2·8	2·9	2·0	3·7	3·2	2·7	2·6	5·1	5·3	4·9	5·0
Ti/Eu	599	2818	1013	2081	4161	4494	5700	4699	4709	5858	4837	4309	4384	7436	6169	6370	5799
Zr/Hf	45·4	>70·9	57·9	27·0	26·4	36·0	20·6	22·7	19·1	20·9	22·1	34·3	27·2	24·0	33·2	23·5	36·7
Nb/Ta	8·0	9·2	6·8	>4·8	8·4	5·3	5·5	5·0	5·4	15·1	9·2	6·1	9·1	4·9	4·5	6·1	5·1

Oxides of selected major elements in wt %; trace elements in μg/g; trans., transitional.

Table 8: Representative major element analyses of clinopyroxene phenocrysts (Cpx III)

	crystal clot 260/109/300/185 and its phenocrysts								phenocryst			phenocryst		phenocryst	
	260			109	300	185			585			1827-3		196	
	rim (3 an.)	interm. (1 an.)	core (7 an.)	core (2 an.)	core (7 an.)	core (3 an.)	interm. (1 an.)	rim (2 an.)	core (5 an.)	interm (1 an.).	rim (3 an.)	core (8 an.)	rim (10 an.)	core (8 an.)	rim (8 an.)
SiO_2	44·94 (0·02)	48·70	51·15 (0·13)	50·70 (0·22)	51·08 (0·25)	50·90 (0·57)	48·64	44·97 (0·13)	49·83 (0·15)	48·82	44·45 (0·10)	50·98 (0·23)	44·97 (0·22)	49·79 (0·30)	44·90 (0·18)
TiO_2	4·01 (0·15)	2·59	1·51 (0·03)	1·54 (0·06)	1·52 (0·04)	1·57 (0·19)	2·57	3·90 (0·18)	1·79 (0·04)	2·13	4·12 (0·05)	1·47 (0·03)	4·09 (0·08)	1·94 (0·07)	4·07 (0·12)
Al_2O_3	7·80 (0·16)	4·91	3·15 (0·09)	3·24 (0·16)	3·23 (0·16)	3·32 (0·20)	4·75	8·03 (0·02)	4·47 (0·10)	5·12	8·03 (0·03)	3·11 (0·07)	8·16 (0·06)	3·82 (0·06)	8·09 (0·15)
Cr_2O_3	0·10 (0·06)	0·13	0·57 (0·02)	0·54 (0·03)	0·57 (0·05)	0·63 (0·05)	0·07	0·10 (0·05)	0·01 (0·01)	0·10	0·13 (0·02)	0·61 (0·02)	0·10 (0·02)	0·33 (0·05)	0·12 (0·02)
FeO	6·78 (0·16)	5·98	4·56 (0·12)	4·20 (0·01)	4·62 (0·21)	4·74 (0·22)	6·27	6·53 (0·03)	6·32 (0·11)	6·09	6·75 (0·08)	4·13 (0·14)	6·26 (0·11)	4·76 (0·04)	6·19 (0·11)
MnO	0·09 (0·04)	0·15	0·07 (0·01)	0·07 (0·03)	0·09 (0·02)	0·09 (0·02)	0·08	0·10 (0·07)	0·10 (0·02)	0·11	0·10 (0·10)	0·07 (0·02)	0·07 (0·01)	0·08 (0·05)	0·06 (0·02)
MgO	12·42 (0·06)	14·32	15·78 (0·09)	16·04 (0·15)	15·69 (0·19)	15·66 (0·16)	14·28	12·84 (0·65)	14·81 (0·19)	14·42	12·22 (0·04)	16·16 (0·20)	12·40 (0·05)	15·28 (0·13)	12·53 (0·12)
CaO	23·49 (0·10)	23·61	23·77 (0·11)	23·83 (0·18)	23·76 (0·07)	23·63 (0·08)	23·69	22·83 (0·75)	23·01 (0·24)	23·03	23·46 (0·06)	23·40 (0·01)	23·34 (0·15)	23·71 (0·11)	23·69 (0·09)
Na_2O	0·60 (0·02)	0·42	0·38 (0·03)	0·37 (0·01)	0·39 (0·04)	0·43 (0·05)	0·43	0·57 (0·00)	0·53 (0·03)	0·49	0·55 (0·02)	0·34 (0·02)	0·63 (0·06)	0·42 (0·03)	0·61 (0·06)
K_2O	0·01 (0·01)	0·01	0·01 (0·01)	0·00 (0·00)	0·00 (0·01)	0·00 (0·01)	n.d.	0·02 (0·00)	0·01 (0·01)	0·01	0·00 (0·00)	0·01 (0·01)	0·00 (0·00)	0·00 (0·00)	0·00 (0·00)
Total	100·24	100·82	100·95	100·53	100·97	100·98	100·79	99·89	100·88	100·31	99·81	100·28	100·02	100·14	100·25
Si	1·687	1·800	1·871	1·861	1·869	1·863	1·801	1·687	1·835	1·810	1·677	1·872	1·686	1·841	1·681
Ti	0·113	0·072	0·042	0·043	0·042	0·043	0·072	0·113	0·050	0·059	0·117	0·041	0·115	0·054	0·115
Al	0·345	0·214	0·136	0·140	0·139	0·143	0·207	0·345	0·194	0·224	0·357	0·135	0·361	0·166	0·357
Cr	0·003	0·004	0·016	0·016	0·016	0·018	0·002	0·003	0·000	0·003	0·004	0·018	0·003	0·010	0·004
Fe^{2+}	0·213	0·185	0·139	0·129	0·141	0·145	0·194	0·213	0·195	0·189	0·213	0·127	0·196	0·147	0·194
Mn	0·003	0·005	0·002	0·002	0·003	0·003	0·003	0·003	0·003	0·003	0·003	0·002	0·002	0·003	0·002
Mg	0·695	0·789	0·860	0·878	0·856	0·855	0·788	0·695	0·813	0·797	0·687	0·885	0·693	0·842	0·699
Ca	0·945	0·935	0·931	0·937	0·931	0·927	0·940	0·945	0·908	0·915	0·948	0·921	0·938	0·939	0·950
Na	0·044	0·030	0·027	0·026	0·028	0·031	0·031	0·044	0·038	0·035	0·040	0·024	0·046	0·030	0·044
K	0·000	0·000	0·000	0·000	0·000	0·000	0·000	0	0·000	0·000	0·000	0·000	0·000	0·000	0·000
Sum	4·048	4·034	4·025	4·032	4·025	4·028	4·038	4·048	4·037	4·035	4·046	4·024	4·040	4·032	4·046
Mg-no.	76·5	81·0	86·1	87·2	85·9	85·5	80·2	76·5	80·7	80·8	76·3	87·5	78·0	85·1	78·3

Oxides in wt %; n.d., not detected; 1σ standard deviations in parentheses. Mg-number = $Mg/(Mg + Fe^{2+})$, assuming all Fe as Fe^{2+}.

Table 9: Representative trace element analyses of clinopyroxene phenocrysts (Cpx III)

	crystal clot 260/109/300/185 and its phenocrysts									phenocryst					phenocryst		phenocryst	
	260			109	300		185			585					1827-3		196	
	rim	interm.	core	core	core	core	core	interm.	rim	interm.	core	core	interm.	rim	core	rim	core	rim
	1	2	3	4	5	6	7	8	9	1	2	3	4	5				
TiO_2	3·202	2·637	1·471	1·872	1·966	1·464	1·965	2·711	3·494	1·977	1·474	1·525	2·410	3·600	1·765	3·752	2·410	3·496
MnO	0·087	0·090	0·072	0·078	0·086	0·072	0·081	0·090	0·087	0·089	0·108	0·107	0·096	0·077	0·085	0·089	0·083	0·087
K_2O	0·011	0·003	0·002	0·005	0·001	0·002	0·002	0·003	0·015	0·001	0·003	0·002	0·002	0·001	0·001	0·002	0·002	0·002
P_2O_5	0·097	0·097	0·015	0·024	0·036	0·016	0·030	0·108	0·064	0·014	0·022	0·021	0·018	0·015	0·020	0·019	0·026	0·019
Li	6·6	3·0	2·3	3·5	<1·8	1·9	2·7	3·3	8·8	2·8	2·9	1·5	2·2	4·1	2·2	5·2	2·2	3·6
B	5·4	5·2	3·7	6·3	<12	5·0	4·8	7·6	7·8	3·6	3·9	6·3	3·9	<2·2	<3·9	<9·8	<5·7	<10·1
Sc	37	65	120	136	146	114	132	54	40	73	70	64	77	42	145	50	129	46
V	285	239	133	160	172	138	169	260	292	254	211	213	295	296	142	313	186	303
Cr	400	368	3208	3025	2706	3743	2399	427	684	373	201	181	360	650	3304	873	1752	692
Co	30	31	26	28	32	27	28	33	32	35	38	38	36	27	31	35	30	28
Ni	155	139	122	133	121	133	124	169	180	166	152	148	154	155	160	210	143	198
Zn	36	31	22	29	28	23	25	35	38	31	30	34	33	32	27	38	32	45
Rb	1·4	0·19	0·13	0·23	<0·13	0·12	0·077	0·070	2·2	<0·013	0·36	0·19	0·017	<0·030	<0·068	<0·15	0·077	<0·15
Sr	373	237	120	128	123	122	130	255	341	131	116	119	139	385	130	331	176	421
Y	24	20	10	13	15	9·4	15	20	22	15	17	16	19	26	13	23	16	25
Zr	247	212	76	122	143	69	137	223	244	99	83	80	143	284	123	262	178	279
Nb	7·0	4·2	0·75	0·89	1·0	0·50	1·1	4·9	6·2	0·95	0·59	0·66	1·8	6·6	1·0	5·1	2·3	5·4
Cs	<0·016	<0·010	<0·017	<0·039	<0·085	<0·007	0·007	<0·010	<0·035	<0·005	<0·024	<0·033	<0·006	<0·011	<0·028	<0·084	<0·029	<0·058
Ba	1·6	1·0	0·38	0·46	<0·50	0·50	0·42	1·1	1·2	0·17	0·22	0·23	0·21	0·45	<0·240	<0·578	0·27	0·70
La	31	20	5·7	7·7	8·0	5·6	9·0	21	27	8·4	7·2	6·7	11	32	7·7	28	13	30

Ce	78	51	18	23	25	17	26	55	74	26	22	21	33	86	23	75	36	82
Pr	11	7·4	2·8	3·3	3·6	2·7	4·2	7·7	11	4·1	3·8	3·6	5·3	12	3·9	11	5·6	11
Nd	50	37	16	20	20	15	22	37	46	23	21	19	29	59	21	52	29	51
Sm	11	8·4	4·7	5·2	5·7	3·7	6·1	9·2	12	6·0	6·6	6·7	7·9	12	5·6	12	6·6	12
Eu	3·2	2·8	1·4	1·8	2·1	1·3	1·9	2·9	3·4	1·9	1·9	1·8	2·4	3·8	1·8	3·9	2·4	4·1
Gd	8·7	6·9	3·5	4·7	5·0	3·9	5·4	7·8	7·9	5·2	5·2	4·6	6·7	9·0	4·8	9·4	7·5	11
Tb	1·1	0·99	0·56	0·79	0·62	0·49	0·67	0·98	1·0	0·75	0·87	0·95	0·93	1·4	0·74	1·1	0·92	1·4
Dy	5·9	5·0	2·4	3·4	5·0	2·3	4·0	5·4	5·8	3·6	4·7	3·8	4·7	6·9	3·3	6·0	3·7	5·1
Ho	1·1	0·82	0·36	0·59	0·60	0·36	0·63	0·85	0·99	0·68	0·69	0·65	0·82	1·1	0·57	0·78	0·88	1·1
Er	2·1	1·9	0·87	1·4	1·0	0·92	1·4	1·6	2·2	1·4	1·7	1·3	1·8	2·3	1·4	1·8	1·4	2·2
Tm	0·29	0·22	0·11	0·11	0·19	0·10	0·16	0·25	0·29	0·17	0·16	0·12	0·19	0·22	0·11	0·30	0·19	0·40
Yb	1·6	1·4	0·64	1·2	0·67	0·52	1·1	1·2	1·6	1·1	1·2	0·83	1·2	1·8	1·2	1·0	1·3	2·1
Lu	0·20	0·18	0·084	0·17	0·17	0·071	0·13	0·17	0·20	0·094	0·13	0·085	0·17	0·18	0·14	0·22	0·16	0·15
Hf	6·6	7·0	3·2	6·0	6·6	3·3	6·3	6·9	7·0	4·4	3·5	3·1	6·7	8·9	5·4	7·7	8·1	8·2
Ta	1·2	0·80	0·090	0·17	0·17	0·09	0·22	0·90	0·94	0·22	0·13	0·082	0·42	1·3	0·14	1·1	0·30	1·6
Pb	0·29	0·064	<0·087	<0·13	<0·30	<0·097	<0·047	<0·11	0·31	0·12	0·16	0·15	0·16	0·18	<0·11	0·38	<0·13	<0·32
Th	0·72	0·51	0·059	0·13	0·16	0·07	0·19	0·61	0·60	0·11	0·16	0·10	0·17	0·55	0·13	0·55	0·31	0·50
U	0·13	0·061	<0·007	<0·014	<0·05	0·02	0·006	0·081	0·077	0·007	<0·013	<0·024	0·015	0·043	0·023	<0·039	0·035	<0·099
$(Ce/Yb)_n$	13·9	9·9	7·8	5·7	10·3	9·3	6·5	12·4	13·1	6·4	5·2	7·1	7·7	13·1	5·6	20·8	8·0	10·7
Zr/Nd	4·9	5·8	4·9	6·0	7·1	4·6	6·2	6·0	5·3	4·3	4·0	4·2	4·9	4·8	5·9	5·0	6·0	5·4
Ti/Eu	5951	5611	6179	6269	5749	6959	6322	5682	6090	6378	4559	5003	5918	5621	5734	5734	6139	5131
Zr/Hf	37·3	30·4	23·9	20·2	21·6	20·5	21·8	32·4	35·0	22·4	23·7	25·9	21·4	31·8	22·7	33·8	21·9	33·8
Nb/Ta	6·1	5·2	8·3	5·1	6·0	5·5	4·9	5·5	6·6	4·4	4·4	8·1	4·3	5·3	7·5	4·8	7·7	3·4

Oxides of selected major elements in wt %; trace elements in μg/g.

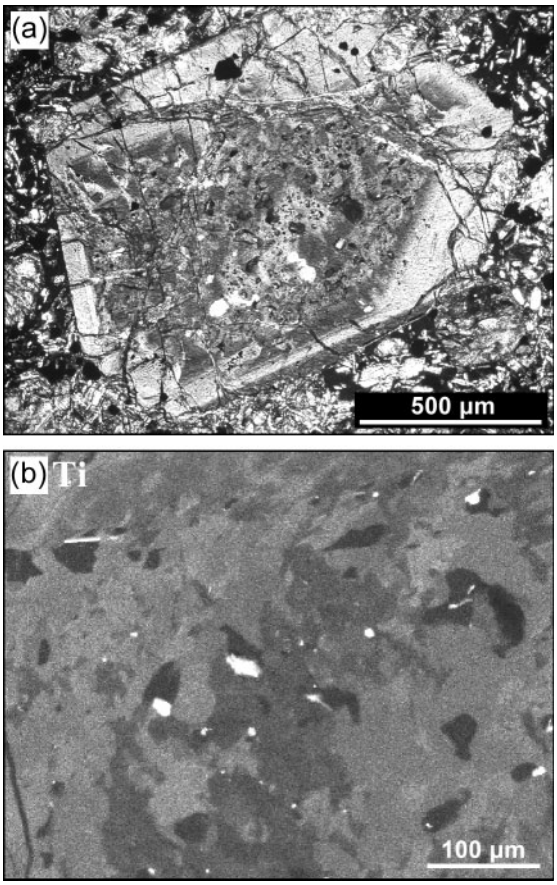

Fig. 3. Small clinopyroxene macrocryst exhibiting a well-developed domain texture over the entire core area. (a) Photomicrograph (cross-polarized light). (b) Element map obtained by energy-dispersive analysis and showing the distribution of Ti in a fragment of the core. Ti-rich inclusions (white) are late-stage Ti-rich magnetite crystals on the walls of opened fluid and melt-fluid inclusions.

olivine is common but mostly replaced by secondary minerals (Fig. 2d–f). Spinel may be present. The mantle hosts an entirely different set of inclusions (tiny needles of rutile, Ti-magnetite).

The core areas of Cpx II are Ca-rich, relatively magnesian, depleted in Na and characterized by low to moderate Al contents (Tables 5 and 6). Cpx II displays two modes in Cr content corresponding to high-Cr and low-Cr sub-types (Table 6). High-Cr Cpx II is typical of clinopyroxene–olivine aggregates (Figs 2b and 5a) and also occurs among the macrocrysts (Figs 2e and 5b). It displays a wide range of Ti contents (~0·1–1·2 wt %). Low-Cr Cpx II (Figs 2f and 5c) accounts for *c.* 60–70% of Cpx II macrocrysts, but is absent in clinopyroxene–olivine aggregates. This clinopyroxene is relatively rich in Ti (0·9–1·4 wt %). Between high- and low-Cr Cpx, transitional varieties occur (Table 6). The core areas of large Cpx II grains are more or less homogeneous in terms of chemical composition (Fig. 5a–c). Small grains show a significant scatter of chemical compositions in microprobe traverses, as a result of the development of the domain texture (Fig. 5f). Closer to the core–rim boundary, positive Cr anomalies and often some increase in Mg-number are observed, followed by strong chemical zoning towards the composition of matrix clinopyroxene within the rim zone. The Al and Ti contents increase, whereas the Mg-number decreases (Fig. 5a–c).

Cpx II are enriched in LREE (Table 7, Fig. 6c and e). Convex REE patterns are present (Fig. 6c and e). The multi-element patterns of the core parts of high-Cr Cpx II display variable negative anomalies of Zr, Hf and Ti (Fig. 6d). A considerable scatter in the trace element abundances over the whole set of the analysed grains of high-Cr Cpx II is observed (Fig. 6c and d). The core areas of low-Cr Cpx II show more uniform trace element patterns that are less depleted in Zr and Hf; the Ti depletion disappears (Fig. 6f).

Complementary to the major element zoning data, Cpx II show strong trace element zoning within the outer rim, resulting in enrichment in almost all incompatible trace elements rimwards (Table 7, Fig. 7a and b). Within the core, no significant variations between individual LA-ICPMS analyses are observed. In the intermediate zones in contact with the domain texture and corresponding to the Cr-peaks in the electron microprobe profiles (e.g. Fig. 5c), the trace element patterns are only marginally re-equilibrated, as shown by convex REE distributions and somewhat reduced Zr and Hf anomalies.

Cpx III represents early phenocrysts occasionally forming clots. Most of these phenocrysts consist of an euhedral core and a well-developed, broad mantle grading into the core with no sharp divide but, unlike the core, showing oscillatory zoning (Fig. 4a–d). Some phenocrysts do not have individualized core areas and show oscillatory zoning in the innermost part. No inclusions are observed either in the core or the mantle, except Ti-magnetite and tiny rutile needles within the outermost rim or along cracks. The outermost rim of Cpx III is indistinguishable from that of Cpx II.

The core areas of Cpx III are Ca-rich, relatively depleted in Na and characterized by low to moderate alumina contents (Table 8). They are depleted in Ti and often enriched in Cr compared with the intermediate and outer rims (Fig. 5d). The core areas of Cpx III display strong REE enrichment and uniform, well-defined convex REE patterns (Table 9, Fig. 6g). The multi-element patterns show a marked depletion in Sr that is not found in other clinopyroxene types. Weak negative Zr and positive Hf anomalies and the absence of any Ti anomaly are observed (Fig. 6h).

The core-to-rim trace element patterns of Cpx III phenocrysts and those of relatively large clinopyroxene

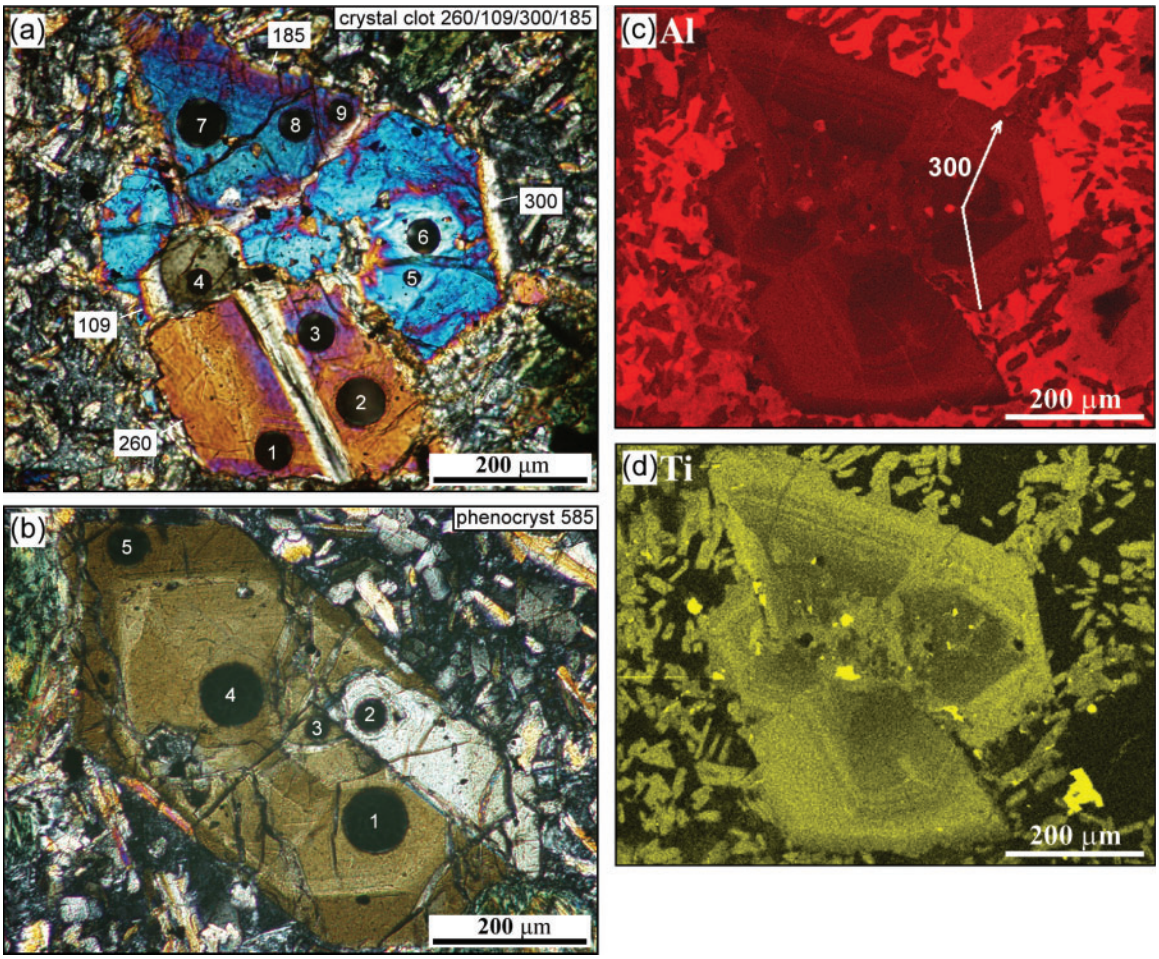

Fig. 4. Clinopyroxene phenocrysts (cross-polarized light). (a) Four individual phenocrysts forming a crystal clot. (b) Single phenocryst showing oscillatory zoning. Numbered spots correspond to laser ablation pits (see Table 9). (c, d) Element maps obtained by energy-dispersive analysis and showing the distribution of Al and Ti inside phenocrysts forming the crystal clot in (a). Oscillatory zoning in the distribution of Al and Ti is visible. Location of a microprobe profile in (c) is indicated by the white line with arrow (Fig. 5d, 300 μm profile).

microphenocrysts (~30 μm × 80 μm) from the rock matrix are shown in Fig. 7c and d. The phenocrysts exhibit enrichment in almost all incompatible elements rimwards. The microphenocrysts display a large scatter in trace element abundances, encompassing compositions typical of core areas of large phenocrysts as well as those characteristic of the rim zones of all clinopyroxenes.

Geochemical relationships between different clinopyroxene types

In the following discussion, all clinopyroxenes are considered in the context of the chemical composition of their core areas. Their averaged major element compositions are plotted in Fig. 8. Relict Cpx I form a distinct group. They could be compared with clinopyroxene from depleted mantle rocks. Cpx I grain 997/274 with ~1·5 wt % Cr_2O_3 is one of the most Cr-rich clinopyroxenes ever found in mantle xenoliths and macrocrysts from the Kaiserstuhl (see Keller, 1977, 1984; Keller *et al.*, 1990; Sigmund, 1996). In terms of major elements, Na and Ca in particular, there is no continuum between such relicts and Cpx II (Figs 5a and 7). Between high- and low-Cr Cpx II and Cpx III, the transition in major elements except for Cr is gradual (Fig. 8, Tables 6 and 8). The Cr contents decrease rather sharply from high- to low-Cr Cpx II, and then increase again in the core parts of early Cpx III phenocrysts (Fig. 8, Tables 6 and 8).

In terms of most trace elements, the transition between the clinopyroxene types is gradual. Trace element patterns of the core areas of high-Cr Cpx II retain many features typical of relict Cpx I. For instance, relict clinopyroxene 997/274 is partially replaced by high-Cr clinopyroxene 997, with a sharp boundary between them being observed both optically (Fig. 2b) and in the electron microprobe profiles (Fig. 5a). Their trace element patterns are similar (compare patterns 997/274 and 997 in Fig. 6a–d).

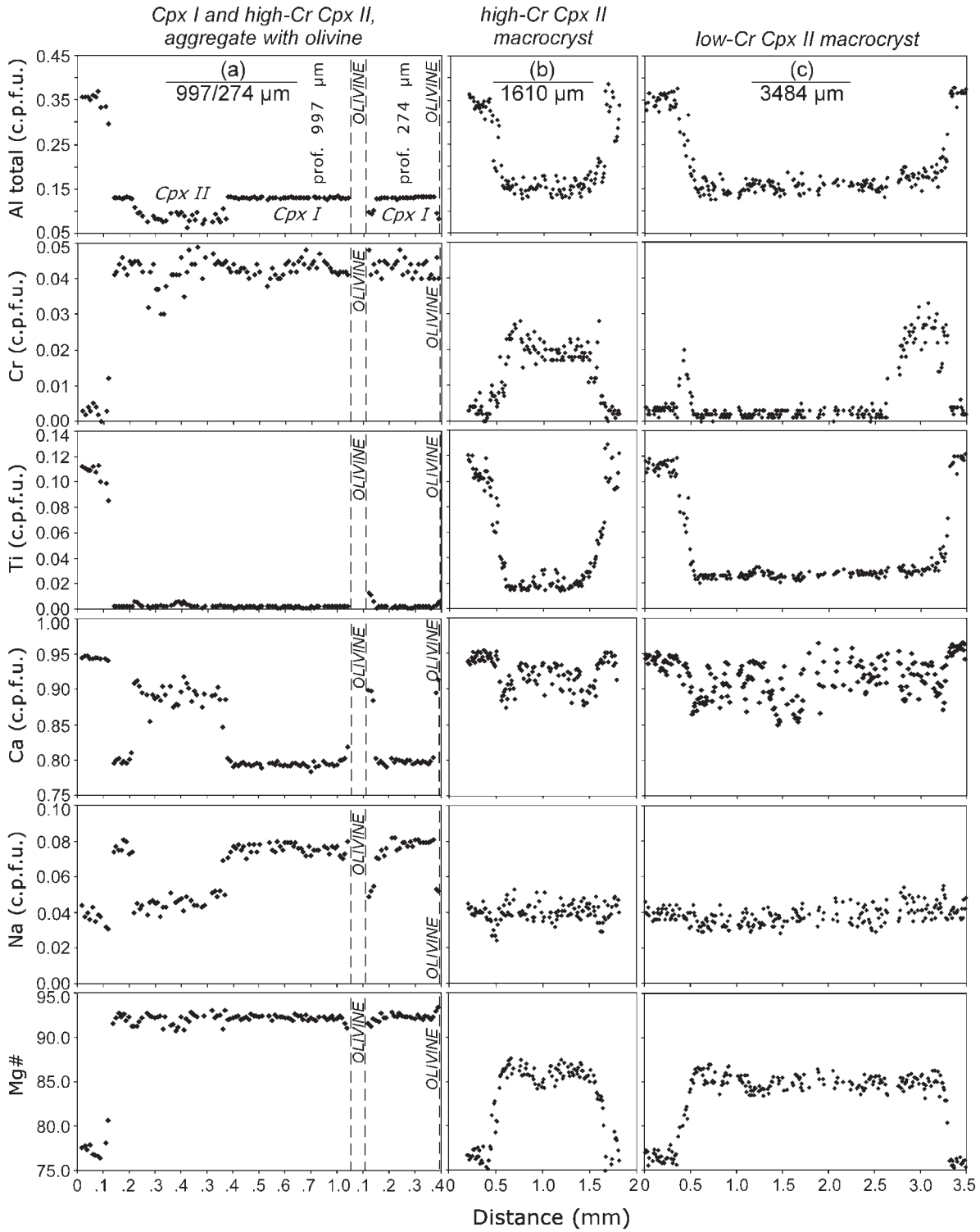

Fig. 5. Microprobe profiles illustrating the zoning patterns of clinopyroxenes. (a) Relict Cpx I partly replaced by high-Cr Cpx II in clinopyroxene–olivine aggregate 997/274. (b) High-Cr Cpx II, macrocryst 1610. (c) Low-Cr Cpx II, macrocryst 3484. (d, e) Cpx III, phenocrysts 300 and 585. (f) Relatively small clinopyroxene macrocryst (1317) with a well-developed domain texture. Clinopyroxene grain numbers correspond to the length of the electron microprobe profiles carried out for each of the grains.

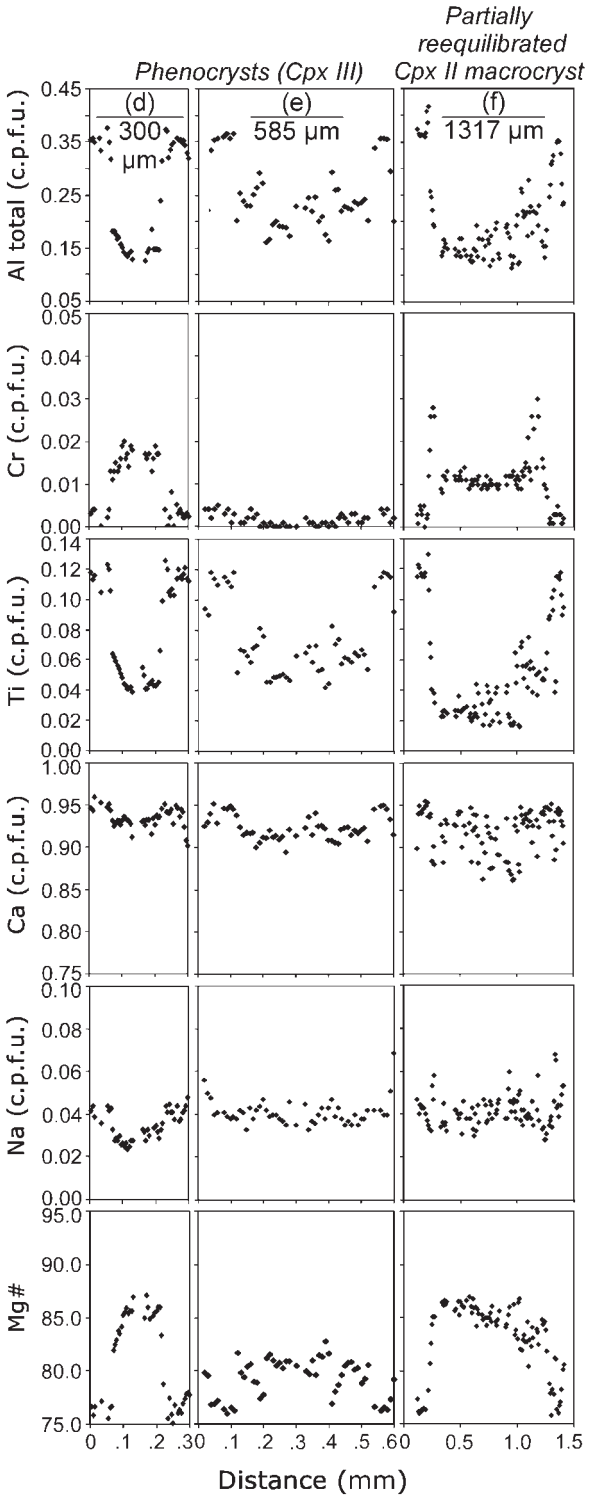

Fig. 5. Continued

However, in general, the 'straight-line' REE patterns of Cpx I grade into the convex patterns in Cpx II (Fig. 6c). The negative anomalies of Zr and Hf are less pronounced than in Cpx I, and the negative anomaly of Ti in many cases disappears (Fig. 6d). The core areas of low-Cr Cpx II display trace element patterns that are intermediate between those of high-Cr Cpx II and Cpx III phenocrysts. The REE elements are strongly fractionated and sometimes show convex patterns (Fig. 6e). The negative Zr and Hf anomalies are less expressed than in high-Cr Cpx II (Fig. 6f). The Ti depletion disappears (Fig. 6f). Cpx III is characterized by well-defined convex REE patterns (Fig. 6g). Compared with Cpx II, the middle REE (MREE) to HREE, Y, Zr, Hf and Ti are enriched (Fig. 6h). The only discontinuity between the trace element compositions of different clinopyroxene types is the depletion of Cpx III in Sr (Fig. 6h).

All clinopyroxenes exhibit strong negative Rb, K and Ba anomalies that are consistent with the incompatibility of these large cations in the clinopyroxene lattice. The negative anomalies of Rb and K are matched in the multi-element pattern of the host olivine nephelinite (Fig. 6).

Inclusions in clinopyroxene

The core areas of Cpx II contain frequent solid, melt and fluid inclusions (Fig. 2b, d–f). The solid inclusions are represented by olivine, carbonate minerals, spinel, apatite and graphite (Fig. 9a–h). Olivine and particularly carbonate minerals are common. Apatite and graphite are rare; they occur in some multi-phase melt–fluid inclusions. The melt inclusions are represented by quenched carbonatite melt and alkali aluminosilicate glass.

Olivine forms anhedral to subhedral inclusions ranging from ~20 to 150 μm in size. They are often associated with calcite and, in the case of smaller inclusions, with alkali aluminosilicate glass and fluid (Fig. 9b and c). Large olivine inclusions are replaced by saponite, serpentine and calcite, whereas small ones (<30 μm) can often be found unaltered. The chemical composition of such inclusions approaches that of the core areas of large olivine macrocrysts.

Carbonate minerals are represented by calcite and Sr-aragonite forming small (normally <35–40, rarely up to 120 μm) drop-like inclusions in the core parts of clinopyroxene macrocrysts (Fig. 9a). Less typically, they occur as thin veinlets in the latter. Calcite may also be present in complex multi-phase inclusions where it is associated with alkali aluminosilicate glass and/or olivine (Fig. 9c and d). Two types of calcite can be distinguished. More commonly, pure calcite forms drop-like inclusions and, less frequently, veinlets. Mg–Mn-rich calcite occurs only in small (<20–35 μm) isolated inclusions. Sr-aragonite forms individual inclusions, thin veinlets and incrustations along cracks. Larger inclusions of Sr-aragonite are often inhomogeneous, made of domains with variable Sr contents. The major and trace element compositions of calcite and Sr-aragonite are given in Table 11. Pure and Mg–Mn-rich calcite are depleted in Sr (SrO <0·5 wt %), whereas

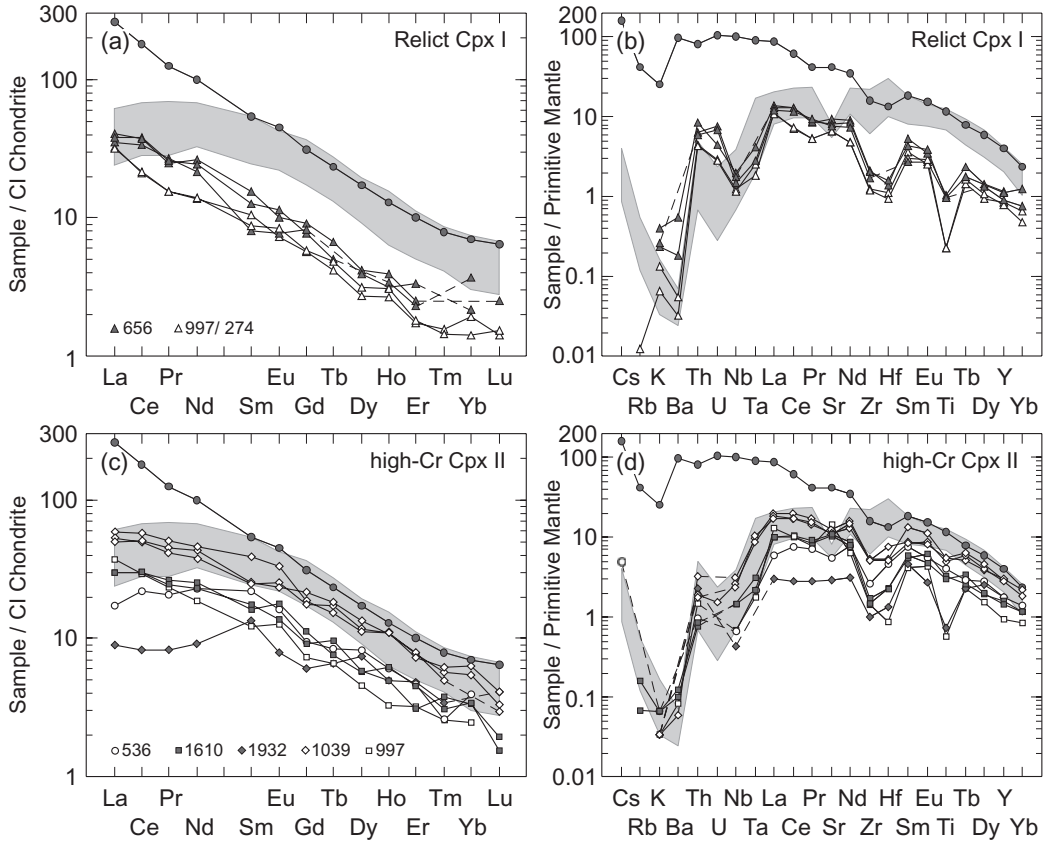

Fig. 6. Normalized REE and multi-element patterns of clinopyroxenes (core areas): (a, b) relict Cpx I; (c, d) high-Cr Cpx II; (e, f) low-Cr Cpx II; (g, h) Cpx III phenocrysts. Normalization values are from Sun & McDonough (1989).

Sr-aragonite is characterized by very low contents of Mn, Fe and Mg (Table 10). The chemical composition of the Mg–Mn-rich calcite inclusions is highly variable in both single macrocrysts and over the whole set of the studied macrocrysts. Both very high (~9·0 wt %) and relatively low (~1·45 wt %) MgO contents are observed in nearby inclusions. Both types of calcite, as well as Sr-aragonite, have very low abundances of REE and high field strength elements (HFSE). Normally, the total REE abundance does not exceed 2–3 μg/g (Table 11). Only in heterogeneous inclusions where calcite is in contact with secondary phyllosilicates replacing olivine, may the ∑REE reach 10–11 μg/g.

Spinel forms tiny (<7–8 μm) euhedral and subhedral inclusions in both high- and low-Cr Cpx II. The inclusions are commonly associated with alkali aluminosilicate melt, although individual inclusions are also present (Fig. 9b). Spinel inclusions are much more common in high-Cr Cpx II than in low-Cr Cpx II. The composition of the inclusions ranges from Cr–Al-rich spinel (picotite) in high-Cr Cpx II to very aluminous low-Cr spinel (hercynite) in low-Cr Cpx II (Table 11).

Inclusions (up to 20–30 μm in size) of quenched carbonatite melts rarely occur in the studied clinopyroxenes. In the core parts of two Cpx II macrocrysts, we found seven unaltered inclusions that can be referred to as quenched carbonatite melt based on their texture (Fig. 9e and f) and major element composition (Fig. 10; Table 11). Their chemical compositions correspond to silicic, calcic carbonatite melts with relatively low abundances of MgO and FeO and alkalis (Table 11). Some inclusions show significant inhomogeneity as a result of the segregation of silicate and carbonate phases in the quenched aggregate (Fig. 9f; to a lesser degree, present in Fig. 9e).

Irregular or rounded inclusions of alkali aluminosilicate glass mostly do not exceed 20 μm in size (Fig. 9a–d and f–h). When imaged using a scanning electron microscope (magnification × 2500–3000), small inclusions appear homogeneous. Larger inclusions (20–25 μm) often contain microcrystals of nepheline. Two glass types can be distinguished. Glass I was detected in three inclusions, two of them also containing quenched carbonatite melt and crystalline calcite (Fig. 9f). It is tephriphonolitic in composition (Table 11; also see Fig. 10). Glass II is far more common. It often occurs in heterogeneous, often fluid-bearing, inclusions that do not contain quenched carbonatite melt (Fig. 9a–d, g and h). Large variations in the modal proportion of melt in the fluid-bearing inclusions

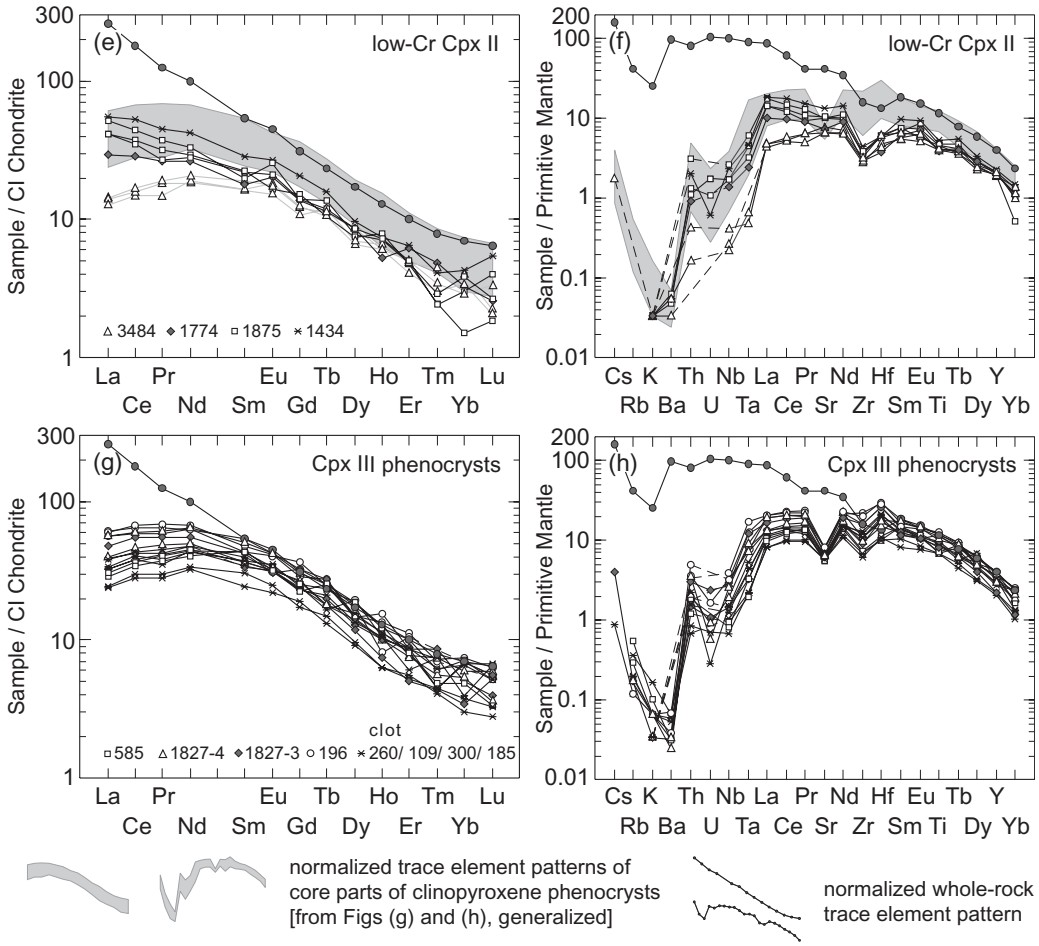

Fig. 6. Continued.

suggest that both fluid and melt represent individual phases during the entrapment of the inclusions; that is, the entrapment was heterogeneous. Glass II is often associated with Mg–Mn-rich calcite and Mg-rich olivine (Fig. 9c and d). Rarely, Cr–Al-spinel and apatite are present. Secondary phases observed in some inclusions are Ti-phlogopite and Ti-magnetite; the former typically develops at the border between the glass and the fluid, whereas the latter forms crystal precipitates on the walls of the fluid cavities. Primary phlogopite and amphibole are absent. In terms of major elements, glass II closely matches the theoretical composition of persilicic nepheline (A. Ulianov *et al.*, unpublished data). Its chemical composition is characterized by a low Fe content and extreme depletion in Ti, Mg and, in most cases, Ca (Fig. 10; Table 11). These features might reflect the nepheline-like structure of the corresponding melt, which is poorly compatible with such cations (e.g. Simakin *et al.*, 2005). Glass II is rich in incompatible elements (Sr, Cs, Rb, Nb, Ta, Zr, LREE; A. Ulianov *et al.*, unpublished data).

Glass II chemical compositions appear primary. Except for the presence of nepheline microcrystals in large inclusions, no convincing evidence for post-entrapment chemical modification of the glass was found. Detailed element maps show that the clinopyroxene host in contact with the glass does not change its chemical composition, whereas olivine crystals associated with the glass in multi-phase inclusions are highly magnesian.

Fluid inclusions up to 30–35 μm in size are common. They are rounded or, less frequently, show negative crystal shapes. Microscopically, three phases can be distinguished in the inclusions: a gas, a liquid, and an oxide phase with high reflection index. The last is a Ti-rich magnetite, clearly visualized by SEM (Fig. 9g). The study of opened inclusions by SEM has also revealed a close association of the fluid with glass II, with more than half of all inclusions either showing a contact of the fluid cavity with 'massive' glass or containing thin glass coatings on the walls (Fig. 9g and h). Several inclusions contain apatite. One (possibly two) inclusions contain graphite (Fig. 9h).

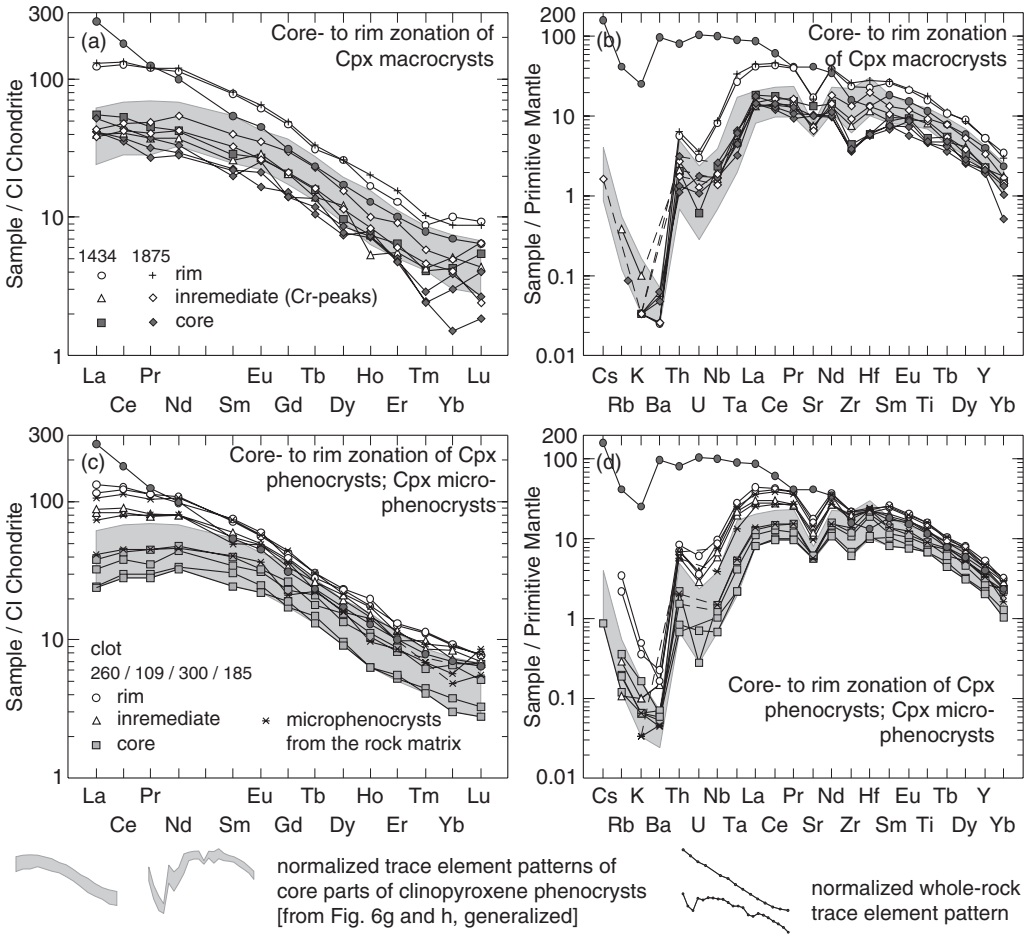

Fig. 7. Normalized REE and multi-element patterns of clinopyroxene (core-to-rim zoning and microphenocrysts): (a, b) core-to-rim zoning of clinopyroxene macrocrysts; (c, d) core-to-rim zoning of clinopyroxene phenocrysts and composition of clinopyroxene microphenocrysts from the olivine nephelinite matrix. Normalization values as in Fig. 6.

DISCUSSION

The relationship between macrocrysts and the host magma

One of the prime aims of this study is to show that the studied suite of macrocrysts and mineral aggregates represents fragments of the mantle source region entrained by the host magma during its formation. Comparing the major and trace element compositions of the clinopyroxene macrocrysts with those of the 'true' phenocrysts of clinopyroxene (with oscillatory zoning) seems to be the best way to evaluate whether or not the macrocrysts are related to the host magma. Other options include comparing the trace element characteristics of the macrocrysts with those of the host rock, provided that mineral–melt partition coefficients are well known, or showing that the macrocrysts are in isotopic equilibrium with the host rock. The first option implies that no immiscible liquids or fluids separated from the host magma *en route* to the surface, and both require the host rock to be fresh. The second option also faces difficulties because of possible isotope re-equilibration between the host magma and the macrocrysts.

In general, the major element data show a gradual transition from Cpx II to Cpx III, and the trace element data demonstrate a gradual transition between all Cpx types. Evolutionary changes include systematic enrichment in Ti, Zr and Hf from Cpx I to high- and low-Cr Cpx II and further to Cpx III, accompanied by some depletion in La and Ce resulting in convex REE patterns. The gradual transition in the chemical composition from Cpx II to Cpx III could be consistent with the derivation of Cpx II from the source region of the olivine nephelinite magma that precipitated early phenocrysts of Cpx III.

Formation of the source region: metasomatism and relationship with carbonatite magmatism

Metasomatism: geochemical characteristics of relict Cpx I

It has been widely proposed that mantle metasomatism can be a precursor to alkaline magmatism

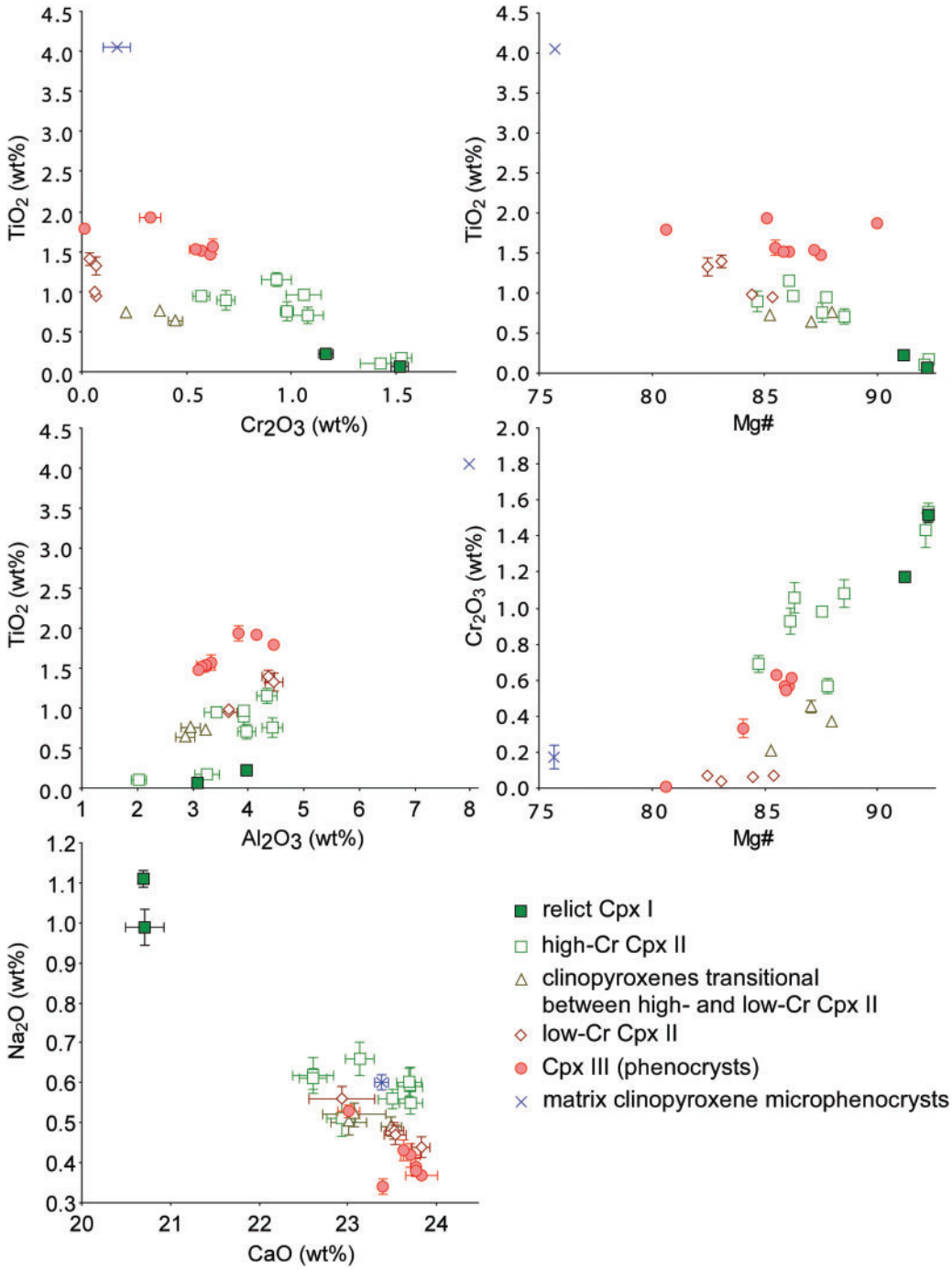

Fig. 8. Binary diagrams illustrating the major element variations in clinopyroxene. A gradual transition between high-Cr Cpx II, low-Cr Cpx II and Cpx III is observed. Error bars correspond to 1σ; if not shown, they are smaller than symbol size.

(e.g. Norry *et al.*, 1980; Wass & Rogers, 1980; Lloyd, 1981; Ionov *et al.*, 1994; Furman, 1995; Späth *et al.*, 2001; Dawson, 2002). The studied Cpx macrocrysts and Ol–Cpx aggregates do not represent fragments derived from 'pristine' (i.e. non-metasomatized) mantle rocks. Cpx I is characterized by marked LREE enrichment (12–14 times chondrite), negative anomalies of Zr, Hf and Ti and low Ti/Eu ratios (Fig. 11a and b; Table 7). These features are typical of clinopyroxene inferred to be formed by carbonatite metasomatism of the mantle, as shown by both natural mineral assemblages from xenoliths (e.g. Hauri *et al.*, 1993; Norman, 1998; Powell *et al.*, 2004) and experiments in carbonatite systems (e.g. Klemme *et al.*, 1995; Blundy & Dalton, 2000; Adam & Green, 2001). They are also

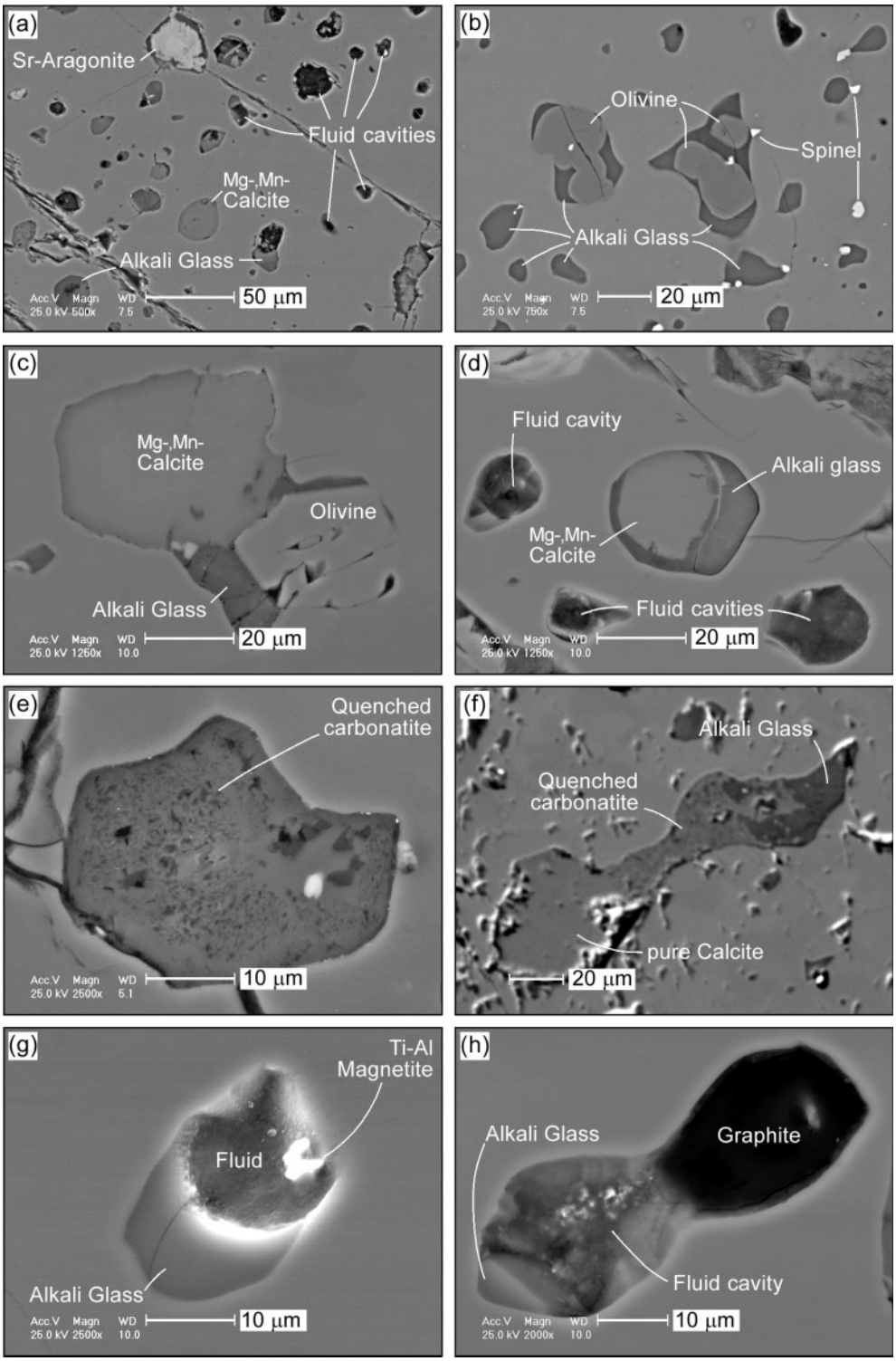

Fig. 9. Backscattered (a–f, h) and secondary (g) electron images of inclusions in the core areas of clinopyroxene grains. (a) Calcite, Sr-aragonite, glass and fluid inclusions, macrocryst 3484. (b) Olivine, Cr–Al-spinel and alkali aluminosilicate glass II, macrocryst 1932. (c) Multi-phase inclusion of Mg–Mn-calcite, olivine and alkali aluminosilicate glass II, macrocryst 1774. (d) Multi-phase inclusion of Mg–Mn-calcite and alkali aluminosilicate glass II, macrocryst 3484. (e) Inclusion of quenched carbonatite melt, macrocryst 2308. (f) Multi-phase inclusion containing calcite, quenched carbonatite melt and alkali silicate glass I, macrocryst 1827w. (g) Opened fluid–melt inclusion with Ti–Al-rich magnetite on the wall containing alkali aluminosilicate glass II, macrocryst 3484. (h) Opened fluid–melt inclusion with graphite and alkali aluminosilicate glass II, macrocryst 3484.

Table 10: Representative trace element analyses of clinopyroxene microphenocrysts from the rock matrix

	1	2	3
TiO_2	1·954	2·964	3·544
MnO	0·081	0·090	0·080
K_2O	0·001	0·001	0·002
P_2O_5	0·028	0·071	0·022
Li	2·8	3·0	4·2
B	4·5	<12	6·3
Sc	161	77	56
V	147	233	280
Cr	2515	911	904
Co	29	33	28
Ni	146	191	155
Zn	27	33	35
Rb	<0·049	<0·078	<0·061
Sr	123	206	305
Y	16	16	22
Zr	158	202	249
Nb	1·1	2·8	5·5
Cs	<0·025	<0·064	<0·033
Ba	0·32	<0·66	0·32
La	9·7	17	25
Ce	27	49	69
Pr	4·3	7·5	9·9
Nd	21	37	49
Sm	6·3	7·6	11
Eu	2·1	2·8	3·3
Gd	4·3	7·5	9·0
Tb	0·83	0·86	1·1
Dy	4·1	4·0	5·5
Ho	0·55	0·81	0·97
Er	1·4	1·6	1·8
Tm	0·17	0·27	0·24
Yb	0·97	0·82	1·5
Lu	0·22	0·14	0·20
Hf	7·5	7·0	7·6
Ta	0·23	0·55	1·0
Pb	<0·15	<0·31	<0·12
Th	0·17	0·50	0·58
U	<0·028	<0·073	<0·032
$(Ce/Yb)_n$	7·8	16·5	12·7
Zr/Nd	7·5	5·4	5·1
Ti/Eu	21·2	28·7	32·9
Zr/Hf	21·2	5·1	5·4
Nb/Ta	4·6	5·1	5·4

Oxides of selected major elements in wt %; trace elements in μg/g.

consistent with the general bulk-rock geochemical characteristics of the metasomatized xenoliths (Yaxley *et al.*, 1991, 1998; Ionov *et al.*, 1993; Rudnick *et al.*, 1993; Powell *et al.*, 2004), and of many carbonatites (e.g. Nelson *et al.*, 1988; Woolley & Kempe, 1989). Moreover, the occurrence of carbonatite melt inclusions found in Cpx II macrocrysts testifies to the presence of a carbonatitic component.

Phase relations in the system peridotite–CO_2

Chemical reactions relevant to the process of carbonatite metasomatism in the mantle were investigated experimentally in the model system CaO–MgO–SiO_2–CO_2 (CMS–CO_2; see Eggler, 1974, 1976, 1978; Wyllie & Huang, 1976; Brey *et al.*, 1983; White & Wyllie, 1992; Lee & Wyllie, 2000; Lee *et al.*, 2000) and in natural peridotite compositions (e.g. Olafsson & Eggler, 1983; Wallace & Green, 1988; Falloon & Green, 1989; Dalton & Wood, 1993; Yaxley & Green, 1998). Two subsolidus reactions for carbonate–lherzolite and five solidus curves for lherzolite, wehrlite, harzburgite and websterite plus CO_2–carbonate in the system peridotite–CO_2 are shown in Fig. 12a. The reaction $Opx + Dol = Cpx + Ol + CO_2$ corresponds to the dissociation of dolomite–lherzolite. With increasing temperature, this assemblage is joined by melt, generating a six-phase invariant point Q (*c.* 20–22 kbar/1050–1090°C in natural systems). At pressures exceeding Q, three high-pressure solidus reactions for dolomite–harzburgite, dolomite–websterite and dolomite–lherzolite emanate from the invariant point. Along the solidus and slightly above, these reactions produce magnesian carbonate melts (e.g. Wallace & Green, 1988; Gudfinnson & Presnall, 2005). Such melts are highly mobile and able to ascend rapidly from their source regions (Hunter & MacKenzie, 1989; Watson *et al.*, 1990; Dobson *et al.*, 1996). At pressures lower than Q, two additional solidus reactions for lherzolite–CO_2 (1) and carbonate-wehrlite (2) exist. Just above Q, the lherzolite–CO_2 solidus curve corresponding to reaction (1) bends sharply through a large temperature interval (Fig. 12a).

The bend (or ledge) of the solidus of lherzolite–CO_2 above Q has been widely discussed in the context of both carbonatite petrogenesis and mantle metasomatism. In most tectonic settings, a carbonatite melt rising towards the surface from the pressure interval below Q encounters the solidus ledge and reacts with lherzolite to form wehrlite and exsolve CO_2, the residual carbonatite melt becoming more calcic:

$$5MgSiO_3 + 2CaMg(CO_3)_2 = 3Mg_2SiO_4 + CaMgSi_2O_6 + CaCO_3 + 3CO_2$$

$$Opx + Mg\text{–rich carbonatite melt} = Ol + Cpx + Ca\text{–rich carbonatite melt} + fluid.$$

Table 11: Representative microprobe analyses of inclusions in clinopyroxene II

	Spinel							Carbonates					
	in high-Cr Cpx				in low-Cr Cpx			3484				1774	1875
	1932	1932	1932	1610	3484	3484		Mg-Mn-calcite	Mg-Mn-calcite	Pure calcite	Sr-aragonite	Mg-Mn-calcite	Mg-Mn-calcite
SiO_2	0·14	0·11	0·23	0·18	0·17	0·27							
TiO_2	0·33	0·23	0·21	0·84	0·59	1·43	*EMPA*						
Al_2O_3	29·21	34·59	42·58	47·19	55·81	53·53	CaO	38·34	52·83	56·24	45·91	50·35	53·19
Cr_2O_3	35·08	30·67	23·69	6·44	1·40	1·02	FeO	0·88	0·26	0·05	0·11	0·56	0·23
Fe_2O_3	4·07	3·23	3·22	10·47	8·05	9·11	MnO	5·14	1·63	n.d.	0·04	2·80	1·03
FeO	16·58	16·03	13·13	19·96	20·52	17·71	MgO	9·01	1·45	n.d.	n.d.	3·06	1·03
MnO	0·22	0·22	0·20	0·38	0·31	0·17	SrO	0·30	0·04	0·12	11·52	0·10	0·32
NiO	0·10	0·15	0·17	0·23	0·31	0·28	BaO	0·02	0·06	n.d.	n.d.	n.d.	0·02
ZnO	0·14	0·10	n.d.	0·16	n.d.	0·17	Na_2O	0·03	n.d.	n.d.	0·04	0·02	0·03
MgO	12·85	13·64	16·80	12·46	13·33	15·24	SiO_2	0·05	0·07	0·04	n.d.	0·02	0·09
CaO*	0·46	0·41	0·43	0·46	0·25	0·34	Total	53·76	56·33	56·45	57·62	56·91	55·94
Na_2O	n.d.	0·02	0·02	n.d.	0·02	n.d.							
Total	99·18	99·40	100·68	98·77	100·76	99·27	Ca	0·686	0·935	0·997	0·878	0·878	0·950
							Fe^{2+}	0·012	0·004	0·001	0·002	0·008	0·003
Si	0·004	0·003	0·006	0·005	0·005	0·007	Mn	0·073	0·023	0·000	0·001	0·039	0·015
Ti	0·008	0·005	0·004	0·018	0·012	0·029	Mg	0·224	0·036	0·000	0·000	0·074	0·026
Al	1·043	1·200	1·393	1·585	1·775	1·719	Sr	0·003	0·000	0·001	0·119	0·001	0·003
Cr	0·841	0·714	0·520	0·145	0·030	0·022	Ba	0·000	0·000	0·000	0·000	0·000	0·000
Fe^{3+}	0·093	0·071	0·067	0·225	0·163	0·187	Na	0·001	0·000	0·000	0·001	0·001	0·001
Fe^{2+}	0·420	0·395	0·305	0·476	0·463	0·403	Si	0·001	0·001	0·001	0·000	0·000	0·002
Mn	0·006	0·005	0·005	0·009	0·007	0·004	Sum	1·000	0·999	1·000	1·001	1·001	1·000
Ni	0·002	0·004	0·004	0·005	0·007	0·006	Ca/∑cat	0·69	0·94	1·00	0·88	0·88	0·95
Zn	0·003	0·002	0·000	0·003	0·000	0·003							
Mg	0·580	0·599	0·695	0·529	0·536	0·619	*LA-ICPMS (TiO_2, K_2O and P_2O_5 in wt %; elements in μg/g)*						
Na	0·000	0·001	0·001	0·000	0·001	0·000	TiO_2	<0·001	n.a.	0·002	0·001	0·003	n.a.
Sum	3·000	3·000	3·000	3·000	3·000	3·000	K_2O	0·002	n.a.	0·001	0·003	<0·001	n.a.
Mg-no.	58·0	60·3	69·5	52·6	53·7	60·6	P_2O_5	<0·008	n.a.	0·008	0·016	<0·008	n.a.
							Sc	0·53	n.a.	0·31	<0·34	<0·46	n.a.
	Quenched carbonatite melt						Zn	8·1	n.a.	2·1	<1·4	<1·5	n.a.
	6/1109	1	2 spots in one incl.		2/6		Rb	0·17	n.a.	0·057	0·34	<0·23	n.a.
SiO_2	7·97	11·50	11·73	20·42	15·39		Sr	2187	n.a.	1075	87856	522	n.a.
TiO_2	0·04	0·05	0·13	0·08	0·03		Y	0·43	n.a.	0·21	0·15	0·19	n.a.
Al_2O_3	4·21	5·73	5·74	8·09	6·08		Zr	<0·20	n.a.	0·098	<0·084	0·28	n.a.
Cr_2O_3	n.d.	n.d.	n.d.	0·01	0·04		Nb	<0·14	n.a.	0·069	<0·074	0·73	n.a.
FeO	0·64	1·07	1·28	1·48	0·66		Ba	6·2	n.a.	0·16	15	<0·96	n.a.
MnO	0·23	0·04	0·14	0·08	0·02		La	0·16	n.a.	0·14	0·37	0·17	n.a.
MgO	1·03	0·24	3·49	6·95	0·85		Ce	0·53	n.a.	0·34	0·39	0·43	n.a.
CaO	46·51	43·47	35·21	27·70	38·67		Nd	0·64	n.a.	0·20	<0·32	<0·46	n.a.
Na_2O	1·46	1·60	1·73	1·56	3·01		Sm	<0·57	n.a.	0·14	<0·19	<0·66	n.a.
K_2O	0·48	0·55	0·58	1·88	0·88		Eu	<0·079	n.a.	0·043	<0·082	<0·16	n.a.
SrO	0·24	0·09	0·22	n.d.	0·19		Dy	<0·17	n.a.	<0·036	0·14	0·19	n.a.
BaO	n.d.	n.d.	n.d.	0·02	n.d.		Ho	<0·076	n.a.	0·012	0·035	<0·10	n.a.
P_2O_5	0·49	0·45	0·44	0·41	0·47		Yb	<0·60	n.a.	<0·030	0·22	<0·49	n.a.
Total	63·30	64·78	60·68	68·68	66·29		Th	<0·050	n.a.	0·052	0·81	<0·056	n.a.
							U	<0·050	n.a.	0·061	0·085	<0·078	n.a.

Table 11: Continued

	Alkali aluminosilicate glass											
	glass I		glass II									
	2/2	2/10	16	1	21	9	1a	7	3	1	8	14
SiO_2	48·06	49·41	52·02	53·35	53·62	53·74	53·92	53·94	54·05	54·05	54·19	55·05
TiO_2	0·03	0·04	0·06	0·14	0·15	0·07	0·12	0·11	0·13	0·10	0·05	0·11
Al_2O_3	22·03	20·93	25·64	24·68	24·84	25·85	25·33	24·81	24·79	25·76	25·65	25·42
Cr_2O_3	n.d.	n.d.	n.d.	0·06	n.d.	0·01	0·01	0·03	n.d.	n.d.	0·02	n.d.
Fe_2O_3	1·92	3·96	1·34	0·72	0·55	0·50	1·06	0·82	0·95	0·99	0·55	0·38
MnO	n.d.	0·15	0·02	0·05	0·04	0·01	n.d.	0·04	n.d.	n.d.	0·01	0·02
MgO	5·99	4·72	0·06	0·03	0·08	n.d.	0·05	0·06	0·06	0·11	0·05	0·01
CaO	4·48	0·88	0·67	0·21	0·29	0·21	0·25	0·20	0·21	0·26	0·23	0·25
Na_2O	2·51	4·47	9·54	7·56	7·65	10·77	10·18	8·60	8·90	12·65	10·33	10·40
K_2O	5·72	4·90	9·74	12·67	12·49	8·15	8·82	11·12	10·62	5·64	8·21	8·21
Total†	90·74	89·46	99·09	99·48	99·71	99·32	99·75	99·73	99·88	99·56	99·28	99·86

Oxides in wt %; trace elements in μg/g; n.d., not detected. For spinel, Fe_2O_3 and FeO were calculated assuming ideal stoichiometry. For carbonates and quenched carbonatite melt, total Fe is given as FeO. For alkali aluminosilicate glass, total Fe is given as Fe_2O_3. Mg-number $= 100 \times Mg/(Mg + Fe^{2+})$.
*Ca was excluded from stoichiometric calculations, as its content is defined by secondary X-ray emission from the host Cpx.
†Glasses I and II may contain up to 0·5 wt % BaO, 0·8 wt % P_2O_5 and 0·4 wt % Cl.

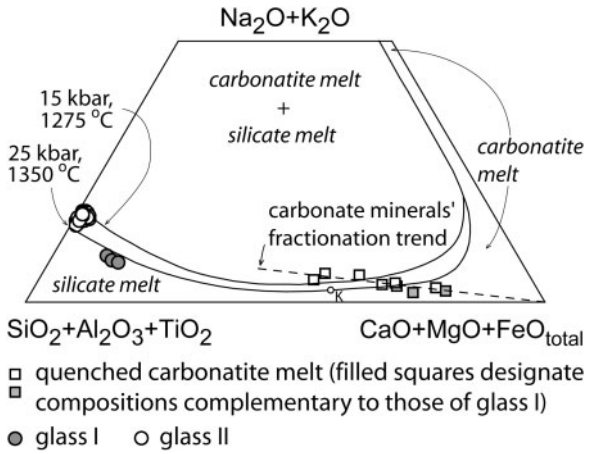

Fig. 10. Major element compositions of quenched carbonatite melt, glass I and glass II in the Hamilton projection (Freestone & Hamilton, 1980; Kjarsgaard & Hamilton, 1989). The geometry of the miscibility gap is controlled by temperature, pressure and bulk chemical composition (for review, see Lee & Wyllie, 1997, 1998; Brooker, 1998). The miscibility gap boundaries for 15 and 25 kbar are from Brooker (1998) and Lee & Wyllie (1996), respectively.

This reaction corresponds to reaction (1) in Fig. 12a. It hinders the ascent of primary mantle carbonatite melts to the surface, because they are 'absorbed' by refractory lherzolite or harzburgite lithologies on the solidus ledge (Green & Wallace, 1988). If the carbonatite melt does not crystallize, the resulting wehrlitic assemblage can be preserved. Precipitation of carbonate minerals from the carbonatite melt causes incongruent melting of the wehrlite, dissolution of olivine and crystallization of clinopyroxene:

$$2Mg_2SiO_4 + 4CaCO_3 + 2CO_2 = CaMgSi_2O_6 + 3CaMg(CO_3)_2$$

$$\mathrm{Ol} + \frac{\mathrm{Cc}}{\mathrm{Dol}} + \mathrm{fluid} = \mathrm{Cpx} + \mathrm{carbonatite\ melt}.$$

This reaction, corresponding to reaction (2) in Fig. 12a, is unfortunately not yet sufficiently well studied (for review, see Lee & Wyllie, 1997, 1998, 2000). For a Mg-rich carbonate mineral phase, it might possibly be congruent.

Precipitating carbonates from a carbonatite melt after completion of reaction (1) is possible if the crystallization process takes place under disequilibrium conditions and occurs very rapidly. The univariant five-phase assemblage $Fo + Di + Cc/Dol + CO_2 +$ carbonatite melt in the CMS–CO_2 system is stable only along the wehrlite solidus [reaction (2)], whereas the four-phase field separating reaction curves (1) and (2) does not contain crystalline carbonates. At slow reaction rates, the highly mobile carbonatite liquid may escape the system or be consumed by reaction with adjacent orthopyroxene-bearing mantle rocks.

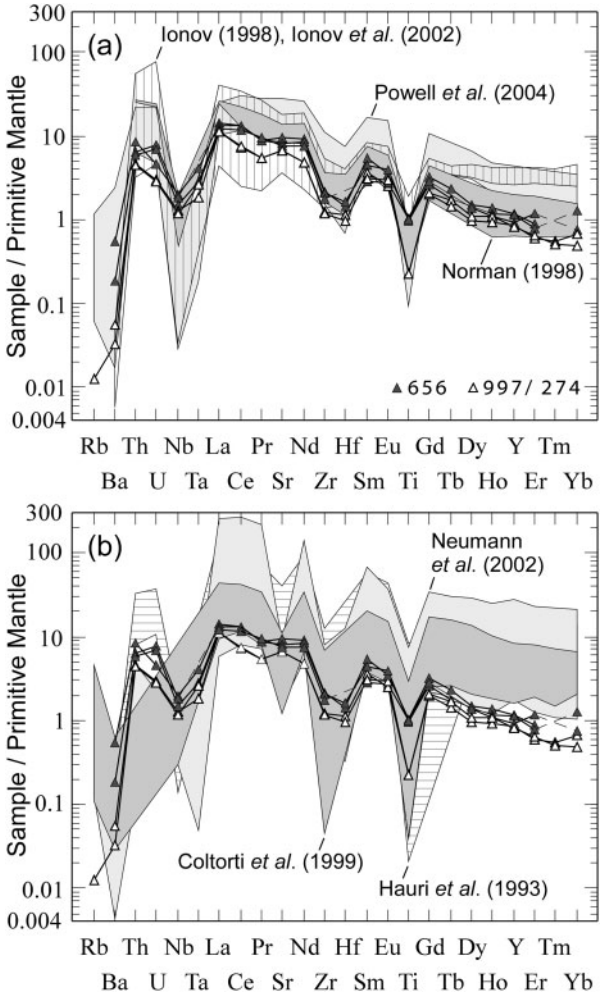

Fig. 11. (a, b) Normalized trace element patterns of relict Cpx I compared with trace element data for clinopyroxenes from a representative set of uppermost mantle xenoliths from different occurrences worldwide for which carbonatite metasomatism has been inferred (Hauri *et al.*, 1993; Ionov, 1998; Norman, 1998; Coltorti *et al.*, 1999; Ionov *et al.*, 2002; Neumann *et al.*, 2002; Powell *et al.*, 2004). However, we are uncertain whether all of these clinopyroxenes formed in equilibrium with primary carbonatite melts. Some of them are characterized by marked Sr depletion (Hauri *et al.*, 1993; Coltorti *et al.*, 1999) that might be caused by the fractionation of carbonates from primary carbonatite melt in the mantle (e.g. Ionov & Harmer, 2002). Evolved carbonatite melts with elevated silica and alkali contents and even strongly carbonated silicate melts may account for the geochemical characteristics of some of the clinopyroxenes used for comparison.

Cpx I in the context of phase relations in the system peridotite–CO_2

The trace element patterns of relict Cpx I are consistent with the patterns of clinopyroxene from mantle xenoliths with strong indications of carbonatite metasomatism (Hauri *et al.*, 1993; Ionov, 1998; Norman, 1998; Coltorti *et al.*, 1999; Ionov *et al.*, 2002; Powell *et al.*, 2004; see Fig. 11). The depletion of Cpx I in Ca suggests that Cpx I coexisted with orthopyroxene. Single-clinopyroxene solvus geothermometers applied to Cpx I yield temperatures of 1040–1060°C (Nimis & Taylor, 2000) and 1135–1155°C [Bertrand & Mercier, 1985, equation (6)], assuming a pressure of 22 kbar. These are moderate temperatures. In the CMS–CO_2 system, they lie well below T_Q (see Wyllie & Huang, 1976; Lee *et al.*, 2000) and even in natural systems they might be lower than the lherzolite–CO_2 solidus ledge temperatures (Fig. 12a). As Cpx I grains are fairly homogeneous and devoid of inclusions, these moderate temperatures might suggest that the host lherzolite underwent textural and chemical re-equlibration after the clinopyroxene has acquired its 'carbonatite' geochemical signature. We are uncertain if garnet was present in the rock. Although the REE patterns of Cpx I are strongly fractionated and exhibit low HREE contents, they compare well with the patterns of clinopyroxene from some spinel lherzolite xenoliths inferred to have undergone carbonatite metasomatism, which are devoid of garnet (Norman, 1998; see Fig. 11a). The depletion of Cpx I in the HREE may reflect the low abundances of these elements in the metasomatizing carbonatite or strongly carbonated silicate melt formed deeper in the mantle, probably in the dolomite–garnet peridotite stability field. The rarity of Cpx I and insufficient data on its paragenetic assemblage hamper further interpretation.

Cpx II and associated phases in the context of phase relations in the system peridotite–CO_2

When a carbonatite or strongly carbonated silicate melt encounters the solidus ledge in the system lherzolite–CO_2 and orthopyroxene reacts out completely according to reaction (1), the enstatite activity in the system becomes unconstrained and, consequently, the Ca content of the clinopyroxene increases. This stage of the reaction process is reflected in the major element composition of Cpx II (Figs 12 and 13). As all carbonate-rich melt inclusions in Cpx II have carbonatitic compositions, we suggest that, during crystallization, Cpx II coexisted with a carbonatite rather than a carbonated silicate melt. Most of such inclusions are Ca-enriched, which is consistent with the experimental data demonstrating Ca enrichment in the carbonate melt that is evolved by reaction (1) (Dalton & Wood, 1993).

Cpx II macrocrysts also contain frequent calcite and aragonite inclusions that are devoid of alkalis and silica and are strongly REE depleted, unlike carbonatite melts in natural systems (e.g. Wallace & Green, 1988; Lee & Wyllie, 1997, 1998). Thus, we interpret the calcite and aragonite present as inclusions in Cpx II as crystal cumulates formed by crystallization of the carbonatite melt remaining after completion of reaction (1). Some inclusions contain calcite enriched in Mg, Fe and Mn. Its presence is suggestive of a high degree of differentiation of the residual carbonatite. Fe–Mn-rich calcite has been described in heterogeneous inclusions containing alkalic brines formed

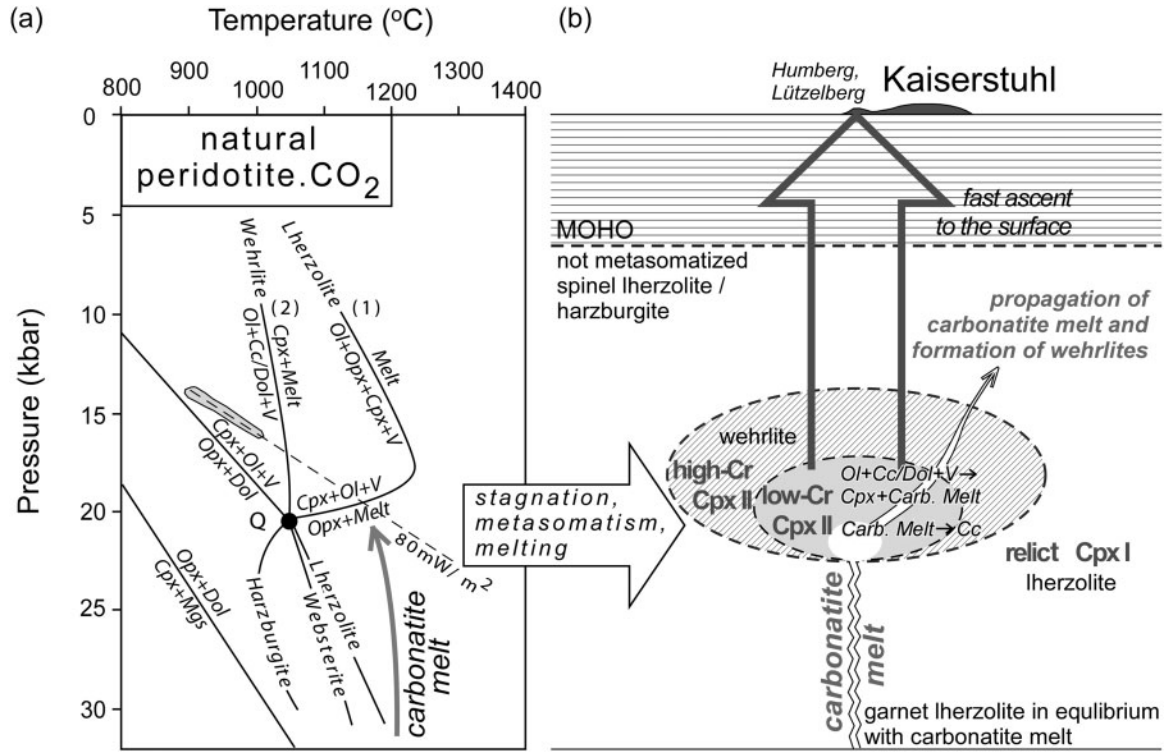

Fig. 12. (a) Schematic illustration of the reaction boundaries for natural carbonated peridotites. The topology of the reaction curves is after Lee *et al*. (2000). The solidus curve for lherzolite–CO_2 is from Falloon & Green (1989). The geometry of the key reaction boundaries including the lherzolite–CO_2 solidus is similar to that in the model system CMS–CO_2 (Olafsson & Eggler, 1983; Wallace & Green, 1988; Falloon & Green, 1989). The principal feature of the solidus is the sharp bend to higher temperature when dolomite / Mg-calcite ceases to form a solidus phase and free fluid appears instead. The shaded area corresponds to the *P–T* range estimated for garnet–spinel peridotite xenoliths from the Kaiserstuhl (Sigmund, 1996; Keller *et al*., 1997). The steady-state conductive geotherm corresponding to a heat flow of 80 mW/m^2 is after Chapman (1986). (b) Schematic illustration of possible relationships between primary carbonate melt and different types of clinopyroxene during formation of the source region of the olivine nephelinite magma. Opx, orthopyroxene; Cpx, clinopyroxene; Ol, olivine; Cc, calcite; Dol, dolomite; Mgs, magnesite; V, vapour.

by crystal differentiation of a parental, magnesian calcic carbonatite melt in the Kalkfeld complex, Namibia (Bühn & Rankin, 1999).

The carbonate-wehrlite assemblage formed by reaction (1) and by concomitant crystallization of carbonate minerals from the remaining carbonatite melt is characterized by low solidus temperatures compared with the solidus of lherzolite–CO_2 (Fig. 12a; see previous section). Therefore, precipitation of carbonate minerals from the carbonatite melt should cause incongruent melting of the carbonate-wehrlite by the reaction Ol + Cc/Dol + CO_2 = Cpx + melt [reaction (2), Figs 12 and 13].

A few grains of high-Cr Cpx II intergrown with olivine are barely distinguishable from relict Cpx I in terms of trace element abundances (Fig. 6a–d). They seem to represent a reaction environment in which reaction (2) terminated quickly as a result of insufficient amount of carbonatite melt. The petrographic and geochemical features of the remaining part of Cpx II (some high-Cr and all low-Cr macrocrysts) are best explained by melting of carbonate-wehrlite according to reaction (2). These pyroxenes do not form aggregates with olivine, but contain olivine as inclusions associated with quenched carbonatite melt, carbonate minerals and fluid inclusions. Some olivine inclusions are strongly resorbed.

In mantle xenoliths that have experienced carbonatite metasomatism Cr–Al-spinel is unstable in the metasomatic textural domains and undergoes resorption and recrystallization (e.g. Ionov *et al*., 1994, 1996; Wiechert *et al*., 1997). The Cr contents of Cpx II decrease rather sharply from high- to low-Cr macrocrysts (Fig. 8). We believe that the Cr content of Cpx II is controlled by the availability of Cr–Al-spinel. High-Cr Cpx II formed in an environment enriched in Cr owing to the continuing process of dissolution of Cr–Al-spinel. Micron-scale Cr–Al-spinel inclusions are relatively frequent in the core areas of high-Cr Cpx II and could be derived by recrystallization of primary Cr–Al-spinel grains. Low-Cr Cpx II formed in an environment where the Cr–Al-spinel was completely consumed or evolved towards compositions strongly enriched in Al (see Table 11, spinel inclusions in Cpx II).

The presence of graphite in some fluid inclusions in low-Cr Cpx II (Fig. 9h) implies that the CCO buffer was occasionally intersected during the reaction process [$-0{\cdot}6$ $\Delta\log(fO_2)^{FMQ}$ at 1100°C/20 kbar; CCO after Woermann & Rosenhauer, 1985; FMQ (fayalite–magnetite–quartz) after O'Neill, 1987]. In this case, reaction (2) is replaced by the carbon–carbonate reaction Ol + Cc/Dol + graphite + CO_2 = Cpx + melt. However, the extreme rarity of the graphite-bearing fluid inclusions and large compositional variations of solid-phase inclusions generally do not allow us to consider this as an equilibrium relationship.

Alkali aluminosilicate glass inclusions in Cpx II and their bearing on the melt generation process

Glass I. Two out of three inclusions containing the extremely rare glass I also contain crystalline calcite and quenched carbonatite melt. Calcite and carbonatite melt volumetrically dominate (Fig. 9f). This is consistent with an origin by liquid immiscibility from a carbonatite parental melt enriched in silica and alkalis owing to calcite crystallization. In the Hamilton projection (Freestone & Hamilton, 1980; Kjarsgaard & Hamilton, 1989), glass I and the quenched carbonatite melts plot on the miscibility gap boundary corresponding to high-*P* conditions (Lee & Wyllie, 1996; Brooker, 1998; see Fig. 10). However, the chemical compositions of carbonatite melts that could be in equilibrium with the tephriphonolitic melt corresponding to glass I are alkali-rich compared with the compositions of the carbonatite melt inclusions in Cpx II (Lee & Wyllie, 1996). A careful investigation of several thin-sections prepared without using water failed to reveal carbonatite melt compositions different from those we have already described. We believe, therefore, that the liquid immiscibility relationships recorded in the inclusions with glass I do not correspond to equilibrium conditions. They may reflect post-entrapment quenching of a formerly homogeneous carbonatite melt.

Glass II. Crystallization differentiation and devolatilization of a silicate melt corresponding to glass I cannot account for the composition of glass II because of the rather low alkali content of the resulting melt. Liquid immiscibility also does not explain the origin of glass II. Under equilibrium conditions, carbonatite melts coexisting with glass II have to be alkalic (Fig. 10). Moreover, quenched carbonatite melt is completely lacking in all heterogeneous inclusions with glass II that we studied.

Petrographic and geochemical data are most consistent with the formation of glass II by segregation from an evolved carbonatite melt (possibly a brine). In heterogeneous inclusions, glass II is often associated with Mg–Mn-rich calcite (see section 'Inclusions in clinopyroxene'). Among the studied macrocrysts and their inclusions, the only non-carbonate phases enriched in Mn are olivine and spinel (0·1–0·2 and 0·3–0·5 wt % MnO, respectively). Volumetrically, olivine dominates. Dissolution of olivine by the reaction Ol + Cc/Dol + vapour = Cpx + carbonatite melt [reaction (2), Fig. 12] results in the crystallization of clinopyroxene, which is Mn depleted compared with olivine. Concomitant precipitation of carbonate minerals from the carbonatite melt should cause extreme fractionation of the latter, as this process leads to a cyclic reaction limited only by the amount of olivine and carbonatite melt and by the stoichiometry of the carbonate phase. It also results in a volatile-enriched residual melt because of crystallization of carbonate minerals from the carbonatite melt. It would be unlikely that such a melt (possibly brine) could be quenched. It probably corresponds to the stage of deep degradation of carbonatite melt during the reaction process and to the onset of silicate melt generation in the system (Fig. 13). Further melting of both olivine and clinopyroxene components and their mixing with the incipient silicate melt corresponding to glass II resulted in the formation of the olivine nephelinite magma (Fig. 13).

Geochemical data and phase relations indicate that a lack of equilibrium is a prerequisite for the formation of glass II. The Na/K ratio of glass II strongly varies in nearby inclusions in the same host clinopyroxene grain. Mg–Mn-rich calcite associated with glass II also shows large compositional variations. These variations cannot be explained by post-entrapment evolution of the inclusions, of which the indications are minor. The lack of equilibrium within and between the reacting domains, probably as a result of fast reaction rates in the presence of a carbonatite melt, is often observed in peridotite xenoliths inferred to have undergone carbonatite metasomatism in the uppermost mantle (e.g. Hauri *et al.*, 1993; Ionov *et al.*, 1996; Coltorti *et al.*, 1999).

Incompatible trace elements during melt generation

The onset of the reaction process discussed above, that is, the formation of the assemblage olivine + clinopyroxene [reaction (1), Fig. 12a], has been implicitly modelled in experimental studies on trace element partitioning between clinopyroxene and carbonatite melt (Brenan & Watson, 1991; Klemme *et al.*, 1995). Among several experimental runs reported by Klemme *et al.* (1995), two (at 20 and 22 kbar) were conducted on a mixture of 30:70 silicate–carbonate components, the former representing a peridotitic composition made of 65% Ol, 30% Opx, and 5% Cpx, whereas the latter was a natural calciocarbonatite from the Kaiserstuhl. Experimental products were olivine, clinopyroxene, and carbonatite melt. Orthopyroxene was completely consumed. Fluid may have formed, although this was not discussed by Klemme *et al.* (1995).

The major element compositions of the clinopyroxenes synthesized by Klemme *et al.* (1995) are comparable with

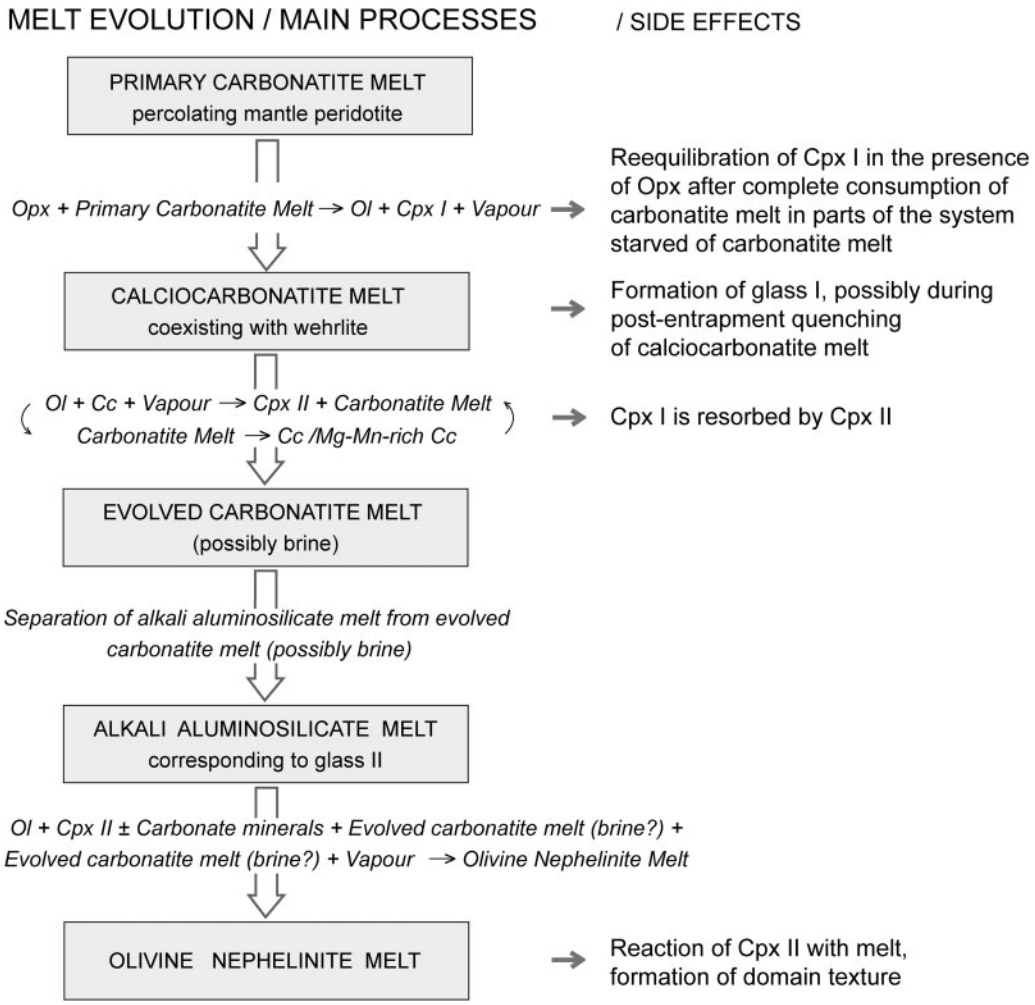

Fig. 13. Schematic illustration of the multi-stage process of formation, evolution and melting of the source region of the olivine nephelinite magma in the uppermost mantle. (For further explanation, see text.)

those of high-Cr Cpx II from our study, especially the clinopyroxene from their run K4 (see Klemme *et al.*, 1995, Table 4). Compared with relict Cpx I, the synthesized clinopyroxene is more calcic and less sodic. The trace element patterns of clinopyroxenes from Klemme *et al.* (1995) and the patterns of Cpx I and some high-Cr Cpx II from this study are presented in Fig. 14a and b. Also shown are the trace element patterns of carbonatite melts coexisting with clinopyroxene in the experiments of Klemme *et al.* (1995) and the whole-rock trace element pattern of the olivine nephelinite from this study. For all elements to the right of La, the patterns of the clinopyroxenes synthesized by Klemme *et al.* (1995) are virtually indistinguishable from those of relict Cpx I and high-Cr Cpx II. For Ba, Nb and Ta, however, large discrepancies are observed. These discrepancies reflect the significantly higher partition coefficients for Ba, Nb and Ta obtained by Klemme *et al.* (1995) compared with several other studies on trace element partitioning between clinopyroxene and carbonatite melt (e.g. Green *et al.*, 1992; Adam & Green, 2001). Adam & Green (2001) suggested that Klemme *et al.*'s (1995) results may have been affected by the contamination of their clinopyroxene analyses by the surrounding carbonatite matrix.

The generally good consistency between our data and the trace element compositions of the clinopyroxenes synthesized by Klemme *et al.* (1995) suggests that the trace element patterns of the coexisting carbonatite melts from Klemme *et al.*'s (1995) experiments (Fig. 14a and b) might represent a reasonable approximation of the trace element composition of the melt involved in the formation of Cpx I and high-Cr Cpx II. An independent evaluation of the trace element composition of the carbonatite melt coexisting with the studied clinopyroxenes is provided in Fig. 14c and d. The trace element abundances of the melts were calculated using the clinopyroxene–carbonatite partition coefficients of Green *et al.* (1992) and Adam & Green (2001). The resultant patterns are lower in Ba and Nb compared with the patterns of Klemme *et al.* (1995), but otherwise similar.

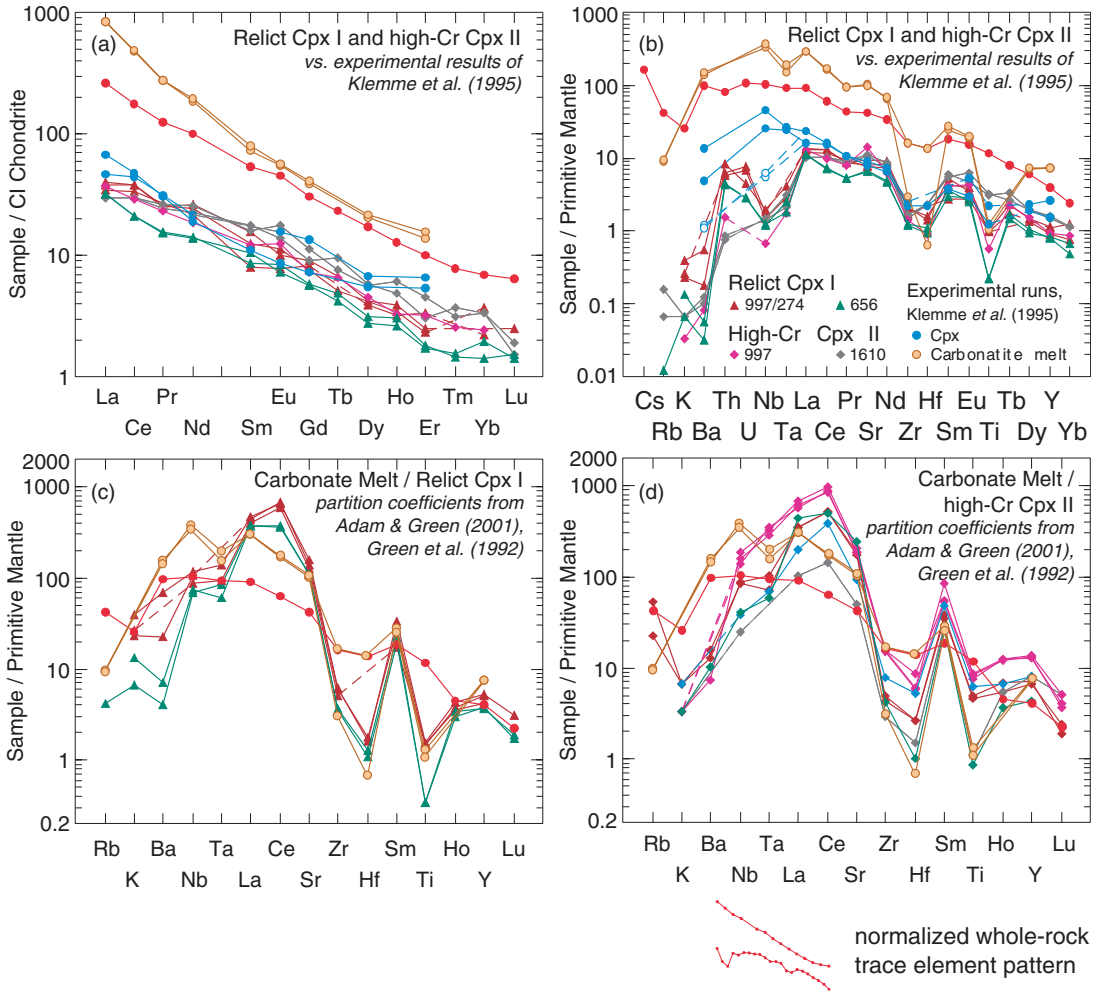

Fig. 14. (a, b) Normalized REE and multi-element patterns of relict Cpx I and some high-Cr Cpx II compared with the trace element patterns of clinopyroxene and coexisting carbonatite melts from the experiments of Klemme *et al.* (1995). Except for the abundances of Zr and Hf, the carbonatite melt patterns are indistinguishable from each other. The variability of Zr and Hf was discussed by Klemme *et al.* (1995). They considered the higher values for Zr and Hf (*c.* 10 times PM) as realistic. On the other hand, independent data on trace element partitioning between clinopyroxene and carbonatite melt (e.g. Green *et al.*, 1992; Adam & Green, 2001) are more compatible with low values for these elements. (c, d) Normalized REE and multi-element patterns of carbonatite liquids computed in equilibrium with relict Cpx I and high-Cr Cpx II. Partition coefficients from Green *et al.* (1992) and Adam & Green (2001) have been used. Normalization values as in Fig. 6.

In terms of their major and trace element compositions, the macrocrysts of low-Cr Cpx II are similar to the Cpx III phenocrysts from the host olivine nephelinite. The only marked difference between them is the lower Sr contents in Cpx III (see Fig. 6f and h). The depletion of Cpx III in Sr is consistent with the presence of carbonate minerals forming inclusions in Cpx II. Crystallization of calcite with a moderate Sr content contributes to the depletion of the coexisting carbonatite melt in Sr relative to LREE and HFSE (see Ionov & Harmer, 2002). Crystallization of Sr-aragonite accelerates this process. The melt in equilibrium with Cpx II has, therefore, probably been depleted in Sr by the precipitation of carbonate minerals.

We also observe a continuous enrichment in Zr, Hf and Ta relative to Sr and REE over the entire sequence of studied clinopyroxenes. Relict Cpx I are strongly depleted in Zr, Hf and Ti, whereas high- and particularly low-Cr Cpx II have higher abundances of these elements, reaching maximum values in Cpx III phenocrysts (see Fig. 6). Amphibole is absent in the studied assemblage. Phlogopite is rare; it sporadically occurs as a late-stage phase in melt–fluid inclusions in Cpx II. As orthopyroxene preferentially accommodates Zr, Hf and Ti (Rampone *et al.*, 1991; McDonough *et al.*, 1992; Norman, 1998), some input of these elements may be expected because of the consumption of orthopyroxene at the onset of the reaction process, although it is unlikely to be the main mechanism

governing the overall Zr, Hf and Ti enrichment of the clinopyroxene phenocrysts.

The principal reactant that could deliver Zr, Hf and Ti in appreciable amounts appears to be the fluid (vapour) released during Opx-out reaction (1). The carbonate-wehrlite solidus reaction (2) is accompanied by the consumption of the fluid (Fig. 12a). Phases associated with fluid inclusions in the clinopyroxenes studied include Ti-rich magnetite and Ti-phlogopite. Ti-rich magnetite in most cases represents late-stage crystal precipitates on the walls of the inclusions. Ti-phlogopite occurs as a reaction phase at the contact between the alkali aluminosilicate glass and the fluid. It is, therefore, reasonable to assume the fluid to be alkalic and Ti-rich (possibly halogen-rich?). Because data on the trace element composition of fluids associated with carbonatite melts in the uppermost mantle are scarce, more *in situ* data are required to evaluate the role of fluid in the studied process.

General evolution of the source region and subsequent magmatic evolution

We propose that the studied suite of macrocrysts and mineral aggregates formed in the pressure range of the solidus ledge in the system lherzolite–CO_2 by interaction of a carbonatite melt with orthopyroxene-bearing mantle rocks, resulting in their transformation to carbonate-wehrlite. Relict Cpx I corresponds to the onset of this process (Fig. 13). Despite its clear 'carbonatite' trace element signature, further data are to elucidate the origin of Cpx I. Some high-Cr Cpx II, olivine and their aggregates record transformation of mantle rocks to carbonate-wehrlite with little or no remaining carbonatite melt. This assemblage was sampled by the magma on ascending to the surface, as a result of spatial proximity and mechanical weakness. Owing to the rheological properties of carbonatite melts (low viscosity and low dihedral wetting angles) the carbonatite melt form an interconnected grain boundary network in an olivine-dominated matrix even at low melt fractions (Hunter & MacKenzie, 1989). Thus, only relict Cpx I that probably re-equilibrated under subsolidus conditions and some high-Cr Cpx II can form aggregates with olivine.

The remaining part of the Cpx II formed during progressive incongruent melting of carbonate-wehrlite. Closed-system crystallization of carbonate minerals from the remaining carbonatite melt, probably under disequilibrium conditions, resulted in extensive fractionation of the carbonatite melt and segregation of incipient alkali aluminosilicate melt(s) (Fig. 13). Rising asthenospheric mantle caused by continuing extensional tectonics in the Rhine graben could have caused increasing temperatures that promoted increasing degrees of partial melting of the assemblage wehrlite + alkali aluminosilicate melt, culminating in the generation of the olivine nephelinite magma (Fig. 13). During this process, Cpx II grains were subjected to dissolution. The relative homogeneity of the core areas of large Cpx II grains and the lack of melt inclusions in Cpx II compositionally similar to the host olivine nephelinite magma suggest that little textural and chemical re-equilibration occurred during this final melting stage. Some limited chemical re-equilibration with the magma is indicated by an increase in Mg-number in the outer parts of the core areas of the Cpx II macrocrysts (Fig. 5b and c). The domain texture in clinopyroxene might have begun to develop at this stage.

Shortly before or during the ascent of the olivine nephelinite melt to the surface, the crystal mush composed of olivine, different types of clinopyroxene and a minor amount of Cr–Al-spinel was homogenized. Low-Cr Cpx II display distinct positive Cr anomalies at the core–rim boundary (Fig. 5c). Dissolution of the remaining grains of Cr–Al-spinel in the homogenized mush of crystals and melt may represent the main cause of this phenomenon. Cr spikes in clinopyroxenes from other alkaline mafic volcanic rocks (e.g. Duda & Schmincke, 1985) are also likely to be related to the dissolution of spinel in the magma. Finally, the elevated Cr content in the early Cpx III phenocrysts is consistent with this process.

En route to the surface, Cpx III phenocrysts began to crystallize and were mantled by Fe-Ti-rich rims at shallower levels. Clinopyroxene and olivine microphenocrysts formed, and olivine macrocrysts, some of them deformed, underwent diffusional re-equilibration towards the composition of the microphenocrysts, resulting in strong chemical zoning (see Electronic Appendix, Fig. A1).

Is carbonate-wehrlite stable under subsolidus conditions at mantle depths?

The solidus of carbonate-wehrlite in the presence of CO_2 corresponds to relatively low temperatures [<1050–1090°C ($=T_Q$); see Fig. 12a]. Therefore, it appears unlikely that carbonate-wehrlite formed by interaction of peridotite mantle rocks with a carbonatite melt can remain in the mantle as solid material. In most thermal regimes, it has to melt. Data on mantle xenoliths from the Kaiserstuhl are consistent with a steady-state heat flow of 80 mW/m^2 (Sigmund, 1996; Keller *et al.*, 1997). The corresponding geotherm intersects the solidus of carbonate-wehrlite at 17 kbar (Fig. 12a). Thus, beneath the Kaiserstuhl, carbonate–wehrlite can remain as a stable phase assemblage in the mantle, where it can undergo textural and chemical re-equilibration under subsolidus conditions, if the pressure does not exceed *c.* 17 kbar. Otherwise, it will melt.

The cores of the studied clinopyroxenes contain alkali aluminosilicate glass and quenched carbonatite melt inclusions, indicating that they formed in the presence of a melt (or melts). We also observe petrographic and geochemical indications of disequilibrium between the coexisting phases. All varieties of calcite and alkali aluminosilicate

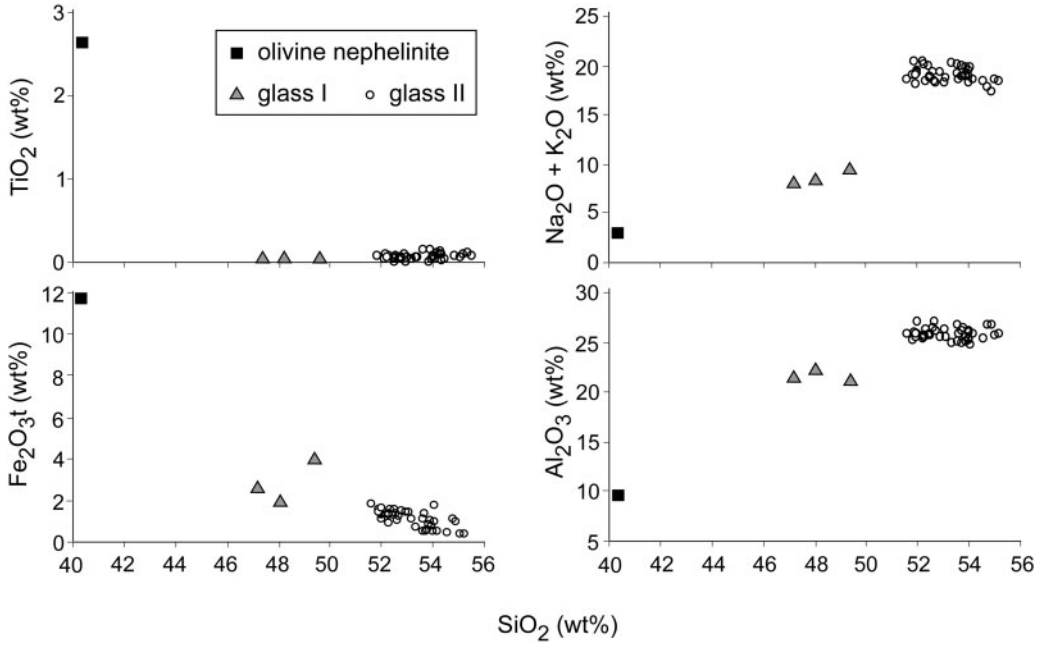

Fig. 15. Major element variation diagrams illustrating the relationships between the compositions of glass I and glass II from inclusions in Cpx II and the bulk composition of the host olivine nephelinite. (For further explanation, see text.)

melt with different K/Na ratios occur in nearby inclusions. Cpx II macrocrysts with fully equilibrated cores do not exist, as some compositional scatter in the microprobe profiles is observed. Together with the physicochemical arguments discussed above, this is inconsistent with textural and chemical re-equilibration of the studied carbonate–wehrlite assemblage under subsolidus conditions and its subsequent melting. We believe that formation of carbonate-wehrlite as a result of interaction of mantle rocks with carbonatite melt along the solidus ledge in the system lherzolite–CO_2 and subsequent melting of the carbonate–wehrlite represents one continuous process.

Fractionation / reaction process as an alternative model

As an alternative to the above model it is possible that the macrocrysts represent the disintegrated relicts of an earlier metasomatic event within the mantle. Both crystal accumulation and metasomatic reaction with wall rocks can occur at the same time during 'percolative fractional crystallization' of an alkaline magma ascending through the upper mantle to the surface (Harte *et al.*, 1993). Deformation features in mantle minerals can possibly be preserved in the course of this process, necessitating additional evidence for an origin of the studied assemblage of macrocrysts and mineral aggregates from the source region of the host magma.

We propose that the key to distinguishing between cumulate and metasomatic minerals entrained during magma ascent and fragments of the magma source region lies in the study of the silicate melt inclusions they contain. In this context, we need to question whether the chemical composition of glass I and II could be explained by fractionation of the olivine nephelinite or a similar magma. Except for the presence of nepheline microlites in some of the large inclusions, we found (almost) no signs of post-entrapment modification of the silicate glass composition. Based on the study of a number of inclusions, we observed a distinct compositional gap between the host olivine nephelinite and glass I and II (Fig. 15). In particular, all the glasses are strongly depleted in Ti compared with the olivine nephelinite (Fig. 15). The cores of the clinopyroxene macrocrysts lack primary inclusions of Ti-rich minerals. Such minerals, including green-core clinopyroxene usually enriched in the HFSE, are absent in the studied macrocryst assemblage. Crystal–liquid differentiation or metasomatic interaction with the wall-rocks should have resulted in enrichment rather than depletion of the residual melt in the HFSE. Sr enrichment and LREE depletion of glass II with respect to the olivine nephelinite are also difficult to explain by fractionation or reaction processes. In addition, textural relationships suggest that rare glass I, which indeed displays some geochemical resemblance to the olivine nephelinite, formed from a carbonatite rather than silicate parental melt (Fig. 9f). The compositional gap between glass II and the host olivine nephelinite cannot be bridged by the compositions of glass I. The presence of a compositional gap is consistent

with the dissolution of the host clinopyroxene in the course of melting during formation of the olivine nephelinite magma, as (primary) melt inclusions cannot be trapped during this process. The fractionation–wall-rock reaction processes do not explain the observed compositional gap.

Mantle xenoliths exhumed by olivine nephelinites

Mantle xenoliths exhumed in volcanic rocks provide independent constraints on the minimum depth of formation of the host magma. Unlike kimberlites and some melilitites and alkali basalts entraining xenoliths equilibrated at high pressures (~70–30 kbar), olivine nephelinites *sensu stricto* contain mostly granulite and low-pressure spinel peridotite and pyroxenite xenoliths. Garnet-bearing peridotite and pyroxenite xenoliths in olivine nephelinites are very rare. Geobarometric data indicate that such xenoliths were equilibrated at relatively low pressures not exceeding those for spinel peridotites (e.g. Sigmund, 1996; Akinin *et al.*, 1997). Mantle xenoliths from the Kaiserstuhl olivine nephelinites, including garnet–spinel peridotites, yield maximum pressures estimates of <22–24 kbar (Sigmund, 1996; Keller *et al.*, 1997). These estimates roughly correspond to the pressure interval along the solidus ledge of carbonated lherzolite, thus highlighting the link between melting reactions on the ledge and the petrogenesis of nephelinitic magmas.

Olivine nephelinites and olivine melilitites

Olivine nephelinites are frequently associated with olivine melilitites. Olivine melilitites represent a large rock group. Some olivine melilitites from cratonic environments contain garnet-lherzolite and harzburgite xenoliths equilibrated at relatively high pressures (37–49 kbar; see Lee & Rudnick, 1999). Off-craton olivine melilitites, such as those of the Upper Rhine graben province in SW Germany, lack xenolith evidence for such a deep level of final melt extraction (Keller *et al.*, 1990; Glahn *et al.*, 1992; Dunworth & Wilson, 1998). Based on the mineralogical and geochemical characteristics of olivine melilitites from the Urach and Hegau volcanic fields of SW Germany and from Mahlberg Castle in the Upper Rhine graben, Dunworth & Wilson (1998) suggested a multi-stage melt generation model. According to their model, a highly carbonated, SiO_2-poor melt rising from the dolomite–garnet peridotite stability field in the asthenosphere reacted with depleted mantle lithologies along the solidus ledge of the system peridotite–CO_2 to form clinopyroxene-rich peridotite. Melting of the latter resulted in the formation of olivine melilitite magma.

The Dunworth & Wilson model complements that presented here, and vice versa. Geographically, the late Tertiary volcanic fields of Urach and Hegau and the Kaiserstuhl belong to the same region, and the olivine melilitite neck at Mahlberg Castle (Fig. 1a) is situated only 20–25 km NNE of the Kaiserstuhl, which itself contains carbonate-rich melilitite rocks (bergalites). Compared with average olivine nephelinite (Nockolds, 1954; Le Bas, 1987), olivine melilitite magmas are more calcic. The chemical composition of the Humberg olivine nephelinite can be derived from the compositions of the Urach and Hegau olivine melilitites by subtracting 3–5% calcite. It seems that either the source region of the olivine melilitite magma contains more extensively carbonated material than the source region of olivine nephelinite, or that olivine melilitite represents a smaller degree partial melt than olivine nephelinite, resulting in the dilution of the carbonate component in the olivine nephelinite magma. Otherwise, the source regions of both magma types appear to be similar, both genetically and in terms of phase assemblage (carbonate-wehrlite). On-craton olivine melilitites from the dolomite–garnet peridotite stability field are not discussed here.

Carbonatites and olivine nephelinites in bimodal carbonatite–alkali silicate rock associations

The regional association of nephelinitic rocks with carbonatites is firmly established both in the Kaiserstuhl and worldwide. Four processes are currently favoured to explain the origin of this association: (1) fractional crystallization of a carbonated nepheline-rich magma (e.g. Watkinson & Wyllie, 1971; Lee & Wyllie, 1994); (2) separation of two immiscible liquids, nephelinitic and carbonatitic, from a carbonated primary or evolved alkali silicate magma (e.g. Koster van Groos & Wyllie, 1963; Kjarsgaard & Hamilton, 1989; Lee & Wyllie, 1997, 1998; Kjarsgaard, 1998); (3) partial melting of carbonate-amphibole or amphibole–peridotite in the uppermost mantle (e.g. Olafsson & Eggler, 1983); (4) generation of a sequence of primary carbonate and silicate magmas by partial melting of carbonated peridotite deep in the mantle (e.g. Moore & Wood, 1998). The first process has more relevance to the formation of intrusive alkali silicate rock–carbonatite complexes rather than volcanic associations of nephelinites and carbonatites (e.g. Watkinson & Wyllie, 1971). The process of liquid immiscibility appears both important and widespread in carbonated alkali silicate magmas, but it does not account for the origin of the silicate precursors themselves. The partial melting of (carbonate–) amphibole peridotites that can potentially form by interaction of primary carbonatite melts or related fluids with peridotite mantle lithologies in the uppermost mantle above the solidus ledge of carbonated peridotite requires amphibole in the source region and seems to leave orthopyroxene as a residual phase (Olafsson & Eggler, 1983). More recently, Moore & Wood (1998) made an attempt to explain the binary nature of the

silicate–carbonatite association in the context of primary carbonatite magmas originating in the mantle at pressures greater than the solidus ledge (>~70 km). Isotopic studies and evidence based on mantle xenocrysts and garnet peridotite and eclogite xenoliths in effusive carbonatites have led to the conclusion that primary carbonatite melts may reach the Earth's surface without being trapped and consumed on the ledge (e.g. Bailey, 1989; Harmer & Gittins, 1998). In the pressure range between the ledge and the Moho (from 70 to 20–40 km), the only peridotite that can coexist with a carbonatite melt is a wehrlite. Once channels in the uppermost mantle protected by metasomatic wehrlites are established, carbonatite melts are able to survive and ascend to the surface (Moore & Wood, 1998; Lee & Wyllie, 2000). With an increase in temperature, at higher degrees of partial melting, silicate melts with moderate CO_2 contents can be generated from carbonated peridotite below the solidus ledge instead of carbonatites. It should be noted that this process may bear more relevance to the origin of kimberlites and some melilitites rather than nephelinites; it also generates orthopyroxene-bearing residues (Moore & Wood, 1998; Gudfinnson & Presnall, 2005).

The exact nature of the processes that led to the generation of the Kaiserstuhl carbonatites appears uncertain, as well as their relationships with the olivine nephelinites. In fact, all four mechanisms mentioned above have been speculatively invoked over the last two decades to explain these relationships (Keller, 1984; Keller *et al.*, 1990; Schleicher *et al.*, 1990, 1991). The Kaiserstuhl carbonatites are characterized by isotope disequilibrium with the associated olivine nephelinitic and limburgitic as well as tephritic rocks. The carbonatites have more radiogenic Nd and Pb isotopic compositions compared with the olivine nephelinites (Schleicher *et al.*, 1990, 1991). Thus, the carbonatites and the olivine nephelinites cannot represent unmodified immiscible melts separated from a common carbonated silicate parental magma (Schleicher *et al.*, 1990, 1991). On the other hand, the Kaiserstuhl bergalites (carbonatite–melilitite rocks) have isotopic characteristics similar to those of the carbonatites (e.g. Schleicher *et al.*, 1990). However, less carbonated melilititic or nephelinitic rocks that would be complementary to the bergalites in terms of isotopic composition have not yet been found in the Kaiserstuhl.

In the uppermost mantle beneath the Kaiserstuhl, the relationships between carbonatite and olivine nephelinite appear to be genetic. This study strongly supports the conclusion that primary carbonatite melts rising from depths below the solidus ledge of carbonate–peridotite can play a major role in the formation of the source region for olivine nephelinite. The primary carbonatite melts metasomatize the mantle to form wehrlites, and the complementary nephelinitic magmas are generated by partial melting of the wehrlites. At intermediate degrees of melting, highly carbonated silicate melts may form and subsequently exsolve carbonatitic liquids on ascending to the Earth's surface, thus generating new carbonatites at shallower depths. At higher degrees of melting, olivine nephelinite magmas with lower CO_2 contents will appear. The primary carbonatite magmas are largely consumed at the solidus ledge and do not reach the surface; this partly explains the large volumes of nephelinitic rocks accompanied by only minor volumes of carbonatites in many occurrences of carbonatite and alkalic silicate rocks worldwide. In nature, the formation of primary carbonate and silicate magmas below the solidus ledge of carbonated peridotite (Moore & Wood, 1998), formation of nephelinitic magmas on the solidus ledge as a result of the supply of primary carbonatite melts from below the ledge (this study), and low-pressure liquid immiscibility traditionally invoked to explain the relationships between carbonatites and nephelinitic rocks are unlikely to be mutually exclusive processes.

CONCLUSIONS

Mineral and bulk-rock compositions of the olivine nephelinite from the Humberg, Kaiserstuhl, represent a mixture of primary melt and disintegrated fragments (10–15%) of the source region. The source region material is dominated by clinopyroxene and olivine.

The magma generation process was multi-stage. A primary carbonatite melt formed deep in the mantle, probably in the carbonate–garnet peridotite stability field. On migrating upwards, it interacted with mantle peridotite in the pressure range of the solidus ledge in the system lherzolite–CO_2 (*c.* 20–22 kbar in natural peridotite systems) by the reaction Opx + carbonate melt = Ol + Cpx + CO_2. It also crystallized carbonate minerals. After complete conversion of orthopyroxene, the resulting carbonate-wehrlite assemblage began to melt incongruently according to the reaction Ol + Cc/Dol + CO_2 = Cpx + melt corresponding to the solidus of carbonate-wehrlite. The residual carbonatite melt continued to crystallize carbonate minerals and evolved towards enrichment in Mg, Mn and volatile components, leaving Mg–Mn-enriched calcite as a crystal cumulate and possibly transforming to a brine. The very first portions of silicate melt in the system might have separated from this evolved carbonatite melt or brine; they were alkali-, alumina- and silica-rich and strongly depleted in mafic components. Further melting of the carbonate-wehrlite assemblage in the presence of the alkali aluminosilicate melt led to the dissolution of the solid phases (olivine + clinopyroxene ± carbonate minerals) and resulted in the generation of olivine nephelinite magma. The magma partly entrained clinopyroxene and olivine

from the source region and brought them to the Earth's surface.

The association of primary carbonatite, melilititic and nephelinitic melts in the uppermost mantle in the pressure range of the solidus ledge of carbonate peridotite is genetic. It partly accounts for the regional association of foidites and foidolites with melilitites and carbonatites, especially with carbonatites considered as primary mantle melts.

ACKNOWLEDGEMENTS

We would like to thank Edwin Gnos and Vincent Serneels for the analytical support. Constructive and insightful reviews provided by two anonymous reviewers helped us to significantly improve the earlier version of the manuscript. Discussions with Jörg Keller about the geology of the Kaiserstuhl olivine nephelinites were much appreciated. We are grateful to Marjorie Wilson for her valuable comments and editorial handling of the manuscript. This research was supported by the Swiss National Science Foundation grants PP002-102809 and 200021-101665.205.

SUPPLEMENTARY DATA

Supplementary data for this paper are available at http://www.petrology.oxfordjournals.org.

REFERENCES

Adam, J. (1990). The geochemistry and experimental petrology of sodic alkaline basalts from Oatlands, Tasmania. *Journal of Petrology* **31**, 1201–1223.

Adam, J. & Green, T. (2001). Experimentally determined partition coefficients for minor and trace elements in peridotite minerals and carbonatitic melt, and their relevance to natural carbonatites. *European Journal of Mineralogy* **13**, 815–827.

Akinin, V. V., Roden, M. F., Francis, D. M., Apt, J. E. & Moll-Stalcup, E. (1997). Compositional and thermal state of the upper mantle beneath the Bering Sea Basalt Province: evidence from the Chukchi Peninsula of Russia. *Canadian Journal of Earth Sciences* **34**, 789–800.

Bailey, D. K. (1989). Carbonate melts from the mantle in the volcanoes of south-east Zambia. *Nature* **338**, 415–418.

Bertrand, P. & Mercier, J.-C. (1985). The mutual solubility of coexisting ortho- and clinopyroxene: toward an absolute geothermometer for the natural system. *Earth and Planetary Science Letters* **76**, 109–122.

Blundy, J. & Dalton, J. (2000). Experimental comparison of trace element partitioning between clinopyroxene and melt in carbonate and silicate systems, and implications for mantle metasomatism. *Contributions to Mineralogy and Petrology* **139**, 356–371.

Boyd, F. R. (1973). A pyroxene geotherm. *Geochimica et Cosmochimica Acta* **31**, 2533–2546.

Brenan, J. M. & Watson, E. B. (1991). Partitioning of trace elements between carbonatite melt and clinopyroxene and olivine at mantle *P–T* conditions. *Geochimica et Cosmochimica Acta* **55**, 2203–2214.

Brey, G. & Green, D. H. (1977). Systematic study of liquidus phase relationships in olivine melilitite + H_2O + CO_2 at high pressures and petrogenesis of an olivine melilitite magma. *Contributions to Mineralogy and Petrology* **61**, 141–162.

Brey, G. P. & Köhler, T. (1990). Geothermobarometry in four-phase lherzolites II. New thermobarometers, and practical assessment of existing thermobarometers. *Journal of Petrology* **31**, 1353–1378.

Brey, G., Brice, W. R., Ellis, D. J., Green, D. H., Harris, K. L. & Ryabchikov, I. D. (1983). Pyroxene–carbonate reactions in the upper mantle. *Earth and Planetary Science Letters* **62**, 63–74.

Brooker, R. A. (1998). The effect of CO_2 saturation on immiscibility between silicate and carbonate liquids: an experimental study. *Journal of Petrology* **39**, 1905–1915.

Bühn, B. & Rankin, A. H. (1999). Composition of natural, volatile-rich Na–Ca–REE–Sr carbonatitic fluids trapped in fluid inclusions. *Geochimica et Cosmochimica Acta* **63**, 3781–3797.

Bultitude, R. J. & Green, D. H. (1971). Experimental studies of crystal–liquid relationships at high pressures in olivine nephelinite and basanite compositions. *Journal of Petrology* **12**, 121–147.

Chapman, D. S. (1986). Thermal gradients in the continental crust. In: Dawson, J. B., Carswell, D. A., Hall, J. & Wedepohl, K. H. (eds) *The Nature of the Lower Continental Crust. Geological Society, London, Special Publications* **24**, 63–70.

Coltorti, M., Bonadiman, C., Hinton, R. W., Siena, F. & Upton, B. G. J. (1999). Carbonatite metasomatism of the oceanic upper mantle: evidence from clinopyroxenes and glasses in ultramafic xenoliths of Grande Comore, Indian Ocean. *Journal of Petrology* **40**, 133–165.

Dalton, J. A. & Wood, B. J. (1993). The compositions of primary carbonate melts and their evolution through wallrock reaction in the mantle. *Earth and Planetary Science Letters* **119**, 511–525.

Dawson, J. B. (1980). *Kimberlites and their Xenoliths*.Berlin: Springer, 252 pp.

Dawson, J. B. (2002). Metasomatism and partial melting in upper-mantle peridotite xenoliths from the Lashaine Volcano, Northern Tanzania. *Journal of Petrology* **43**, 1749–1777.

Dobosi, G. & Fodor, R. V. (1992). Magma fractionation, replenishment, and mixing as inferred from green-core clinopyroxenes in Pliocene basanite, southern Slovakia. *Lithos* **28**, 133–150.

Dobson, D. P., Jones, A. P., Rabe, R., Sekine, T., Kurita, K., Taniguchi, T., Kondo, T., Kato, T., Shimomura, O. & Urakawa, S. (1996). *In-situ* measurements of viscosity and density of carbonate melts at high pressure. *Earth and Planetary Science Letters* **143**, 207–215.

Duda, A. & Schmincke, H. U. (1985). Polybaric differentiation of alkali basaltic magmas: evidence from green-core clinopyroxenes (Eifel, F.R.G.). *Contributions to Mineralogy and Petrology* **91**, 340–353.

Dunworth, E. A. & Wilson, M. (1998). Olivine melilitites of the SW German Tertiary volcanic province: mineralogy and petrogenesis. *Journal of Petrology* **39**, 1805–1836.

Edel, J. B., Fuchs, K., Gelbke, C. & Prodehl, C. (1975). Deep structure of the southern Rhine Graben area from seismic refraction investigations. *Geophysical Journal International* **41**, 333–356.

Eggler, D. H. (1974). Effect of CO_2 on the melting of peridotite. *Carnegie Institution of Washington Yearbook* **73**, 215–224.

Eggler, D. H. (1976). Composition of the partial melt of carbonated peridotite in the system CaO–MgO–SiO_2–CO_2. *Carnegie Institution of Washington Yearbook* **75**, 623–626.

Eggler, D. H. (1978). The effect of CO_2 upon partial melting of peridotite in the system Na_2O–CaO–Al_2O_3–MgO–SiO_2–CO_2 to 35 kbar, with an analysis of melting in a peridotite–H_2O–CO_2 system. *American Journal of Science* **278**, 305–343.

Falloon, T. J. & Green, D. H. (1989). The solidus of carbonated, fertile peridotite. *Earth and Planetary Science Letters* **94**, 364–370.

Freestone, I. C. & Hamilton, D. L. (1980). The role of liquid immiscibility in the genesis of carbonatites—an experimental study. *Contributions to Mineralogy and Petrology* **73**, 105–117.

Furman, T. (1995). Melting of metasomatized subcontinental lithosphere: undersaturated mafic lavas from Rungwe, Tanzania. *Contributions to Mineralogy and Petrology* **122**, 97–115.

Girnis, A. V., Brey, G. P. & Ryabchikov, I. D. (1995). Origin of Group 1A kimberlites: fluid-saturated melting experiments at 45–55 kbar. *Earth and Planetary Science Letters* **134**, 283–296.

Glahn, A. & Granet, M. (1992). 3-D structure of the lithosphere beneath the southern Rhine Graben area. *Tectonophysics* **208**, 149–158.

Glahn, A., Sachs, P. M. & Achauer, U. (1992). A teleseismic and petrological study of the crust and upper mantle beneath the geothermal anomaly Urach/SW Germany. *Physics of the Earth and Planetary Interiors* **69**, 176–206.

Green, D. H. (1973). Conditions of melting of basanite magma from garnet peridotite. *Earth and Planetary Science Letters* **17**, 456–465.

Green, D. H. & Wallace, M. E. (1988). Mantle metasomatism by ephemeral carbonatite melts. *Nature* **336**, 459–462.

Green, T. H., Adam, J. & Sie, S. H. (1992). Trace element partitioning between silicate minerals and carbonatite at 25 kbar and application to mantle metasomatism. *Mineralogy and Petrology* **46**, 179–184.

Greenough, J. D. (1988). Minor phases in the Earth's mantle: evidence from trace- and minor-element patterns in primitive alkaline magmas. *Chemical Geology* **69**, 177–192.

Griffin, W. L., O'Reilly, S. Y. & Ryan, C. G. (1999). The composition and origin of sub-continental lithospheric mantle. In: Fei. Y., Bertka, C. M. & Mysen B. O. (eds) *Mantle Petrology: Field Observations and High-pressure Experimentation: a Tribute to Francis R (Joe) Boyd. Geochemical Society, Special Publications* **6**, 13–43.

Gudfinnson, G. H. & Presnall, D. C. (2005). Continuous gradations among primary carbonatitic, kimberlitic, melilititic, basaltic, picritic, and komatiitic melts in equilibrium with garnet lherzolite at 3–8 GPa. *Journal of Petrology* **46**, 1645–1659.

Günther, D., Frischknecht, R. & Heinrich, C. A. (1997). Capabilities of a 193 nm ArF excimer laser for LA-ICPMS micro analysis of geological materials. *Journal of Analytical Atomic Spectrometry* **12**, 939–944.

Haak, V., Sengpiel, K.-P., Berktold, A. & Greinwald, S. (1970). The telluric method: results of the measurements along a profile across the Rhinegraben between Stuttgart and Kaiserslautern. In: Illies, J. H. & Müller, St. (eds) *Graben Problems*. Stuttgart: Schweizerbart, pp. 235–242.

Harmer, R. E. & Gittins, J. (1998). The case for primary, mantle-derived carbonatite magma. *Journal of Petrology* **39**, 1895–1903.

Harte, B., Hunter, R. H. & Kinny, P. D. (1993). Melt geometry, movement and crystallization, in relation to mantle dykes, veins and metasomatism. *Philosophical Transactions of the Royal Society of London, Series A* **342**, 1–21.

Hauri, E. H., Shimizu, N., Dieu, J. J. & Hart, S. R. (1993). Evidence for hot-spot related carbonatite metasomatism in the upper mantle. *Nature* **365**, 221–227.

Heinrich, C. A., Pettke, T., Halter, W. E., Aigner-Torres, M., Audétat, A., Günther, D., Hattendorf, B., Bleiner, D., Guillong, M. & Horn, I. (2003). Quantitative multi-element analysis of minerals, fluid and melt inclusions by laser-ablation inductively-coupled-plasma mass-spectrometry. *Geochimica et Cosmochimica Acta* **67**, 3473–3496.

Henjes-Kunst, F. & Altherr, R. (1992). Metamorphic petrology of xenoliths from Kenya and northern Tanzania and implications for geotherms and lithospheric structures. *Journal of Petrology* **33**, 1125–1156.

Hubberten, H. W., Katz-Lehnert, K. & Keller, J. (1988). Carbon and oxygen isotope investigations in carbonatites and related rocks from the Kaiserstuhl, Germany. *Chemical Geology* **70**, 257–274.

Hunter, R. H. & MacKenzie, D. (1989). The equilibrium geometry of carbonate melts in rocks of mantle composition. *Earth and Planetary Science Letters* **92**, 347–356.

Ionov, D. A. (1998). Trace element composition of mantle-derived carbonates and coexisting phases in peridotite xenoliths from alkali basalts. *Journal of Petrology* **39**, 1931–1941.

Ionov, D. A. & Harmer, R. E. (2002). Trace-element distribution in calcite–dolomite carbonatites from Spitskop: inferences for differentiation of carbonatite magma and origin of carbonates in mantle xenoliths. *Earth and Planetary Science Letters* **198**, 495–510.

Ionov, D. A., Dupuy, C., O'Reilly, S. Y., Kopylova, M. G. & Genshaft, Y. S. (1993). Carbonated peridotite xenoliths from Spitsbergen: implications for trace element signature of mantle carbonate metasomatism. *Earth and Planetary Science Letters* **119**, 283–297.

Ionov, D. A., Hofmann, A. W. & Shimizu, N. (1994). Metasomatism-induced melting in mantle xenoliths from Mongolia. *Journal of Petrology* **35**, 753–785.

Ionov, D. A., O'Reilly, S. Y., Genshaft, Y. S. & Kopylova, M. G. (1996). Carbonate-bearing mantle peridotite xenoliths from Spitsbergen: phase relationships, mineral compositions and trace-element residence. *Contributions to Mineralogy and Petrology* **125**, 375–392.

Ionov, D. A., Bodinier, J.-L., Mukasa, S. B. & Zanetti, A. (2002). Mechanism and sources of mantle metasomatism: major and trace element compositions of peridotite xenoliths from Spitsbergen in the context of numerical modelling. *Journal of Petrology* **43**, 2219–2259.

Illies, J. H. (1970). Graben tectonics as related to crust–mantle interactions. In: Illies, J. H. & Müller, St. (eds) *Graben Problems*. Stuttgart: Schweizerbart, pp. 4–27.

Illies, J. H. (1975). Intraplate tectonics in stable Europe as related to plate tectonics in the Alpine system. *Geologische Rundschau* **64**, 677–699.

Kahle, H.-G. & Werner, D. (1980). A geophysical study of the Rhinegraben—II. Gravity anomalies and geothermal implications. *Geophysical Journal International* **62**, 631–647.

Keller, J. (1977). Frühe Mineralanalysen im Kaiserstuhl im Vergleich mit modernen Mikrosondendaten. *Berichte der Naturforschenden Gesellschaft zu Freiburg im Breisgau* **67**, 113–125.

Keller, J. (1978). Megakristalle von Al-reichem Klinopyroxen in Olivinnepheliniten und deren experimentelle Modellierung als Hochdruck-Liquidphasen. *Fortschritte der Mineralogie* **56**, 56–57.

Keller, J. (1984). Der jungtertiäre Vulkanismus Südwestdeutschlands: Excursionen im Kaiserstuhl und Hegau. *Fortschritte der Mineralogie* **62**, 2–35.

Keller, J., Brey, G., Lorenz, V., Sachs, P. & Schleicher, H. (1990). *IAVCEI 1990 Preconference excursion 2a: volcanism and petrology of the upper Rheinegraben (Urach–Hegau–Kaiserstuhl) and Post-conference excursion 2b: volcanism and petrology of Kaiserstuhl. Excursion Guide, Mainz: IAVCEI*, pp. 1–63.

Keller, J., Sigmund, J., Müller-Sigmund, H. & Czirjak, A. (1997). Mantle xenoliths in Rhinegraben volcanics from the Black Forest–Vosges dome. In:. *Abstracts of the 9th European Union of Geosciences Conference (EUG9), Strasbourg. Terra Nova* **9(Abstract Supplement 1): 56.**

Keller, J., Kraml, M. & Henjes-Kunst, F. (2002). $^{40}Ar/^{39}Ar$ single crystal laser dating of early volcanism in the Upper Rhine Graben and tectonic implications. *Schweizerische Mineralogische und Petrographische Mitteilungen* **82**, 121–130.

Kjarsgaard, B. A. (1998). Phase relations of a carbonated high-CaO nephelinite at 0·2 and 0·5 GPa. *Journal of Petrology* **39**, 2061–2075.

Kjarsgaard, B. A. & Hamilton, D. L. (1989). The genesis of carbonatites by liquid immiscibility. In: Bell, K. (ed.) *Carbonatites: Genesis and Evolution*. London: Unwin Hyman, pp. 388–404.

Klemme, S., van der Laan, S. R., Foley, S. F. & Günther, D. (1995). Experimentally determined trace and major element partitioning between clinopyroxene and carbonatite melt under upper mantle conditions. *Earth and Planetary Science Letters* **133**, 439–448.

Koch, M. (1993). Simultaneous inversion for three-dimensional crustal structure and hypocenters including direct, refracted and reflected phases. III. Application to the southern Rhinegraben, Germany. *Geophysical Journal International* **112**, 429–447.

Kopylova, M. G. & Caro, G. (2004). Mantle Xenoliths from the Southeastern slave craton: evidence for chemical zonation in a thick, cold lithosphere. *Journal of Petrology* **45**, 1045–1067.

Koster van Groos, A. F. & Wyllie, P. J. (1963). Experimental data bearing on the role of liquid immiscibility in the genesis of carbonatites. *Nature* **199**, 801–802.

Kraml, M., Keller, J. & Henjes-Kunst, F. (1995). New K/Ar, $^{40}Ar/^{39}Ar$ step-heating and $^{40}Ar/^{39}Ar$ laser fusion dates for the Kaiserstuhl volcanic complex (Upper Rhine Graben; Germany). *European Journal of Mineralogy, Beihefte* **7**(1), 142.

Le Bas, M. J. (1987). Nephelinites and carbonatites. In: Fitton, J. G. & Upton B. G. J. (eds) *Alkaline Igneous Rocks. Geological Society, London, Special Publications* **30**, 53–83.

Le Bas, M. J. (1989). Nephelinitic and basanitic rocks. *Journal of Petrology* **30**, 1299–1312.

Lee, C.-T. & Rudnick, R. L. (1999). Compositionally stratified cratonic lithosphere: petrology and geochemistry of peridotite xenoliths from the Labait tuff cone, Tanzania. In: Gurney, J. J., Gurney, J. L., Pascoe, M. D. & Richardson, S. H. (eds) *Proceedings of the 7th International Kimberlite Conference*. Cape Town: Red Roof Design, pp. 503–521.

Lee, W. J. & Wyllie, P. J. (1994). Experimental data bearing on liquid immiscibility, crystal fractionation, and the origin of calciocarbonatites and natrocarbonatites. *International Geology Review* **36**, 797–819.

Lee, W. J. & Wyllie, P. J. (1996). Liquid immiscibility in the join $NaAlSi_3O_8$–$CaCO_3$ to 2·5 GPa and the origin of calciocarbonatite magmas. *Journal of Petrology* **37**, 1125–1152.

Lee, W. J. & Wyllie, P. J. (1997). Liquid immiscibility between nephelinite and carbonatite from 1·0 to 2·5 GPa compared with mantle melt compositions. *Contributions to Mineralogy and Petrology* **127**, 1–16.

Lee, W. J. & Wyllie, P. J. (1998). Petrogenesis of carbonatite magmas from mantle to crust, constrained by the system CaO–$(MgO + FeO^*)$–$(Na_2O + K_2O)$–$(SiO_2 + Al_2O_3 + TiO_2)$–$CO_2$. *Journal of Petrology* **39**, 495–517.

Lee, W. J. & Wyllie, P. J. (2000). The system CaO–MgO–SiO_2–CO_2 at 1 GPa, metasomatic wehrlites, and primary carbonatite magmas. *Contributions to Mineralogy and Petrology* **138**, 214–228.

Lee, W. J., Huang, W. L. & Wyllie, P. (2000). Melts in the mantle modeled in the system CaO–MgO–SiO_2–CO_2 at 2·7 GPa. *Contributions to Mineralogy and Petrology* **138**, 199–213.

Le Maitre, R. W., Bateman, P., Dudek, A., Keller, J., Lameyre, P., Le Bas, M. J., Sabine, P. A., Schmid, R., Soerensen, H., Streckeisen, A., Woolley, A. R. & Zanettin, B. (2002). *A Classification of Igneous Rocks and Glossary of Terms: Recommendations of the IUGS Subcommission on the Systematics of Igneous Rocks*, 2nd edn. Cambridge: Cambridge University Press, 204 pp.

Lippolt, H. J., Gentner, W. & Wimmenauer, W. (1963). Altersbestimmungen nach der Kalium–Argon Methode an tertiären Eruptivgesteinen Südwestdeutschlands. *Jahreshefte des Geologischen Landesamts Baden-Württemberg* **6**, 507–538.

Lloyd, F. E. (1981). Upper-mantle metasomatism beneath a continental rift: clinopyroxenes in alkali mafic lavas and nodules from South West Uganda. *Mineralogical Magazine* **44**, 315–323.

MacKenzie, J. M. & Canil, D. (1999). Composition and thermal evolution of cratonic mantle beneath the central Archean Slave Province, NWT, Canada. *Contributions to Mineralogy and Petrology* **134**, 313–324.

McDonough, W. F., Stosch, H. G. & Ware, N. G. (1992). Distribution of titanium and the rare earth elements between peridotitic minerals. *Contributions to Mineralogy and Petrology* **110**, 321–328.

Menzies, M. A. (ed.) (1990). *Continental Mantle*. Oxford: Clarendon Press, 200 pp.

Mitchell, R. H. (1995). *Kimberlites, Orangeites, and Related Rocks*. New York: Plenum, 410 pp.

Moore, K. R. & Wood, B. J. (1998). The transition from carbonate to silicate melts in the CaO–MgO–SiO_2–CO_2 system. *Journal of Petrology* **39**, 1943–1951.

Nelson, D. R., Chivas, A. R., Chappel, B. W. & McCulloch, M. T. (1988). Geochemical and isotopic systematics in carbonatites and implications for the evolution of ocean-island sources. *Geochimica et Cosmochimica Acta* **52**, 1–17.

Neumann, E.-R., Wulff-Pedersen, E., Pearson, N. J. & Spencer, E. A. (2002). Mantle xenoliths from Tenerife (Canary Islands): evidence for reactions between mantle peridotites and silicic carbonatite melts inducing Ca metasomatism. *Journal of Petrology* **43**, 825–857.

Nimis, P. & Taylor, W. (2000). Single clinopyroxene thermobarometry for garnet peridotites. Part I. Calibration and testing of a Cr-in-Cpx barometer and an enstatite-in-Cpx thermometer. *Contributions to Mineralogy and Petrology* **139**, 541–554.

Nixon, P. H. (ed.) (1987). *Mantle Xenoliths*. New York: John Wiley, 844 pp.

Nockolds, S. R. (1954). Average chemical compositions of some igneous rocks. *Geological Society of America Bulletin* **65**, 1007–1032.

Norman, M. D. (1998). Melting and metasomatism in the continental lithosphere: laser ablation ICPMS analysis of minerals in spinel lherzolites from eastern Australia. *Contributions to Mineralogy and Petrology* **130**, 240–255.

Norry, M. J., Truckle, P. H., Lippard, S. J., Hawkesworth, C. J., Weaver, C. D. & Marriner, C. F. (1980). Isotopic and trace element evidence from lavas, bearing on mantle heterogeneity beneath Kenya. *Philosophical Transactions of the Royal Society of London, Series A* **97**, 259–271.

Olafsson, M. & Eggler, D. H. (1983). Phase relations of amphibole–carbonate, and phlogopite–carbonate peridotite: petrologic constraints on the astenosphere. *Earth and Planetary Science Letters* **64**, 305–315.

O'Neill, H. St. C. (1987). The quartz–fayalite–iron and quartz–fayalite–magnetite equilibria and the free energies of formation of fayalite (Fe_2SiO_4) and magnetite (Fe_3O_4). *American Mineralogist* **72**, 67–75.

Pettke, T., Halter, W. E., Webster, J. D., Aigner-Torres, M. & Heinrich, C. A. (2004). Accurate quantification of melt inclusion chemistry by LA-ICPMS: a comparison with EMP and SIMS and advantages and possible limitations of these methods. *Lithos* **78**, 333–361.

Pilet, S., Hernandez, J. & Villemant, B. (2002). Evidence for high silicic melt circulation and metasomatic events in the mantle beneath alkaline provinces: the Na–Fe-augitic green-core pyroxenes in the Tertiary alkali basalts of the Cantal massif (French Massif Central). *Mineralogy and Petrology* **76**, 39–62.

Powell, W., Zhang, M., O'Reilly, S. Y. & Tiepolo, M. (2004). Mantle amphibole trace-element and isotopic signatures trace multiple metasomatic episodes in lithospheric mantle, western Victoria, Australia. *Lithos* **75**, 141–171.

Rampone, E., Bottazi, P. & Ottolini, L. (1991). Complementary Ti and Zr anomalies in orthopyroxene and clinopyroxene from mantle peridotites. *Nature* **354**, 518–520.

Rudnick, R. L., McDonough, W. F. & Chappell, B. W. (1993). Carbonatite metasomatism in the northern Tanzanian mantle: petrographic and geochemical characteristics. *Earth and Planetary Science Letters* **114**, 463–475.

Scheelke, I. (1974). Models for the resistivity distribution from magnetotelluric soundings. In: Illies, J. H. & Fuchs, K. (eds) *Approaches to Taphrogenesis*. Stuttgart: Schweizerbart, pp. 362–365.

Schleicher, H. & Keller, J. (1991). Isotopengeochemie der Alkalivulkanite und Karbonatite des Kaiserstuhls: Aussagen zur Magmengenese und zur isotopischen Zusammensetzung des Erdmantels. *Jahreshefte des Geologischen Landesamts Baden-Württemberg* **33**, 33–57.

Schleicher, H., Keller, J. & Kramm, U. (1990). Isotope studies on alkaline volcanics and carbonatites from the Kaiserstuhl, Federal Republic of Germany. *Lithos* **26**, 21–35.

Schleicher, H., Baumann, A. & Keller, J. (1991). Pb isotope systematics of alkaline volcanic rocks and carbonatites from the Kaiserstuhl, Upper Rhine rift valley, F.R.G. *Chemical Geology* **93**, 231–243.

Sigmund, J. (1996). Diatrembreccien, Mantelxenolithe und Karbonatite in der Kernbohrung KB2 im Kaiserstuhl. Ph.D. thesis, University of Freiburg, 154 pp.

Simakin, A. G., Zavel'sky, V. O., Behrens, H., Kucherinenko, J. & Salova, T. (2005). A thermodynamic model for polymerized sodium aluminosilicate melt. *European Journal of Mineralogy* **17**, 243–250.

Skinner, E. M. W. (1989). Contrasting group I and II kimberlite petrology: towards a genetic model for kimberlites. In: Ross, J., Jaques, A. L., Ferguson, J., Green, D. H., O'Reilly, S. Y., Danchin, R. V. & Janse, A. J. (eds) *Proceedings of the Fourth International Kimberlite Conference, Volume 1.* Victoria, Australia: Blackwell Scientific, pp. 528–544.

Sobolev, N. V. (1977). *Deep-seated Inclusions in Kimberlites and the Problem of the Composition of the Upper Mantle*. Washington, DC: American Geophysical Union, 279 pp.

Späth, A., Le Roex, A. P. & Opiyo-Akech, N. (2001). Plume–lithosphere interaction and the origin of continental rift-related alkaline volcanism—the Chyulu Hills Volcanic field, Southern Kenya. *Journal of Petrology* **42**, 765–787.

Sun, S. S. & McDonough, W. F. (1989). Chemical and isotopic systematics of oceanic basalts: implications for mantle composition and processes. In: Saunders, A. D. & Norry, M. J. (eds) *Magmatism in the Ocean Basins. Geological Society, London, Special Publications* **42**, 313–345.

Ulmer, P. & Sweeney, R. J. (2002). Generation and differentiation of group II kimberlites: constraints from a high-pressure experimental study to 10 GPa. *Geochimica et Cosmochimica Acta* **66**, 2139–2153.

von Dietrich, Ph. Fr. (1783). Description d'un volcan, découvert en 1774, près le vieux Brisach. *Journal de Physique* **13**, 616 *et seq.*

Wallace, M. E. & Green, D. H. (1988). An experimental determination of primary carbonatite magma composition. *Nature* **335**, 343–346.

Wass, S. Y. & Rogers, N. W. (1980). Mantle metasomatism—precursor to continental alkaline volcanism. *Geochimica et Cosmochimica Acta* **44**, 1811–1823.

Watkinson, D. H. & Wyllie, P. J. (1971). Experimental study of the join $NaAlSiO_4$–$CaCO_3$–H_2O and the genesis of alkalic rock–carbonatite complexes. *Journal of Petrology* **12**, 357–378.

Watson, E. B., Brennan, J. M. & Baker, D. R. (1990). Distribution of fluids in the continental mantle. In: Menzies, M. A. (ed.) *Continental Lithosphere*. Oxford: Clarendon Press, pp. 111–125.

Wedepohl, K. H., Gohn, E. & Hartmann, G. (1994). Cenozoic alkali basaltic magmas of western Germany and their products of differentiation. *Contributions to Mineralogy and Petrology* **115**, 253–278.

White, B. S. & Wyllie, P. J. (1992). Solidus reactions in synthetic lherzolite–H_2O–CO_2 from 20–30 kbar, with applications to melting and metasomatism. *Journal of Volcanology and Geothermal Research* **50**, 117–130.

Wiechert, U., Ionov, D. A. & Wedepohl, K. H. (1997). Spinel peridotite xenoliths from the Atsagin-Dush volcano, Dariganga lava plateau, Mongolia: a record of partial melting and cryptic metasomatism in the upper mantle. *Contributions to Mineralogy and Petrology* **126**, 345–364.

Wilson, M. & Downes, H. (1992). Mafic alkaline magmatism associated with the European Cenozoic rift system. *Tectonophysics* **208**, 173–182.

Wimmenauer, W. (1957). Beiträge zur Petrographie des Kaiserstuhls. Einführung und Teil I: Die Ergubgesteine und Tuffe. *Neues Jahrbuch der Mineralogie, Abhandlungen* **91**, 131–150.

Wimmenauer, W. (1959). Beiträge zur Petrographie des Kaiserstuhls. Schlub von Teil I: Die Ergubgesteine und Tuffe. Teil II: Die essexitisch–theralitischen subvolcanischen Intrusivgesteine. Teil III. Die Ganggesteine der essexitischen Familie. *Neues Jahrbuch der Mineralogie, Abhandlungen* **93**, 133–173.

Wimmenauer, W. (1962). Beiträge zur Petrographie des Kaiserstuhls. Teil IV: Die Gesteine der phonolitischen Familie. Teil V: Die subvulkanischen Breccien. *Neues Jahrbuch der Mineralogie, Abhandlungen* **98**, 367–415.

Wimmenauer, W. (1963). Beiträge zur Petrographie des Kaiserstuhls. Teil VI: Die Karbonatite. Teil VII: Zur Petrogenese des Kaiserstuhls. *Neues Jahrbuch der Mineralogie, Abhandlungen* **99**, 231–276.

Winter, R. (1974). A model for the resistivity distribution from geomagnetic depth soundings. In: Illies, J. H. & Fuchs, K. (eds) *Approaches to Taphrogenesis*. Stuttgart: Schweizerbart, pp. 369–375.

Woermann, E. & Rosenhauer, M. (1985). Fluid phases and the redox state of the Earth's mantle. *Fortschritte der Mineralogie* **63**, 263–349.

Woolley, A. R. & Kempe, D. R. C. (1989). Carbonatites: nomenclature, average chemical composition, and element distributions. In: Bell, K. (ed.) *Carbonatites: Genesis and Evolution*. London: Unwin Hyman, pp. 1–14.

Wyllie, P. J. & Huang, W. L. (1976). Carbonation and melting reactions in the system CaO–MgO–SiO_2–CO_2 at mantle pressures with geophysical and petrographical applications. *Contributions to Mineralogy and Petrology* **54**, 79–107.

Yaxley, G. M. & Green, D. H. (1998). Experimental reconstruction of sodic dolomitic carbonatite melts from metasomatized lithosphere. *Contributions to Mineralogy and Petrology* **124**, 359–369.

Yaxley, G. M., Crawford, A. J. & Green, D. H. (1991). Evidence for carbonatite metasomatism in spinel peridotite xenoliths from western Victoria, Australia. *Earth and Planetary Science Letters* **107**, 305–317.

Yaxley, G. M., Green, D. H. & Kamenetsky, V. (1998). Carbonatite metasomatism in the southeastern Australian lithosphere. *Journal of Petrology* **39**, 1917–1930.